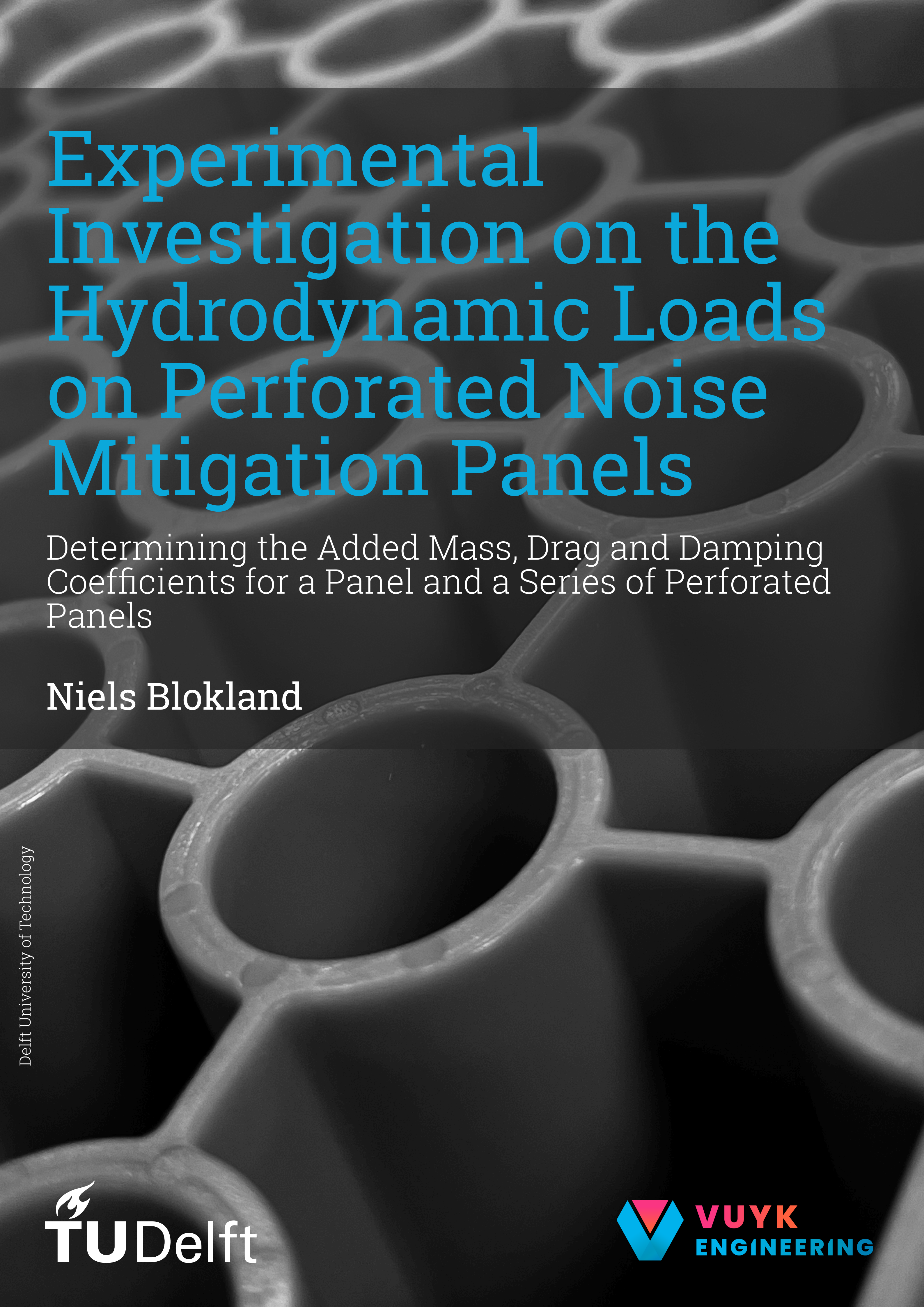

Experimental Investigation on the Hydrodynamic Loads on Perforated Noise Mitigation Panels

Determining the Added Mass, Drag and Damping Coefficients for a Panel and a Series of Perforated Panels

Niels Blokland

Delft University of Technology

Thesis for the degree of MSc in Marine Technology in the specialisation of Ship Hydromechanics

Experimental Investigation on the Hydrodynamic Loads on Perforated Noise Mitigation Panels

Determining the Added Mass, Drag and Damping Coefficients for a Panel and a Series of Perforated Panels

By

Niels Blokland

Performed at

Vuyk Engineering Rotterdam B.V.

This thesis MT.25/26.006.M is classified as confidential in accordance with the general conditions for projects performed by the TUDelft.

October 16, 2025

Thesis Exam Committee
Chair: Dr.-Ing. S. Schreier
Staff Member: Dr. ir. H.J. de Koning Gans
Staff Member: Dr. D. Fiscaletti
Company Member: Ir. B.J. van der Kleij

Author Details
Name: Niels Blokland
Student Number: 4964179

Preface

This thesis is written to complete my Master's degree in Marine Technology, with a specialisation in Ship Hydromechanics. The project was conducted at Vuyk Engineering Rotterdam B.V., and experimental tests were performed in the Ship Hydromechanics Lab at Delft University of Technology. Over the past months, I have had the opportunity to deepen my interest and expand my knowledge in hydrodynamics, both theoretically and experimentally. There are a few people I would like to thank for their assistance during the project.

Firstly, I would express my gratitude to Dr.-Ing. Sebastian Schreier and dr. ir. Henk de Koning Gans for their guidance, valuable feedback, and for sharing their expertise, which offered me helpful insights during the project. Next, I want to thank my supervisor from Vuyk Engineering, ir. Ben van der Kleij. Our weekly meetings provided me meaningful perspectives through your knowledge and experience in the field of hydrodynamics. Furthermore, I want to thank my colleagues at Vuyk Engineering for sharing their interest and the enjoyable time I had during the past months. In addition, I would like to thank Dr. Mark Wochner, inventor of the AdBm Noise Mitigation System, for his interest and contribution to this study. I also want to thank the staff of the Ship Hydromechanics Lab, especially Peter Poot, for his assistance with the experimental setup and execution. Finally, I want to thank my family, friends, and my girlfriend for their continuous support during this project.

Niels Blokland
Delft, October 2025

Summary

There is a lack of knowledge on the hydrodynamic behaviour of an AdBm Noise Mitigation System (NMS) designed to reduce sound during monopile piling, which is relevant for improving design and safety. The NMS contains panels designed to mitigate underwater noise. Model tests were performed on both an actual AdBm panel and geometry-based perforated panels, and hydrodynamic coefficients in the form of added mass (C_a), drag (C_d), and linear damping (C_b) were determined for the heave and surge directions, improving the understanding of hydrodynamic loads on the NMS.

Experiments were conducted in the Towing Tank No. 2 at TU Delft, where both forced oscillation and wave tests were performed with test conditions based on regular environmental waves. The hydrodynamic coefficients in heave and surge have been determined and show that the nondimensional Keulegan-Carpenter number (KC) is the most dominant parameter, which leads to the coefficients being expressed as functions of KC. Tests were performed with a single panel and three panels in series to study interaction effects. The main findings showed a significant decrease in C_d and C_b up to 70% within the tested KC range using panels in series, resulting in lower hydrodynamic loads compared to using a single panel. Furthermore, the results of the forced oscillation and wave tests were compared. The hydrodynamic coefficients were found to be similar for low KC values, but the forced oscillation results increasingly overestimated the hydrodynamic coefficient values as KC increased. However, the range of comparison was constrained due to limitations in the wave maker capabilities. The findings contribute to a better understanding of the hydrodynamic loads on the perforated models that reduce the knowledge gap of the hydrodynamic behaviour of the NMS, providing a basis for improving the design parameters for the deployment system.

Contents

List of Figures

List of Tables

Nomenclature

Abbreviations

Abbreviation	Definition
CFD	Computational Fluid Dynamics
DFT	Discrete Fourier Transform
DNV	Det Norske Veritas
ITTC	International Towing Tank Conference
NMS	Noise Mitigation System
NRMSE	Normalised Root Mean Square Error
OLS	Ordinary Least Squares
PMMA	Polymethyl methacrylate
RMSE	Root Mean Square Error

Symbols

Symbol	Definition	Unit
a	Fitted parameter added mass	-
A	Amplitude	m
A_d	Dimensional added mass	kg
b	Fitted parameter linear damping	-
B_d	Dimensional damping	kg/s
c	Wave velocity	m/s
c_g	Wave group velocity	m/s
C_a	Added mass coefficient	-
C_b	Linear damping coefficient	-
C_d	Drag coefficient	-
d	Fitted parameter quadratic drag	-
D	Characteristic structure length	m
D_h	Hole diameter	mm
f	Frequency	Hz
f_s	Sample rate	Hz
F	Force	N
g	Gravitational constant	m/s^2
h	Water depth	m
H	Height	m
H_s	Significant wave height	m
k_{air}	Air spring stiffness	N/m
k	Wave number	1/m
KC	Keulegan-Carpenter number	-
L	Length	m
M	Mass	kg
n	Polytropic index	-
n_h	Number of holes	-
p	Pressure	N/m^2
p_a	Atmospheric pressure	N/m^2
r	Radius	m

Symbol	Definition	Unit
R^2	Coefficient of determination	-
Re	Reynolds number	-
S	Surface area	m^2
t	Time	s
t_p	Panel thickness	mm
T	Period	s
τ	Perforation ratio	-
u	Fluid velocity	m/s
$\dot{u}$	Fluid acceleration	m/s^2
u_m	Maximum fluid velocity	m/s
U	Relative velocity	m/s
$\dot{U}$	Relative acceleration	m/s^2
V	Volume	m^3
V_r	Reference volume	m^3
W	Width	m
z	Depth	m
$\dot{x}$	Structure velocity	m/s
$\ddot{x}$	Structure acceleration	m/s^2
α	Scaling factor	-
α_c	Correction factor	-
λ	Wavelength	m
μ	Discharge coefficient	-
ν	Kinematic viscosity	m^2/s
ρ	Density	kg/m^3
ω	Frequency	rad/s
ω_n	Eigenfrequency	rad/s
ζ_a	Wave amplitude	m

1

Introduction

1.1. Background

The demand for wind energy has significantly increased in recent decades as a direct result of climate goals aimed at reducing emissions [1] [2]. However, the growth in the number of onshore wind farms is limited due to the expensive land near large population areas, limited space, and, from a social point of view, noise and visual pollution caused by wind turbines [3] [4]. Moreover, higher electricity production is generated in offshore areas compared to onshore due to higher wind velocities in the offshore region [3]. Consequently, there has been a significant shift towards the use of offshore wind resources, leading to the development of an emerging market for offshore wind power [5]. With the goal of the European Union to be climate neutral in 2050, the number of offshore wind farms will grow because it is expected that the offshore wind energy will account for at least 50% of the total energy production [6]. However, the installation of wind farms can significantly impact marine sea life [7]. Dahl said that loud and impulsive underwater sounds can have direct physical effects on fish and marine mammals, including physical injuries such as hearing damage [8]. Moreover, the intense sound pulses can disturb the behaviour of marine mammals at long distances, possibly leading to travel deviations. Furthermore, at longer distances, noise can affect animal communication and navigation. The hydroacoustic noise from pile driving is gaining attention because most foundations are installed using hydraulic hammers. Higher sound levels are expected in the future due to the installation of larger piles in offshore wind projects [9] [10]. This leads to regulations that limit noise levels in several countries [11]. For example, the German Federal Maritime and Hydrographic Agency (BSH) requires offshore pile driving to comply with a standard sound exposure level of 160 dB (SEL) and a peak sound pressure level of 190 dB (SPL) measured at a distance of 750 metres [10]. SPL is a measure of the sound pressure over a period of time, while SEL is the total sound energy, independent of duration. Similar noise limits are applied in the Netherlands, while in the United Kingdom the environmental impact is assessed for each project and a maximum noise level is established, which cannot be exceeded [4][12]. Consequently, underwater noise mitigation systems are often required to comply with the regulatory standards for offshore pile driving operations [13].

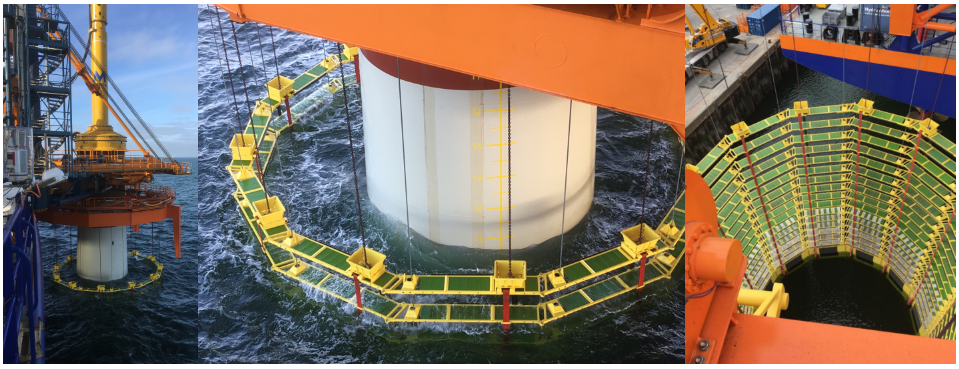

Figure 1.1: AdBm Noise Mitigation System [14]

A system that is able to reduce noise during pile driving is designed by AdBm Technologies. The company designed and developed a noise mitigation system, hereafter referred to as NMS, to reduce the noise levels during the installation of monopiles. Figure 1.1 illustrates the deployed and undeployed NMS. The NMS looks like a slat curtain that contains large arrays of panels, which are tuned to reduce the noise from hammer activities [15]. The short sides of the panels are connected to a frame and arranged side by side to form a slat, and multiple slats are connected to create a circular curtain around the monopile, which is lowered toward the seabed with distances of 1.0 metres between each layer (Figure 1.2). The panels consist of round air-filled cups whose geometry is designed to absorb the sound during pile driving. When a sound wave enters the open side of the cup, the air in the cup will oscillate and lead to a resonance at a specific frequency. This frequency leads to destructive interference with the sound wave, causing the sound to be absorbed. The open sides of the cups are placed down in the water to keep the air in the cups. There are three different types of panels, which are illustrated in Figure 1.3. The green panels are used in the first 10 metres from the water surface, the white panels in the following 10 metres, and the yellow panels for a depth between 20 and 40 metres, in which the latter dimension is approximately the depth of the seabed. As can be observed in the figure, the size of the round cups increases for panels positioned at higher depths. The hydrostatic pressure increases with increasing depth, compressing the air more strongly. The larger size of the air-filled cylinders compensates for the reduction in effective air volume, ensuring that the panels remain effective at the design frequency. There are open area holes between the round air-filled cups to reduce the vertical lift force during system recovery.

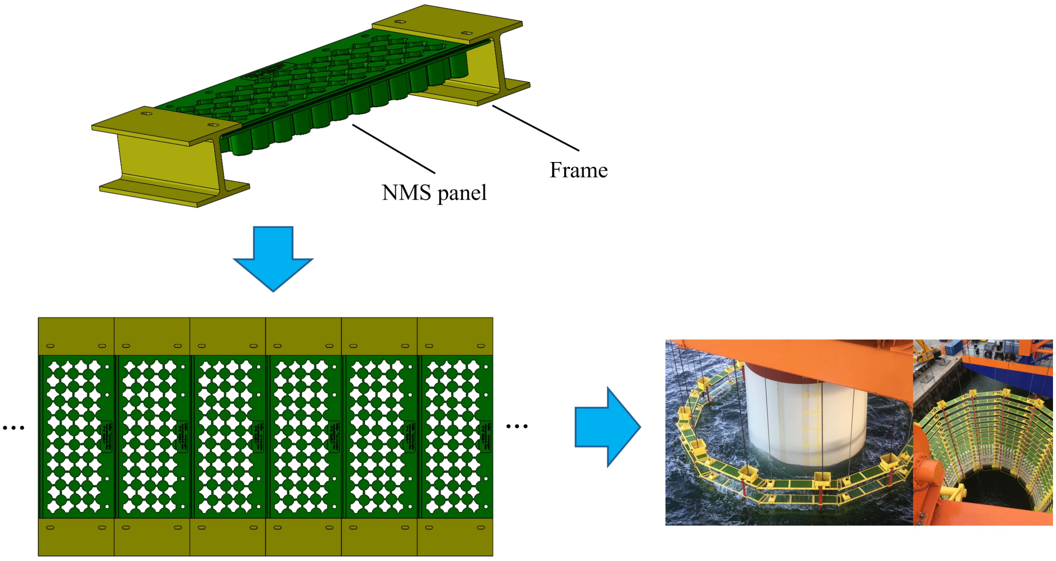

Figure 1.2: Drawing of a panel in the upper left corner, piece of a slat below the panel and a picture of the whole system in the bottom right [14].

1.2. Problem statement

It has been studied that the system works when considering only noise reduction [13][16]. However, no studies have yet been done on the hydrodynamic behaviour and interaction between the water and the NMS, nor on the hydrodynamic interaction among the slats themselves. Additionally, understanding how the system behaves during launch and recovery under environmental conditions is essential to setting design parameters for the deployment system. Although the behaviour of the system depends on the actual design of the system, there are aspects worth highlighting. Typically, the NMS is attached to a gripper, which also experiences loads due to the wave forces on the NMS and subsequent motions of the NMS. It is essential to maintain workability and operability as high as possible during installation. Since the largest projected area is orthogonal to the vertical direction, the forces are expected to be the highest in the vertical direction, resulting in the gripper experiencing the highest loads in this direction. Here, the vertical direction is defined as perpendicular to the sea surface and the horizontal direction parallel to the water level. Moreover, the NMS can collide with the monopile due to horizontal loads from environmental wave conditions, which can cause damage to both the monopile and the NMS. This is not only a technical disadvantage but also an economic one. Damages cost money and conflicts can arise with the monopile supplier due to damage to the pile. Consequently, performing a hydrodynamic analysis enables the establishment of design parameters and safety analysis, which are essential for contractors [17].

Figure 1.3: Three different types of panels used in the AdBm NMS [15].

1.3. Vuyk Engineering Rotterdam B.V.

Vuyk Engineering Rotterdam B.V. is a maritime design house that is continuously investing in the development of new technologies, innovations, and new solutions. Their goal is to develop design solutions that meet the requirements of clients, in which the NMS described above is an example. Vuyk is interested in the hydrodynamic loads on the complex-shaped NMS panels, which results can be used in software and further analysis to set up design conditions on the whole system and prevent over- or under-design, which is helpful for clients.

1.4. Scope and simplifications

The hydrodynamic loads on the NMS due to the waves are complex to calculate for a number of reasons. The complexity is related to both the environment and the system itself. The presence of the monopile, vessel motions, and potential irregular wave conditions have, in terms of the environment, effects on the hydrodynamic behaviour. In the system itself, the complex geometry of the panels, the presence of air in the cups, and the interaction between the vertical panel layers make the analysis challenging. Calculating the hydrodynamic behaviour of the entire system appears to be computationally and mathematically intensive. For this reason, simplifications are necessary but should be limited to include the most important forces and effects.

It is essential to account for the most dominant forces acting on the system to achieve a reliable design. These loads originate from waves. The highest loads are expected from the fluid flows normal to the projected area of the object. Due to the circular structure of the system, the direction of the undisturbed incoming wave will almost always be normal to the vertical area of the frame, with the result that loads in this horizontal direction are essential to investigate. The highest loads are expected in the vertical direction, as the largest area is orthogonal to the vertical direction. Therefore, this study focuses on horizontal and vertical hydrodynamic loads. However, the interaction effects between the vertically arranged panels should be investigated, as there is a chance that a panel is in the disturbed flow of objects above and below. Figure 1.4 shows a schematic illustration of three vertically arranged panels, including an undisturbed flow at the top. This figure is used to indicate what interaction effects in the vertical direction mean. Due to the openings in the panels, the incoming flow is disturbed and creates complex velocity fields that may also affect the panels below or above. It is unknown what the magnitude of these effects is on the hydrodynamic loads.

In the literature, it appears that hydrodynamic coefficients are essential input parameters for hydrodynamic analysis that can be used in numerical simulation to set design parameters, in which the latter is important for cost and safety analysis [18]. Knowing the geometry of the system, flow conditions, and hydrodynamic coefficients, the hydrodynamic forces can be estimated. Det Norske Veritas (DNV) provides the values of the hydrodynamic coefficients for simple geometries that can be used for marine operations [19]. However, these values are unknown for complex geometries such as the perforated panels described above. Moreover, DNV notes that conducting model tests is the most accurate method to determine hydrodynamic coefficient values, rather than analytical and numerical methods, particularly for perforated objects [20]. A commonly used method for complex geometric structures is to divide components of regular shape and sum up the loads of the individual parts by using hydrodynamic coefficients [17]. However, the interaction effects between the components themselves have to be taken into account because they overestimate or underestimate coefficient values if these effects are neglected [19][21].

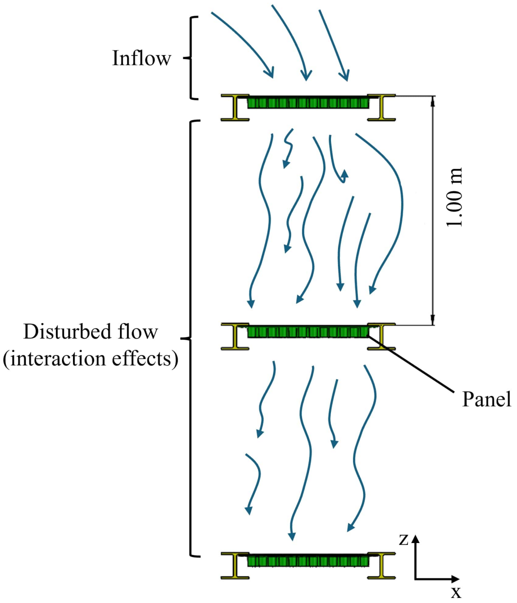

Figure 1.4: Schematic sketch of the possible interaction effects between the panel layers in the vertical direction.

The panels are identical and are distributed regularly for each circular layer. The symmetrical and regular structure of the ring provides opportunities to divide the system, where the forces on the individual objects can be considered representative of the whole. Using hydrodynamic coefficients of identical parts, which are lacking in the literature, enables hydrodynamic force calculations. It has been mentioned that this study focuses on the normal horizontal and vertical force on the NMS, which makes it possible to investigate the loads on a single panel, including the outer frame. However, possible vertical interaction effects must be taken into account. In addition, there are an extensive amount of studies on hydrodynamic analysis in perforated or ventilated structures, while there is a lack of research on noise mitigation curtains. This provides opportunities to utilise studies of the available literature on perforated structures to develop a method for determining hydrodynamic coefficients on perforated panels of the NMS, thereby extrapolating the results and considering a possible correction factor on the hydrodynamic coefficients due to interaction effects.

1.5. AdBm noise mitigation panels

Figure 1.5 shows schematic sketches of the AdBm panel without the outer frame, and relevant properties are given in Table 1.1. The panels are designed to reduce the noise from the hammer sounds during monopile installation. The presence of air in the round-shaped cups dampens the sound. This figure is meant to provide an idea of the physical geometry of the panels. Moreover, the properties can be used to identify similarities with previous studies, thereby enabling the selection of an appropriate hydrodynamic loading method or equation.

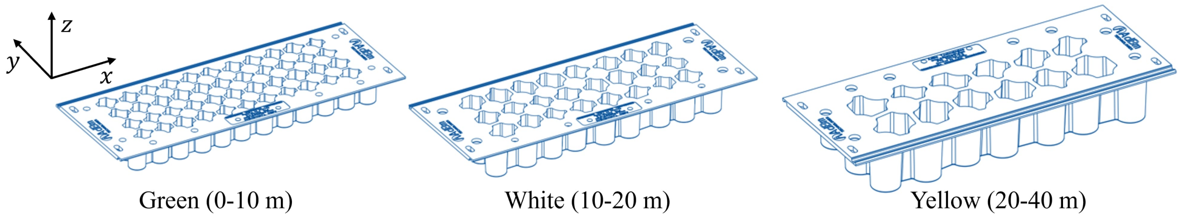

Figure 1.5: Schematic sketches of the three AdBm noise mitigation system panels: the green panel on the left, the white panel in the middle, and the yellow panel on the right.

Table 1.1: Structure properties of the green, white and yellow panels.

Variable	Green panel	White panel	Yellow panel
Length [m]	0.61	0.61	0.61
Width [m]	0.24	0.24	0.24
Height [m]	0.052	0.065	0.084
Amount of holes	44	24	12
Perforation ratio	0.28	0.28	0.28
Frame type	H - frame	H - frame	H - frame
Characteristic structure length (inclusive frame) [m]	0.76	0.76	0.76

1.6. Relevant studies on (perforated) structures in oscillatory flow

In the past, a significant amount of research has been done on the hydrodynamic characteristics of solid and perforated plates, which show similarities with the perforated panels in this study. Examples include the study of heave plates, which provide extra added mass and damping to improve the heaving motion of offshore structures [22]. Other examples include protection covers, mudmats, and simplified subsea modules. Table E.1 lists several previous research studies on the determination of hydrodynamic loads for solid and perforated plate-shaped structures. A common term is the perforation ratio, which is

$$\tau = \frac{\text{open area}}{\text{total area including open area}}. \tag{1.1}$$

Figure 1.6 is used to provide clarity on the definition of the perforation ratio, where the perforation ratio is equal to the area of the open holes divided by $L \times W$.

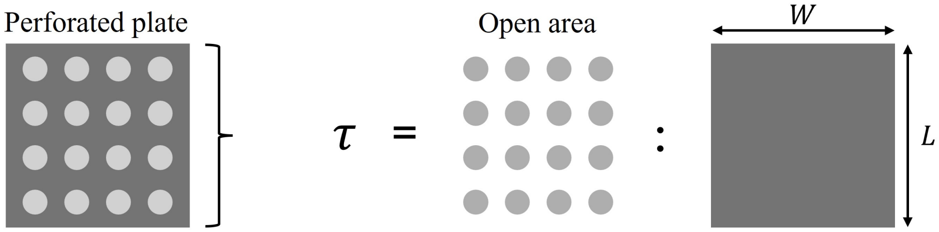

Figure 1.6: Clarification of the perforation ratio for perforated plates.

Each study examines the value of the hydrodynamic coefficients, which are used to estimate hydrodynamic loads. It appears that, in addition to the geometry, two nondimensional numbers in fluid mechanics are essential parameters in the value of the hydrodynamic coefficients: the Reynolds number and the Keulegan-Carpenter number. The origin and physical interpretation of both numbers are described in the following.

1.6.1. Reynolds number

The Reynolds number was introduced in 1883 by O. Reynolds, who demonstrated the transitions of laminar and turbulent flows by experiments and expressed the Reynolds number as

$$Re = \frac{uD}{\nu}, \tag{1.2}$$

where u is the velocity of the fluid, D the representative length, and ν the kinematic viscosity. This nondimensional number is a ratio between inertial and viscous forces and affects the values of the inertia and drag coefficients. The Reynolds number characterises the flow regime and boundary layers, which are important for hydrodynamic analysis.

1.6.2. Keulegan-Carpenter number

In 1958, G.H. Keulegan and L.H. Carpenter investigated the inertia and drag coefficients on a cylinder and a vertical plate in sinusoidal currents [23]. They found dependencies in the coefficients when they are related to the period parameter. They introduced the nondimensional number as

$$KC = \frac{u_m T}{D}. \tag{1.3}$$

u_m is the maximum velocity of the fluid, T the period, and D the characteristic length. Additionally, the authors found that the KC number influences the flow patterns around a structure and that flow behaviour has a significant influence on the variations of the inertia and drag coefficient. For sinusoidal flow with amplitude A, the Keulegan-Carpenter number can be expressed as

$$KC = \frac{2\pi A}{D}. \tag{1.4}$$

1.6.3. Hydrodynamic load equations and coefficients

The studies mentioned above use different equations to estimate the loads on the structures under oscillatory flow conditions. Some studies estimate the loads using the semi-empirical Morison equation, which assumes that the total force has two contributors: an inertia force and a drag force. The Morison equation is given as

$$F(t) = \underbrace{\rho V \dot{u}(t)}_{\text{FK}} + \underbrace{\rho V C_a \dot{U}(t)}_{\text{Added mass}} + \underbrace{\frac{1}{2}\rho S C_d U(t)\left|U(t)\right|}_{\text{Drag force}}. \tag{1.5}$$

ρ is the density of the fluid, V is the volume of the structure, $\dot{u}(t)$ is the acceleration of the fluid, $\dot{U}(t)$ is the relative acceleration between the fluid and the structure ($\dot{u}(t) - \ddot{x}(t)$), S is the surface area, $U(t)$ is the relative velocity between the fluid and the structure ($u(t) - \dot{x}(t)$), C_a is the added mass coefficient and C_d is the drag coefficient. The first term is the Froude-Krylov force (FK), which arises from the pressure acting on a body surface from an undisturbed wave. The added mass is a measure of the acceleration of the fluid due to the presence of the body. The added mass coefficient (C_a) and drag coefficient (C_d) can be determined using Equation 1.5, which is performed in [24], [25], [26], [27] and [28].

Other studies estimate the force by determining the values of the added mass and the linear damping terms given in Equation 1.6.

$$F(t) = \underbrace{\rho V \dot{u}(t)}_{\text{FK}} + \underbrace{A_d \dot{U}(t)}_{\text{Added mass}} + \underbrace{B_d U(t)}_{\text{Linear damping}} \tag{1.6}$$

A_d is the dimensional added mass coefficient and B_d is the dimensional coefficient. The added mass and damping are commonly made nondimensional by normalising them using a theoretical reference volume V_r, which value is based on a reference volume of a similar but simpler body shape. Using a reference volume simplifies the comparisons with other similar geometries and helps to compare the results with other studies. This reference volume is an estimate of the volume of fluid displaced when moving the body. The added mass and the linear damping coefficient are then found with equations 1.7 and 1.8, respectively.

$$C_a = \frac{A_d}{\rho V_r} \tag{1.7}$$

$$C_b = \frac{B_d}{\rho \omega V_r} \tag{1.8}$$

Figure 1.7 to get insight into the reference volumes used in the literature to nondimensionalise the added mass and linear damping. The black shapes are geometries that oscillate in a vertical direction. The light blue volumes are the reference volumes. The reference volume for an oscillating circular disc, which can be observed in the middle of Figure 1.7, is based on the theoretical added mass derived from potential flow theory [29].

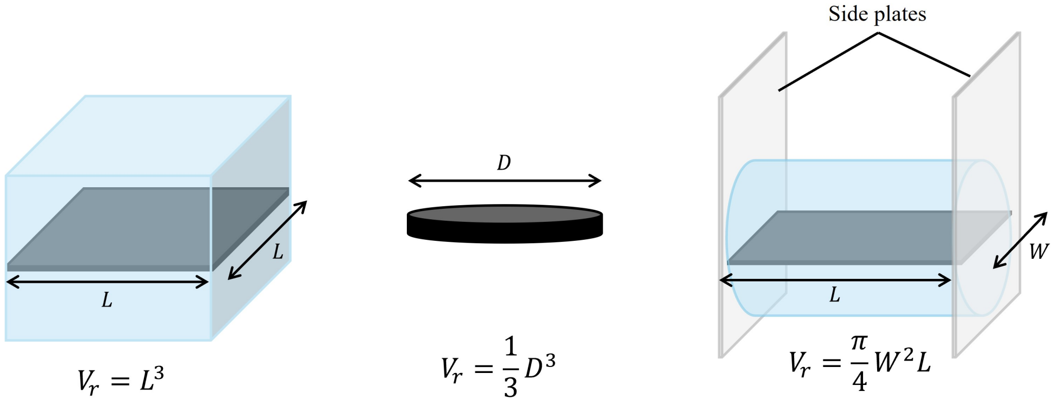

Figure 1.7: Reference volumes that are used in studies to nondimensionalise hydrodynamic added mass and linear damping coefficients. Left: square plate and V_r used in [24], [25], [26] and [27]. Middle: circular shape and V_r used in [28], [30] and [31]. Right: rectangular shape and V_r used in [21] and [32].

The method of estimating hydrodynamic loads by determining the values of the added mass and linear damping coefficients is carried out in the studies in [21], [22], [28], [30], [32] and [33]. The only difference between Equation 1.5 and Equation 1.6 is the drag force and the linear damping force; therefore, the physical difference will be discussed.

1.6.4. Physical difference between linear damping and drag force

Linear damping is proportional to velocity and is related to two sources. First, it is related to the energy dissipation caused by waves, which are generated by the movement of the object. Second, it is associated with skin friction, which is the viscous friction between the fluid and the object due to the boundary layers near the surface [34]. The drag force is proportional to the velocity multiplied by the absolute velocity. The drag force is also known as quadratic damping. This term is mainly caused by flow separations and vortex sheddings at the edges of the object and is commonly referred to as form drag [28][34]. Higher KC values are related to a higher ratio between fluid particle displacement and object size, causing more space and time for vortex sheddings to become larger and stronger [35].

The flow separations and vortex sheddings become more significant as the KC increases, leading to the quadratic drag becoming more dominant than the linear damping. Consequently, the behaviour of the fluid, both locally and globally, around the object is essential to assess the dominance of linear and quadratic damping. The nondimensional Re and KC numbers are relevant for describing the fluid behaviour and can be used to find the ratio between drag and linear damping forces in different Re and KC regimes.

1.6.5. Overview and relevant findings from previous studies

Table 1.2 summarises Table E.1, where the most important studies are listed, including the geometry, perforation, experimental method, and KC conditions. A commonly used method to find coefficients is to conduct forced oscillation tests in still water because the kinematics is identical between an oscillating object in still water and an oscillating fluid passing a fixed object [36]. Moreover, Mentzoni pointed out that oscillations are useful to study hydrodynamic effects by varying parameters and that the resulting coefficients are used by project engineers for analysis and planning [21].

Table 1.2: Previous studies on (perforated) plates and their conditions.

Author(s)	Geometry	Holes	Method	KC
Z.H. Liang et al. [24]	Rectangular (0.4x0.4 m)	no	Heave forced oscillation	0.3-1.6
J. Li et al. [25]	Rectangular (0.4x0.4 m)	yes	Heave forced oscillation	0.2 - 1.2
K.H. Chua et al. [26]	Rectangular (0.4x0.4 m)	yes	Heave forced oscillation	0.2 - 1.3
K. Liu et al. [27]	Rectangular (0.85x0.85 m)	no	Heave forced oscillation	0.2 - 0.6
S. An and Odd M. Faltinsen [33]	Rectangular (0.52x0.37 m)	yes	Heave forced oscillation and numerically	0.2 - 1.7
L.F. Cong and B. Teng [22]	Rectangular	yes	Numerically	0.5 - 1.0
T. Kristensen et al. [32]	Simplified perforated models (L = 0.57 m)	yes	Heave forced oscillation	0.2 - 2.5
F. Mentzoni [21]	Simplified perforated models (L = 0.57 m)	yes	Heave forced oscillation, waves and numerically	0.2 - 2.0
X. Tian et al. [30]	Circular, hexagon, square, rectangle, triangle (D=0.2 m)	yes	Heave forced oscillation	0.2 - 3.2
X. Tian and X. Li [31]	Circular	no	Numerically	0.2 - 1.0
L. Tao and D. Dray [28]	Circular (D = 0.40 m)	yes	Heave forced oscillation	0.2 - 1.2

Tian et al. (2013) present a numerical investigation of the effects of the Reynolds number between $O(10^2)$ and $O(10^7)$ on the added mass and linear damping coefficients on an oscillating circular disc and conclude that the effect of the Reynolds number is not significant [31]. On the other hand, Tao and Dray conducted heave oscillation tests on circular discs with frequencies between 0.1 and 1.0 Hz for perforation ratios between 0% and 20% and concluded that the added mass coefficients were approximately 45 $\%$ lower for the higher frequencies in the KC range between 0.2 and 1.2 with a 20$\%$ perforation ratio [28]. However, the damping coefficient was found to be insensitive to the oscillation frequency when the perforation ratio increased to 20%.

Li et al. (2013) investigated the value of the added mass and quadratic drag coefficients for rectangular plates with forced oscillations and studied, among others, the effects of the KC number, frequency, hole geometry, and multi-plates [25]. An important finding is that the KC number is the most dominant factor compared to the frequency in the value of the hydrodynamic coefficients. This finding has been confirmed by the studies of Ezoji et al. (2022) and Zhang et al. (2023), who investigated the influence of the KC number on the coefficient values using forced oscillations [37] [38]. Li investigated the values of the added mass and drag coefficients using multi-plates with a plate distance-length ratio between 0.5 and 1.5 and oscillation amplitude up to 76 mm using a solid plate and a 5$\%$ perforated plate. It was found that when multiple plates were placed closer to each other, the value of the hydrodynamic coefficients decreased compared to the sum of individual single-plate contributions. However, C_a and C_d are identical for $\frac{H}{L}$ $=$1.5 using a single plate and multi-plates. Furthermore, the differences in both coefficients using a single plate and multi-plates decrease with a higher perforated plate ratio. Particularly, the quadratic drag term was sensitive to interaction effects. Moreover, there appears to be little to no difference in the values of the hydrodynamic coefficients for plates with the same perforation ratio but different hole sizes [25]. This is in line with the results of Tian et al. (2017), where forced oscillations were performed on perforated circular discs with five different hole sizes with a diameter between 4 and 31.5 mm with the same perforation ratio [30]. On the other hand, Molin investigated added mass and damping coefficients for oscillating porous discs and states that the pressure difference through the holes is equal to $\Delta p = \frac{1}{2\mu}\rho U|U|$ [39]. Molin introduces the discharge coefficient μ, whose value depends on the Reynolds number and the shape of the openings. Consequently, the pressure difference through the holes depends on the geometry of the holes, leading to possible differences in drag and damping coefficients.

F. Mentzoni performed an extensive study on the hydrodynamic loads in plate-shaped perforated and ventilated structures, which are simplified models of subsea modules [21]. He investigated the value of the added mass and linear damping coefficients by conducting experiments and numerical simulations and studied the hydrodynamic loads in forced oscillation and incident wave tests. The results show that the hydrodynamic loads of the oscillation tests and incident wave tests are similar at low KC values (KC < 0.3). However, the difference increases with increasing KC values, with higher measured forces from oscillation tests [21]. Figure 1.8a shows the experimental results of the normalised force plotted with the related KC for forced oscillation tests and incident wave tests using a ventilated plate. The black markers represent the data for the oscillation tests, whereas the coloured triangular symbols correspond to the wave test. Downward-pointing triangles indicate higher-period waves, whereas leftward-pointing triangles correspond to lower-period waves. The colour of the triangles is related to the depth of submergence. The main finding from this figure is the difference in the measured forces between the forced oscillation tests and the incident wave tests. The author states that these differences can be attributed to the horizontal velocity component in the orbital fluid motion, which is not present in the oscillation test. Oscillating the model in still water will form symmetric vortices at the edges and in the holes, whereas in orbital wave fluid motion, this symmetry breaks, leading to variations in the hydrodynamic coefficients. This is illustrated in Figure 1.8b, where the asymmetric vortices under orbital flow conditions can be obtained in the upper figure and the symmetric vortices from the vertical oscillation can be obtained in the lower figure. Mentzoni concludes that the large vortex on the left side of the top figure results in a low pressure, which leads to lower measured forces in incident wave tests.

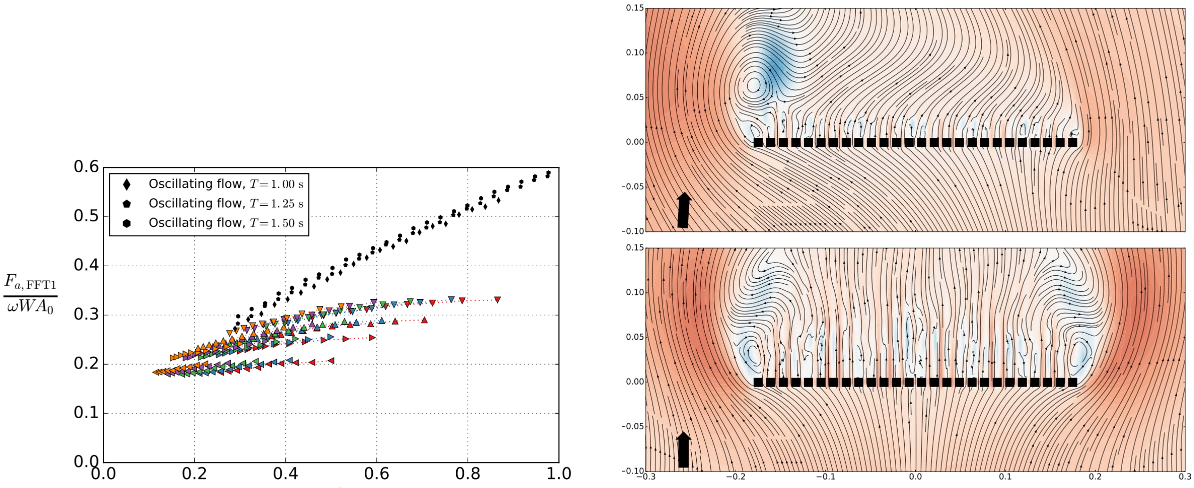

(a) Experimental normalised force for oscillation tests and incident wave tests.

(b) Numerical streamline plots of orbital flow conditions on the top and vertical oscillating flow conditions on the bottom around a ventilated structure.

Figure 1.8: Experimental results of forced oscillation tests and incident wave tests and numerical simulations on a ventilated structure performed by F. Mentzoni [21].

Similarly to the study by Li et al. (2013), Mentzoni shows that the added mass coefficients obtained from oscillating two parallel plates closely match the values predicted by superposing the results from a single plate. However, when the damping coefficients are superposed, the resulting damping is overestimated. Both studies refer to the work of Tao et al. (2007), who explain the lower damping coefficients by using two plates. The authors investigated the effect of KC and plate spacing on hydrodynamic characteristics using a finite difference method [40]. The most significant finding is that the vortex shedding interaction between the plates results in lower damping and that this interaction becomes stronger as KC increases.

As mentioned above, the KC value is the most dominant parameter in the value of the hydrodynamic coefficients. Therefore, a commonly used method is to plot the hydrodynamic added mass, quadratic drag, and linear damping coefficients as functions of KC. A general trend is that the added mass increases linearly or near-linearly with increasing KC number [25][27][28][33][38]. However, a trend observed in the study by Tian et al. (2017) is that the added mass coefficient tends to approach an asymptotic value at a certain KC value [30]. In the same way, the damping coefficient shows the same linear or near-linear trend as the added mass coefficient for increasing KC values [21][28][30][33]. Similarly to the added mass coefficient, the slope of the linear damping coefficient decreases after a specific KC value. This transition is more pronounced for the damping coefficient than for the added mass coefficient [37]. According to studies, the drag coefficient decreases non-linearly with increasing KC number [24][25][26][27][28]. This decrease is most significant for KC numbers below one. The drag coefficient is less sensitive to larger numbers of KC and tends to go to an asymptotic value.

J.M.R. Graham investigated the flow around sharply edged solid structures in oscillatory flow at low KC and provided that the drag coefficient curve varies as a function of KC in the form of $C_d \sim KC^{-\frac{1}{3}}$ for a flat plate [41]. The drag coefficient can then be estimated with equation 1.9. Graham's theoretical value for α is 11.8 for a flat plate. However, according to Mentzoni, this value is lower for perforated plates and depends on the geometry of the model [21]. Furthermore, Mentzoni linearised equation 1.9 to estimate the linear damping coefficient with equation 1.10 and concluded good agreement between his experimental and numerical results on solid and perforated plates and the study of Graham. Consequently, quadratic damping and linear damping coefficients can be estimated in the form of equations 1.9 and 1.10 as functions of KC.

$$C_d = \alpha \cdot KC^{-\frac{1}{3}} \tag{1.9}$$

$$C_b = \frac{b_1}{\pi^2} KC^{\frac{2}{3}} \tag{1.10}$$

The main findings of the literature and previous studies on (perforated) flat structures that are relevant in this study are summarised as follows:

- Investigating the value of hydrodynamic coefficients is an excellent method for estimating hydrodynamic loads on complex structures by conducting model tests.
- A commonly used method for complex geometric structures is to divide regular-shaped objects and sum up the hydrodynamic loads of the individual parts and take interaction effects into account. As a result, this study focuses on hydrodynamic loads of a single perforated NMS panel that includes the outer frame.
- Forced oscillation tests are an effective method for finding hydrodynamic coefficient values; however, differences have been observed in the hydrodynamic loads between forced oscillation tests and incident wave tests for the same KC values, in which the hydrodynamic coefficient values were higher in forced oscillation tests within the tested conditions.
- The most dominant parameter in the values of the coefficients is the nondimensional KC number, and the coefficient values are usually plotted as functions of the KC. Trends are observed where the added mass and linear damping coefficients increase and the drag coefficient decreases as functions of KC.
- There appears to be little to no difference in the hydrodynamic coefficients for oscillating plates with the same perforation ratio but different round hole sizes [25][30]. However, different hole geometries can influence the drag and damping coefficient values.
- Using multi-arranged plates will decrease the value of the hydrodynamic coefficients compared to the sum of individual single-plate contributions. Primarily, the quadratic drag and linear damping coefficient are sensitive to interaction effects.

1.7. Influence of the air on the hydrodynamic loads

For the NMS under investigation, the most important factor in reducing the sound is the presence of air in the round-shaped hollow cups. However, this air may influence the hydrodynamics of the panels. Therefore, it has to be investigated what the effect of air is on the hydrodynamic behaviour. Air-filled cups can be seen as a mass-spring system, where air behaves like a spring with stiffness k_{air}, and the mass is the mass of water. This is illustrated in Figure 1.9, which is a schematic sketch of a cup in the panel. The total water is the water inside the cup and an approximated added mass just outside the cup because this mass is expected to contribute to the mass-spring system. However, although this volume is unknown, it is approximated as half the volume of a sphere equal to $\frac{2}{3}\pi r^3$.

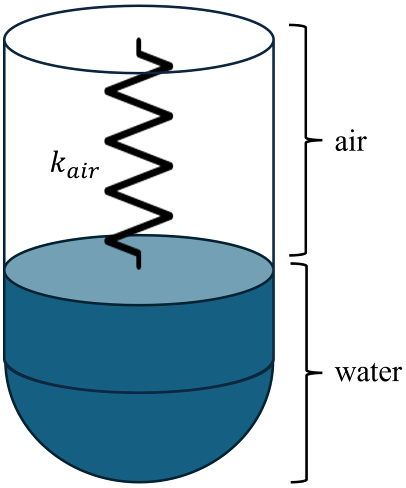

Figure 1.9: Sketch of a single cup where the system can be seen as a mass-spring system.

The pressure in the water increases with increasing water depth, resulting in the volume of air decreasing with depth. To calculate how much the volume of air decreases in depth, a combination of the polytropic equation and static pressure is used. The polytropic equation is given in Equation 1.11. The polytropic process describes the relation between pressure and volume for a thermodynamic process. The polytropic index n ranges from 1.0 to 1.4 for air [42]. This index is related to heat transfer between the air and the surroundings. When air is compressed, the molecules are pressed closer together, which increases the internal energy and consequently the temperature. The air temperature remains constant if the heat can be transferred to the surroundings. This is an isothermal process where n=1. On the other hand, the air temperature will increase if the heat is not transferred to the surroundings. This is an adiabatic process, for which n = 1.4. Since exact thermal conditions are unknown, a polytropic index range between 1.0 and 1.4 is used for further calculations.

$$pV^n = C \tag{1.11}$$

The static pressure in depth is equal to

$$p(z) = p_a - \rho g z, \tag{1.12}$$

where p_a is the atmospheric pressure, g is the gravity constant and z is the depth. The static force is the pressure multiplied by the area of the cup. It can be concluded that the pressure increases and the volume of air decreases as the depth increases.

Figure 1.10 contains the pressure force for different depths and the height of compressed air due to the increase in pressure with depth for n = 1. This figure is used to explain how the stiffness of the air is determined for different depths. The stiffnesses are determined by taking the slope at each point with the central difference method. For the first and last values, the forward and backward difference methods are applied, respectively. Knowing the stiffness and the amount of mass of water inside the cup, the eigenfrequencies can be determined with

$$\omega_n = \sqrt{\frac{k_{air}}{m_{water}}}. \tag{1.13}$$

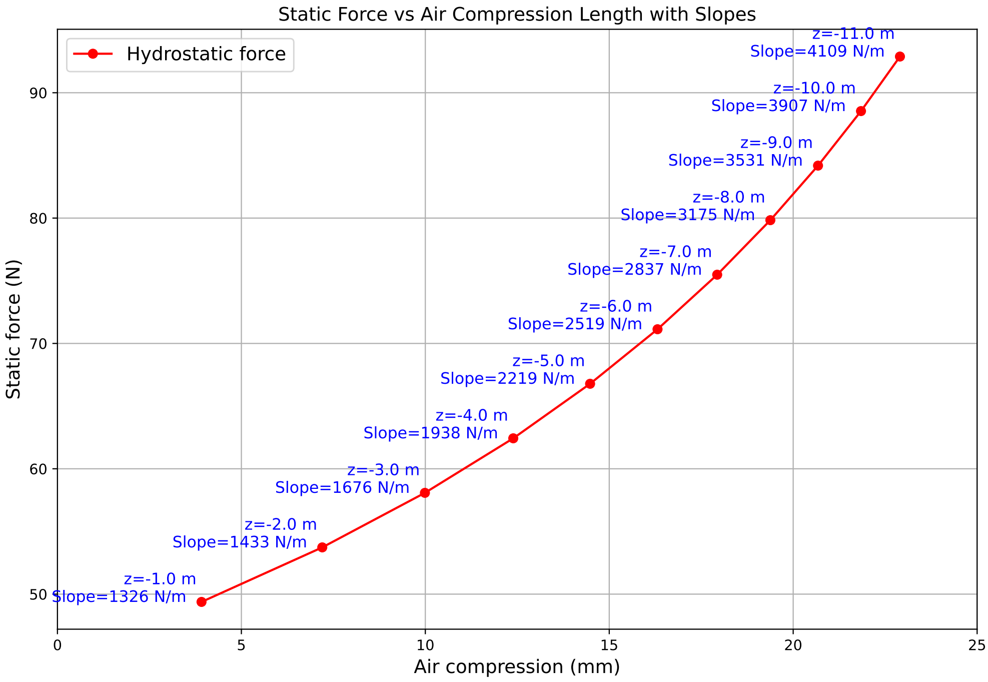

Figure 1.10: Force from hydrostatic pressure and the compression length of the air for the first 10 meters. The slope at each point is equal to the air spring stiffness k_{air}.

The same method is applied for the other polytropic indices, where the results can be obtained in Figure 1.11. The x-axis represents the length of air compression. It can be observed from the figure that the slope of the lines, and consequently the value of the air stiffness, is different for different polytropic index values. The lower the amount of heat that can be transferred to the surroundings, the higher the stiffness of the air.

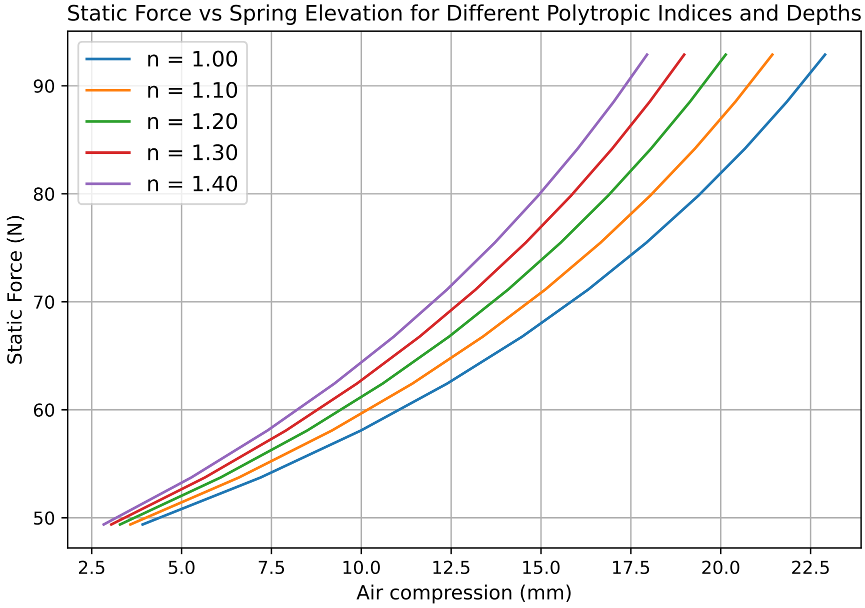

Figure 1.11: Force from hydrostatic pressure vs the air compression length in millimetres.

The eigenfrequencies of the mass-spring system for the cups in the green panel are provided in Figure 1.12 for different depths and different polytropic index values. This figure is used to compare the values of the eigenfrequencies with the frequencies of the environmental wave conditions.

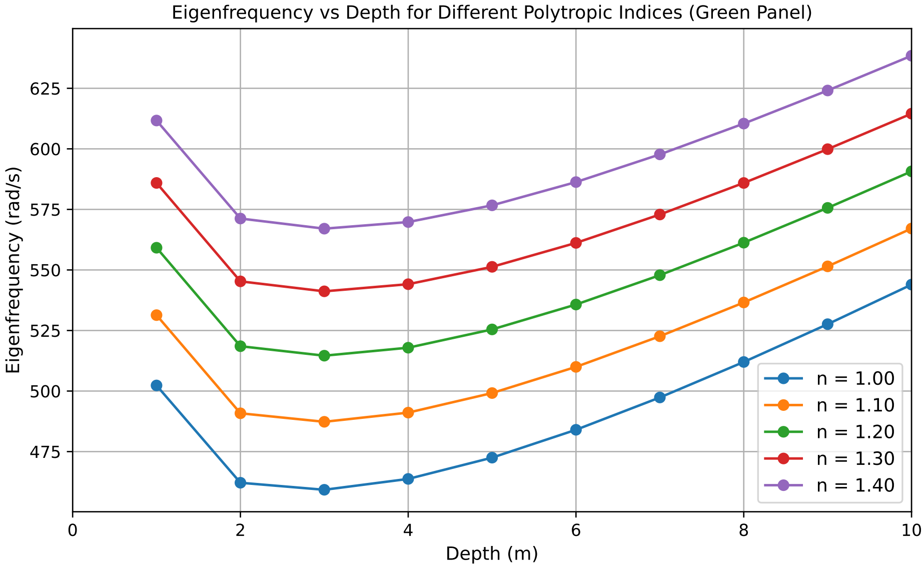

Figure 1.12: Eigenfrequencies of the mass-spring system for different depths.

The eigenfrequencies of the mass-spring system are higher than 450 rad/s, which is significantly higher than the frequencies of the waves that occur in practice. As a result, the air in the cups responds quasi-statically to the pressure variations induced by the waves. This means that there is no phase difference between the compression and expansion of the air and the incoming waves, with the result that dynamic air vibrations and inertia effects due to the mass of the water are negligible. Consequently, the force can be seen as a linear spring force, as in Equation 1.14, which does not contribute to the hydrodynamic load, since the latter arises from fluid motions.

$$F_{spring}(t) = -k_{air}\Delta z(t) \tag{1.14}$$

1.8. Literature gap analysis

The hydrodynamic behaviour of perforated structures and the effects of various parameters relevant to this study have been extensively studied. However, these studies focus on the forces in the heave direction and are limited to significantly lower KC values compared to those considered in the present work, thus revealing a gap in existing research. An overview of the KC values used in the studies compared to the KC values in this study is shown in Figure 1.13. The way in which the values in this study were derived will be discussed later. The difference is mainly because the geometry of the panels is much smaller than in previous studies.

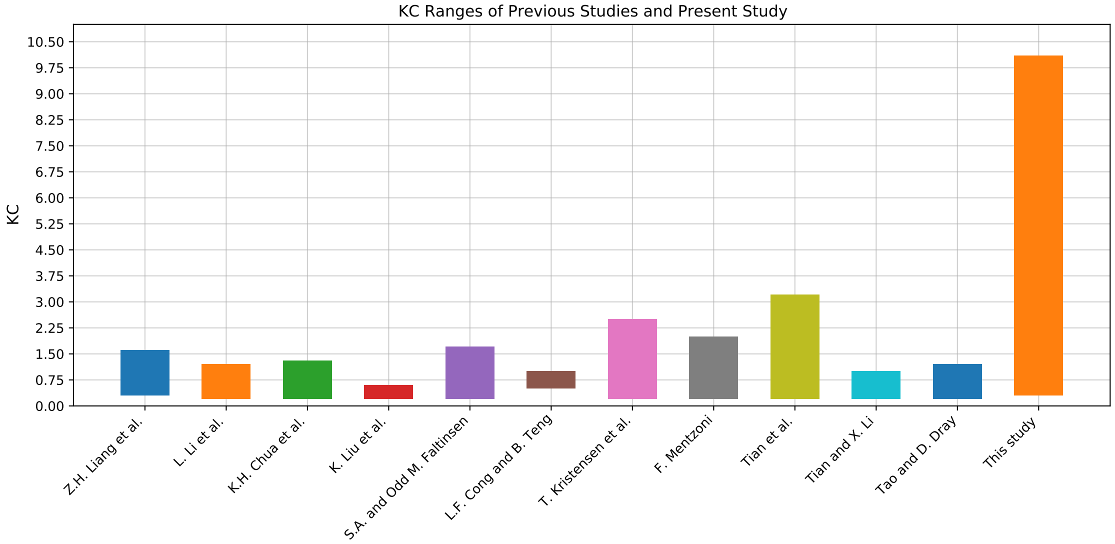

Figure 1.13: Overview of the KC range in previous studies on (perforated) flat structures compared to the present study.

Furthermore, the hydrodynamic behaviour with the specific perforated geometry shown in Figure 1.5 has not been previously investigated.

It appears that there is a physical difference in quadratic and linear damping in which the quadratic damping is related to form drag and the linear damping is related to wave energy dissipation and friction drag. Knowing the behaviour of the fluid near and around the structure is important to assess the dominance of friction and form drag. Due to the difference in structural geometry and the lack of knowledge of the fluid behaviour around the panels, it is unknown what the value and ratio of the linear and quadratic damping are in different Re and KC regimes.

Consequently, it can be learnt that the Keulegan-Carpenter number has the most significant influence on the hydrodynamic coefficients and what the trend is of the added mass, drag, and linear damping coefficients as a function of KC. Furthermore, studies show the significant effects of plates in series and the difference in forced oscillation and wave tests on the hydrodynamic coefficient values. However, these studies do not consider a structural geometry identical to that in the present study, and the range of KC values investigated is significantly lower.

1.9. Research objective

This research aims to determine the hydrodynamic coefficients in the form of added mass, drag, and linear damping of a perforated panel including a frame in the horizontal (surge) and vertical (heave) directions. However, possible interaction effects between the vertical panel layers must be taken into account. Both the drag force and the linear damping force are included in this study to ensure that damping effects are not neglected. This is achieved by finding a drag coefficient C_d related to the drag force and a linear damping coefficient C_b related to the linear damping. The results can be used in engineering software to estimate hydrodynamic loads on the system. This will provide more insight and expectations into the behaviour of the system, which can be helpful in setting design parameters and limits for the NMS deployment system. The total hydrodynamic load will be determined with Equation 1.15, which separates Froude-Krylov, added mass, drag, and linear damping forces.

$$F_{hyd}(t) = \underbrace{\rho V \dot{u}(t)}_{\text{FK}} + \underbrace{\rho V_r \mathbf{C_a} \dot{U}(t)}_{\text{Added mass}} + \underbrace{\frac{1}{2}\rho S \mathbf{C_d} U(t)\,|U(t)|}_{\text{Drag force}} + \underbrace{\rho V_r \omega \mathbf{C_b} U(t)}_{\text{Linear damping}} \tag{1.15}$$

1.10. Research question and research subquestions

In order to comply with the objective of the study, the main research question and sub-questions are formulated as follows:

Research question

- What are the values of the hydrodynamic coefficients in the heave and surge directions in the form of added mass, drag, and linear damping for the perforated panels in realistic wave conditions?

Research subquestions

- What are the values of the hydrodynamic coefficients in forced oscillation tests and fixed structure wave tests, and how can they be compared?
- What is the effect of multiple panels arranged in series on the hydrodynamic coefficients?

1.10.1. Research methodology

Model tests are conducted to achieve the research objective, which is the most accurate method for perforated objects according to DNV, rather than numerical simulations and analytical equations [20]. In addition, the correctness of the results from numerical simulations and analytical equations can be questioned, and the results need to be validated with experimental results. The model tests will be performed in the towing tank at Delft University of Technology. The aim is to perform experimental tests that are representative of the conditions and fluid kinematics to which the panels are exposed in the real world. It appears that the nondimensional KC and Re numbers influence the value of the hydrodynamic coefficients, whereby the KC number is the most dominant factor for the Re and KC combinations in this study. Therefore, test conditions must be based on these nondimensional numbers. Two types of model tests will be conducted: forced oscillation tests in still water and wave tests with a fixed structure. Forced oscillations are conducted for the following reasons:

- Forced oscillation tests using flat perforated objects have been an extensively used method in determining hydrodynamic coefficients in the past. It is useful to study effects by varying parameters such as KC, Re, perforation ratio, hole sizes, and multi-arranged objects. The results of the forced oscillation tests can be compared with the literature to observe similarities.
- According to Mentzoni, the coefficients are used by project engineers for analysis and planning [21].
- Forced oscillation tests are able to reach a higher value of KC compared to wave tests in model tests. As a result, the full range of KC numbers in this study can be tested with forced oscillations, while this is challenging for wave tests. This will be explained in more detail in the following chapter.

In addition, wave tests will be performed for two main reasons. First, the most dominant hydrodynamic loads on the panels originate from waves. Second, studies show discrepancies in the values of hydrodynamic coefficients between forced oscillation tests and wave tests while keeping the KC constant. Consequently, both forced oscillation and wave tests will be performed.

To find the value of the hydrodynamic coefficients from the model test, the Ordinary Least Squares (OLS) regression method is applied. This theory is described in Appendix B and is commonly used in the literature described above [25][26][34][38][43].

2

Translation to experiments

2.1. Regular wave theory

Figure 2.1 shows the wave profile of a regular wave in the space x direction on the left and, on the right, a regular wave as a function of time.

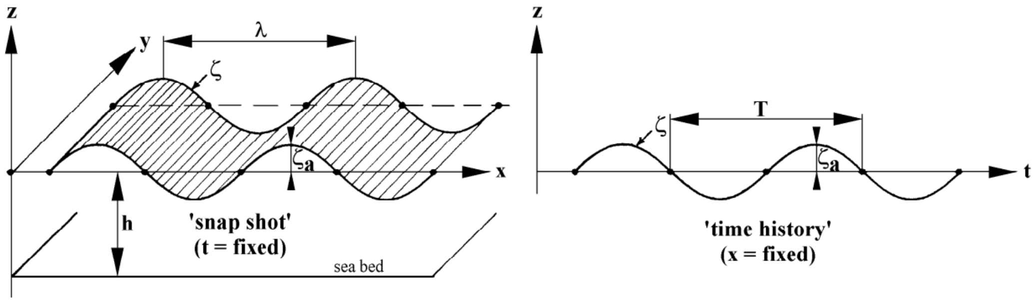

Figure 2.1: Wave profile of a regular wave in distance x and in time, respectively [44].

h is the water depth, ζ is the wave elevation, ζ_a is the wave amplitude, λ is the wavelength, and T is the wave period. The particle velocities in the x and z directions for regular waves can be determined with Equation 2.1 and Equation 2.2, respectively [44].

$$u = \zeta_a \cdot \omega \cdot \frac{\cosh k(h+z)}{\sinh kh} \cdot \cos(kx - \omega t) \tag{2.1}$$

$$w = \zeta_a \cdot \omega \cdot \frac{\sinh k(h+z)}{\sinh kh} \cdot \sin(kx - \omega t) \tag{2.2}$$

u is the horizontal velocity, w is the vertical velocity, ω is the wave frequency, z is the vertical distance or depth, x is the horizontal distance, t is the time and k is the wave number which can be found with the dispersion relationship given in Equation 2.3. The wave number is used to find the wavelength with Equation 2.4.

$$\omega^2 = kg \tanh(kh) \tag{2.3}$$

$$\lambda = \frac{2\pi}{k} \tag{2.4}$$

The wave particle trajectories can be found with Equation 2.5. x_1 and z_1 are the mean positions of the water particles. This equation provides insight into how the fluid particle moves around the panels for different depths, which is also important for investigating possible vertical interaction effects.

$$\frac{(x-x_1)^2}{\left(\frac{\zeta_a \cdot \cosh k(h+z_1)}{\sinh kh}\right)^2} + \frac{(z-z_1)^2}{\left(\frac{\zeta_a \cdot \sinh k(h+z_1)}{\sinh kh}\right)^2} = 1 \tag{2.5}$$

One can define three different types of waves: deep water waves, intermediate water waves, and shallow water waves. If $\frac{h}{\lambda} > 0.5$ the wave can be considered as a deep water wave and if $\frac{h}{\lambda} < 0.05$ there are shallow water waves. The wave is considered an intermediate water wave if the ratio is between these values. The type of wave has, among other things, effects on the horizontal and vertical velocities and the orbital wave trajectories of fluid particles.

2.2. Range of study

2.2.1. Environmental design conditions

The environmental wave conditions in which the NMS is deployed are important in determining the fluid velocities and accelerations that can be used in Equation 1.15, and to determine the value of the nondimensional numbers Re and KC. However, the environmental wave data are unknown, as the location where the NMS will be deployed is not defined in a specific way. The most realistic environmental waves are irregular on the sea, which can be seen as superpositions of harmonic waves [44]. Typically, waves are recorded, and with the use of statistics, the wave periods and significant wave height are determined. The significant wave height is the average wave height of $\frac{1}{3}$ of the highest recorded waves, which are the waves with the highest energies. The range of wave periods is based on the scatter table in a North Sea zone provided in the study by Elzinga et al. (2024), where monopiles are installed with water depths up to 68 metres [45]. Wave periods between 5.0 and 8.0 s have been found to be the most common in this area. Therefore, in this study, a range of wave periods between 4.5 and 9.0 seconds is used to set design parameters. However, this study only mentions the average significant wave height and not the maximum operating limit wave height. Guachamin et al. (2016) evaluated operational limits during monopile installation by conducting a case study using a heavy lift vessel and concluded a maximum significant wave height of H_s = 1.5 m [46]. Nevertheless, the paper notes that this limit depends on design parameters that are different in engineering projects. In this study, a wave height of 2.5 m is used to analyse hydrodynamic loads under broader wave conditions.

Table 2.1 shows an overview of the regular wave design conditions of the NMS and includes wavelength, amplitude, and frequencies for wave periods between 4.5 and 9.0 seconds and a water depth of 40 metres.

Table 2.1: Real environmental wave conditions.

Wave design conditions	**Variable**	**Deep water**			**Intermediate water**		
Wave period (s)	T	4.50	5.50	6.5	7.50	8.50	9.0
Wave frequency (rad/s)	ω	1.40	1.14	0.97	0.84	0.74	0.70
Wavelength (m)	λ	31.6	47.2	65.9	87.3	110	122
Wave number ($\frac{1}{m}$)	k	0.199	0.133	0.095	0.072	0.057	0.051
Wave height (m)	H	2.5	2.5	2.5	2.5	2.5	2.5
Wave steepness (-)	H/λ	0.079	0.053	0.038	0.029	0.023	0.020
Depth-to-wavelength ratio (-)	h/λ	1.27	0.85	0.61	0.46	0.36	0.33

It can be observed that the values of the wave steepness for the first two wave periods are relatively high, as a result, higher-order wave effects are more significant for these periods compared to the longer wave periods. However, this study adopts the linear wave theory in subsequent calculations for several reasons. This theory is analytically more tractable compared to higher-order theories, and linear methods are generally widely accepted [44]. Furthermore, wave effects decrease exponentially with e^{-nkz}, where n is the order of the wave. This leads to higher-order wave effects decreasing more rapidly than first-order wave theory for increasing depth. This is worth emphasising because this study also focuses on deeper-positioned panels.

Figure 2.2 illustrates the particle trajectories for the wave periods of 4.50, 6.75 and 9.00 seconds with H = 2.5 metres for the first 40 metres. It can be concluded that, with increasing depth, the orbital amplitudes and velocities decrease, and that this phenomenon occurs more rapidly for waves with shorter periods than for those with longer periods. Additionally, the orbital trajectory for the wave period of 9.0 seconds has an elliptical shape instead of the circular shape of the lowest wave period, so the water depth is intermediate for this wave period. This results in slightly higher maximum horizontal velocities than maximum vertical velocities. The highest values of Re and KC are found near the water surface as a result of higher particle velocities and orbital amplitudes. Moreover, higher velocities and accelerations result in higher loads according to Equation 1.15.

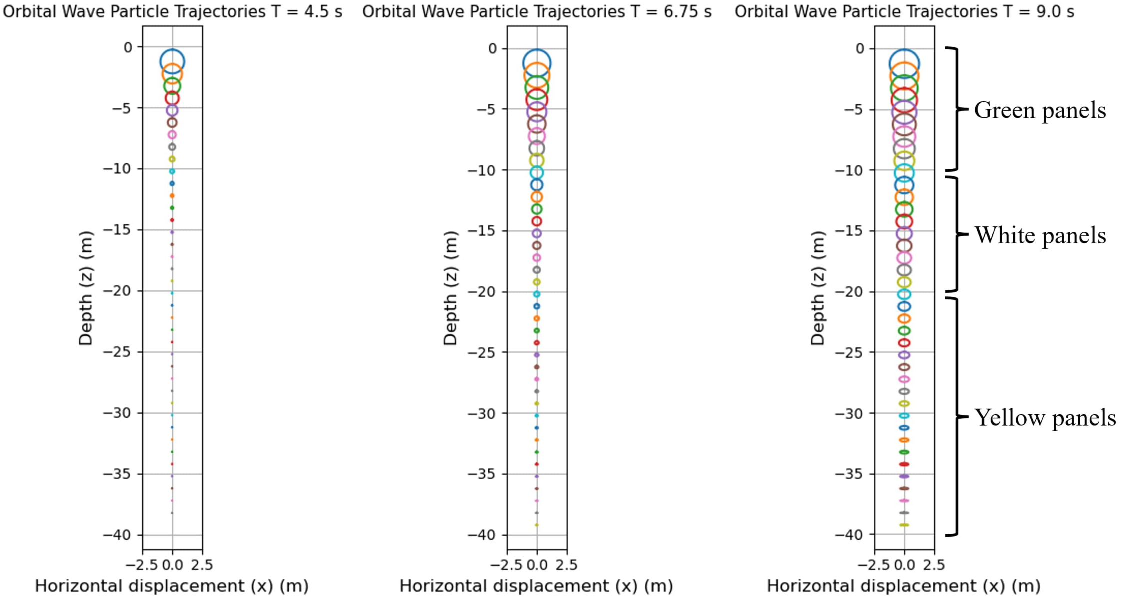

Figure 2.2: Wave particle trajectories for the first 40 meters for wave periods T = 4.5 s, T = 6.75 s and T = 9.0 s. The difference in height between each centre point of the orbital trajectory is 1.0 metres.

2.2.2. Panels in this study

This study will only focus on the green and white panels arranged in the first 20 metres. There are three main reasons for this. Firstly, the most dominant forces, which are of most interest, are expected near the water surface, as a result of which the hydrodynamic loads on the panels arranged near the water surface are most relevant. Secondly, there is a limitation in the test time with the result that the choice has been made to neglect the determination of the hydrodynamic coefficient of the yellow panels. Third, the panels have the same length and width dimensions, and the perforation ratios are almost identical, resulting in geometric similarities between the panels. However, the differences in the hydrodynamic coefficients will be quantified between the green and white panels.

2.2.3. Simplification of the AdBm panel geometry to align with literature

There are several motivations for simplifying the complex geometry of AdBm panels. Firstly, the geometry of the AdBm panels can be simplified to models that look similar to previous studies to decrease the research gap. The results of the experiments can be validated using knowledge from the literature to identify similarities and to assess whether the previously discussed effects of KC, Re, and geometry are comparable. Moreover, numerical simulations have already been performed on different perforated objects, and using a similar model could provide more insight into fluid behaviour around the model. However, it is essential to justify the simplifications to ensure that the simplified model remains representative of the real panels.

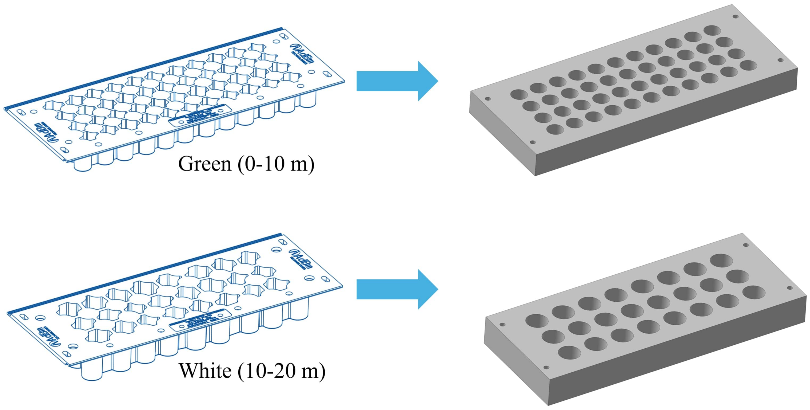

Figure 2.3: Simplified models based on the real AdBm panels.

Figure 2.3 shows the simplified models based on real AdBm panels. The design steps that are used to reach the final design of the simplified models are listed below.

- Simplified models have the same length, width, and height as the original panels. The height is based on the height of the cups. There is a difference in the height of the green and white panels, resulting in different heights for both models.
- It has been explained that the inertial effects of the mass-spring system inside the cups can be neglected because of quasi-static behaviour. For this reason, the simplified models are solid to remove complex and irregular hollow circular cylinders.
- The perforation ratio is based on the original panels, and the number of holes is the same as the number of complicated-shaped holes. The holes are circular because this hole geometry is commonly used in the literature. The diameter of the hole is based on the surface of the open area. It has been mentioned that in previous studies the values of the hydrodynamic coefficients of models with the same perforation ratio but different hole sizes are almost identical. This makes this simplification possible.

These design arguments are used to get simplified panels that represent the original ones. Experimental tests on the original green panels are conducted to assess the effects of the aforementioned design simplifications. The green panel is chosen for the reason that the highest loads are expected on this panel because these are vertically arranged near the water surface, making this panel more interesting. The next subsection explains the final models that are used in this study to achieve the objective of this study.

2.2.4. Perforated panels used for experiments

Figure 2.4 shows the models that are used in this study. The two models on the right are the simplified models. The simplified model with the smaller hole size is shown in the middle and is named model SH. The simplified model with the bigger hole size is shown on the right and is named model BH. The panels are attached to H-shaped frames, which keep the panels arranged next to each other to form a slat, and are typically used in practice. The relevant properties of the three panels are listed in Table 2.2. The perforation ratio is equal to the open area divided by $L \times W$.

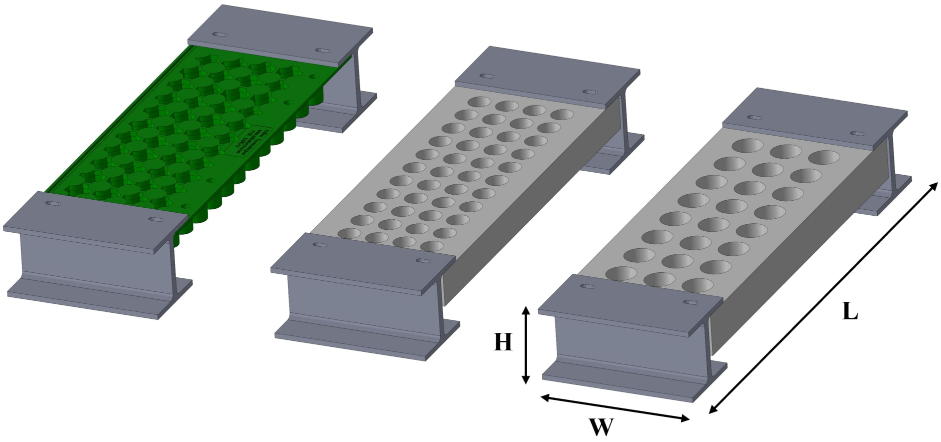

Figure 2.4: 3D models of the panels used in this study. Left: green AdBm panel; middle: panel with a smaller hole size (model SH); right: panel with a larger hole size (model BH).

Table 2.2: Panel properties

Variable	Symbol	AdBm panel	Panel with smaller hole size	Panel with larger hole size
Model length (mm)	L	758	758	758
Model width (mm)	W	240	240	240
Model height (mm)	H	114	114	114
Panel thickness (mm)	t_p	53	53	65
Number of holes	n_h	44	44	24
Hole diameter (mm)	D_h	n/a	34	46
Perforation ratio	τ	0.22	0.22	0.22

2.2.5. Range of KC and Re in this study

Figure 2.5 illustrates the Re and KC numbers using equations 1.2 and 1.3. The maximum velocities of the wave particles from equation 2.1 are taken, and the characteristic length is the length of the panel, including the outer frames. Since the model may be deployed at various locations in the sea, a representative water temperature of 13 degrees is assumed to estimate the kinematic viscosity, which is taken as 1.25 $\times 10^{-6}$ m^2/s. The depth increases from the top to the bottom of the figure with steps of 1.0 metres from 0 to 20 metres. An important point is that this study focuses on fully submerged panels, and slamming effects are therefore not considered. Therefore, the starting depth is taken as the value of the wave amplitude of 1.25 metres.

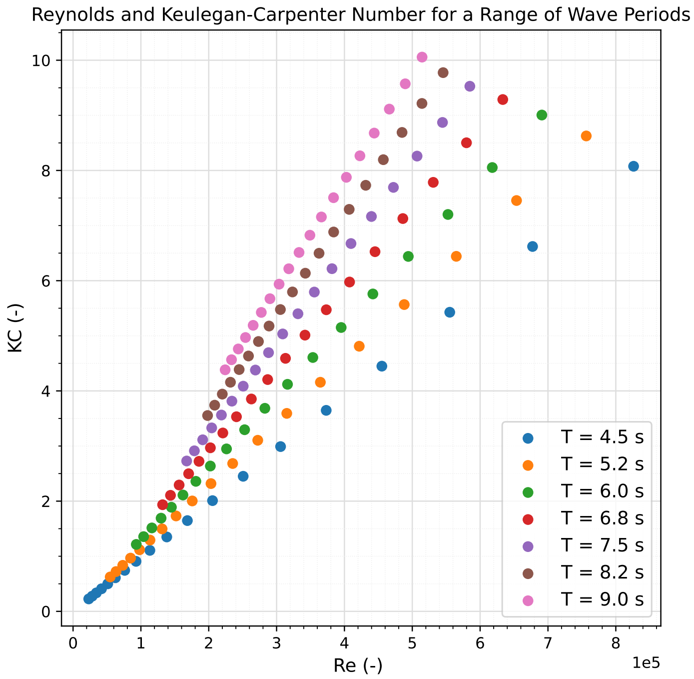

Figure 2.5: The Reynolds and Keulegan-Carpenter numbers for the first twenty fully submerged panels for a range of wave periods.

An overview of the range of Reynolds and Keulegan-Carpenter numbers in Figure 2.5 are given in Table 2.3, for the lowest, centre, and highest wave periods. It can be seen in Figure 2.5 that the lowest and highest wave periods determine the maximum and minimum values of KC. In other words, wave periods between 4.5 s and 9.0 s result in KC values between the resulting values of the highest and lowest wave periods. The test time is limited, and therefore, it is chosen to perform experimental tests for a limited range of three periods. This choice was also made because it is expected from previously described literature in Section 1.6 that frequency has little to no influence on the value of hydrodynamic coefficients in forced oscillation tests. However, by testing three different frequencies, the effect of the frequency will be investigated. Therefore, the values of KC and Re in Table 2.3 are the range in which the values of the hydrodynamic coefficients must be determined to accurately find the total hydrodynamic loads on the panels.

Table 2.3: KC and Re ranges for different depths and wave periods.

Depth (m)	0 – 10			10 - 20		
Wave period (s)	4.5	6.75	9.0	4.5	6.75	9.0
Wave frequency (rad/s)	1.40	0.93	0.70	1.40	0.93	0.70
KC	1.4 - 8.1	4.2 - 9.3	6.5 - 10.1	0.3 - 1.4	1.9 - 4.2	4.4 - 6.5
Re $[\times 10^5]$	1.4 - 8.3	2.9 - 6.3	3.3 - 5.1	0.2 - 1.4	1.3 - 2.9	2.2 - 3.3

2.3. Experimental limitations

The aim is to perform model tests with the nondimensional conditions given in Table 2.3. However, there are limitations in the test facility, test conditions and test time which make it impossible to reproduce the exact wave conditions given in Table 2.1. This section describes the limitations and associated consequences that it has on the experiments.

2.3.1. Test facility

The tests will be carried out in the small towing tank at Delft University of Technology, whose dimensions are provided in Table 2.4. The research objective is to find the hydrodynamic coefficients in the vertical heave direction and the horizontal surge direction. The depth of the towing tank is 1.5 m, and the water level is chosen as 1.1 m, making it difficult to perform forced oscillations in the vertical direction, especially when multiple panels are used to assess interaction effects. For the highest KC value of 10.1, an oscillation amplitude of 1.22 m is needed for an unscaled model using Equation 1.4, which is significantly higher than the depth of the water. However, it has been investigated that the mass-spring system of the water and air in the cylindrical cups does not have a hydrodynamic influence. Combined with the fact that there is enough space in the horizontal oscillation direction, this makes it interesting to orient the test model 90 degrees to perform the heave oscillation test in the horizontal direction. Moreover, the large amount of space in the horizontal direction is a significant advantage in investigating interaction effects using multiple models.

Table 2.4: Dimensions of TU Delft Towing Tank No. 2 [47].

Wave Tank No. 2	
Length [m]	85.0
Width [m]	2.75
Water depth [m]	1.10

2.3.2. Forced oscillation

There are limitations in forced oscillation tests related to the amplitude and velocity of the oscillation. The oscillation tests will be performed on a towing carriage in which the available space is limited, resulting in limitations in the maximum achievable amplitude and thus KC values. The total space inside the towing carriage to perform the oscillations is 3.2 metres. In this area, a linear motor, a slider, and a moving frame must be fitted. Therefore, a maximum design stroke is set to 1.20 metres in which the oscillations are performed. The maximum oscillation velocities are 1.3 and 2.0 m/s for input voltages of 48 V and 72 V, respectively [48].

Table 2.5 contains the amplitude needed in the oscillation for the highest KC number when using a 1:1 scaled model and using Equation 1.4. This value is compared to the maximum design amplitude mentioned earlier. It can be concluded that it is impossible to reach the maximum KC value with an unscaled model, and therefore, it is necessary to scale the model. The ratio $\frac{A_{needed}}{A_{max}}$ is equal to 2.03, which is the minimum scaling factor needed.

Table 2.5: Maximum amplitude compared to the needed amplitude.

		A_{needed} (1:1)	A_{max}	$\frac{A_{\text{needed}}}{A_{\text{max}}}$
KC	10.1	1.22 m	0.60 m	2.03

2.3.3. Wave maker capabilities

Figure 2.6 illustrates the wave limits of the small towing tank at the Delft University of Technology. This graph was provided by Peter Poot, head technician of the ship hydromechanics lab. The blue line in this figure is an estimation of which wave amplitude and frequency combination is possible in the tank. Waves with amplitude and frequency combinations in the area below the blue curve are possible to generate. The limiting factor of the region where the blue line increases is the maximum achievable wave amplitude that the wave maker is able to generate. On the other hand, in the region where the blue line decreases, the steepness of the wave is the limiting factor, which is set to not exceed $\frac{H}{\lambda} < 0.08$. Another limit is the water level of the tank, which is important in the type of wave that is generated. The tank water level is set at 1.1 metres, and with the use of Equations 2.3 and 2.4 and the deep water limit ($\frac{h}{\lambda} > 0.5$), deep water waves are generated for frequencies higher than 5.3 rad/s. This is relevant for the reason that the panels are exposed to deep water waves for lower wave periods using Table 2.1. It becomes clear from Figure 2.6 that it is not possible to reconstruct the wave conditions from Table 2.1 and, therefore, scaling laws must be applied

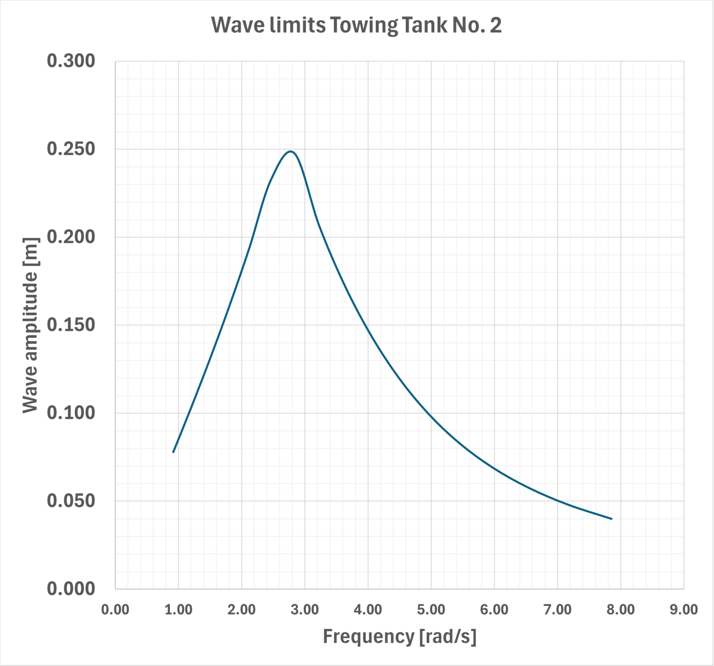

Figure 2.6: Wave limits of Towing Tank No. 2.

2.3.4. Scaling

Scaling laws are often used in model tests to maintain geometry, kinematics, and dynamics during model tests. A commonly used scaling law in practice is the Froude scaling. Table 2.6 shows the conversion factors using the Froude scaling law [49]. However, the water in the towing tank is not replaced with another liquid, which results in the fact that the viscosity is not scaled. As a consequence, the Reynolds numbers in the experiments are typically smaller than in reality and therefore smaller than in Table 2.3. However, the effect of the Reynolds number can be evaluated by testing different frequencies at the same oscillation amplitude in the forced oscillation tests. This can be explained by substituting the maximum oscillation velocity $u_{max} = A_{osc}\omega$ in Equation 1.2. The Reynolds number scales with $\alpha^{1.5}$, which means that the Reynolds number is closer to reality for the lower scaling factor.

Table 2.6: Froude scaling conversion factors

Variable	Unit	Scale Factor
Length	m	α^1
Area	m^2	α^2
Volume	m^3	α^3
Density	$\frac{kg}{m^3}$	α^0
Time	s	$\alpha^{0.5}$
Frequency	s^{-1}	$\alpha^{-0.5}$
Velocity	$\frac{m}{s}$	$\alpha^{0.5}$
Acceleration	$\frac{m}{s^2}$	α^0
Force	N	α^3

The most challenging part is to generate waves in the towing tank that are consistent with the waves described in Table 2.1 with the geometry kept representative. For example, to generate a wave that is representative of a deep water wave of 4.5 s and a wave height of 2.5 m, a scaling factor of 14.4 is needed. This scaling results in a model length of 0.05 m, which is too small. In addition, the water level of the tank is 1.1 metres, which is 36 times less than the water depth in reality. Consequently, the limits of the towing tank are so limited that the fluid kinematics cannot be regenerated by using a representative geometry. This results in the fact that the maximum KC values, which are related to the panels positioned near the surface, cannot be achieved. However, KC values decrease with increasing depth, which leads to opportunities to determine hydrodynamic coefficients for deeper arranged panels.

In contrast with the wave tests, the forced oscillation tests do offer the possibility to reach the maximum KC value using a model that is representative of reality. This is an additional reason to perform forced oscillation tests. From Table 2.5 can be concluded that a minimum scale factor of 2.03 is needed to achieve the maximum KC value. Ultimately, a scaling factor of 2.5 is taken in the experiments for the reasons given below.

1. The aim is to use a model in the experiments in which the geometry is close to the original model as much as possible to limit the differences in the real Reynolds numbers and the experimental Reynolds numbers.
2. The 2.5 scaling factor makes it possible to reach the maximum KC value with the available oscillation space, which is the most dominant variable in the value of the hydrodynamic coefficients.
3. A scaling factor of 2.0 is enough to reach the maximum KC value in the forced oscillation tests, but a scaling factor of 2.5 is chosen. This leads to a KC of 12.4, which can be reached using the maximum oscillation amplitude of 0.60 m. First, the range of study is based on the wave design conditions given in Table 2.1, but it is not unlikely that there are waves present with a higher significant wave height or longer wave periods. From Table 2.3 can be concluded that longer wave periods result in higher KC values. Moreover, the KC number is linearly related to the wave amplitude by substituting Equation 2.1 and Equation 2.2 in Equation 1.3. This means that the results are relevant for wave heights that are 1.23 times higher than the design wave height of 2.5 m.
4. The maximum achievable amplitudes for the scaled wave frequencies are given in Figure 2.7. The scaled frequencies are capable of reaching a KC value of 5.4, 5.2 and 4.3 related to the wave periods of 4.5, 6.75 and 9.0 seconds, respectively. The maximum KC value related to the wave period of T = 9.0 seconds is less than the minimum KC value provided in Table 2.3. Forced oscillation results can be compared with the results of the wave tests up to a KC of 5.4 related to the wave period of 4.5 seconds and up to a KC of 5.2 for the wave period of 6.75 seconds.

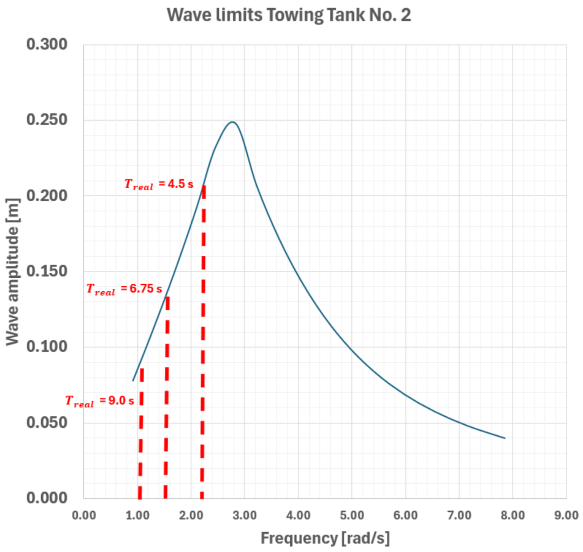

Figure 2.7: Wave limits of the towing tank, including the scaled wave frequencies.

This scaling factor leads to the experimental design above the water surface depicted in Figure 2.8 and allows the moving frame, slider, and linear motor to fit in the available space within the towing carriage. The dark blue arrows show the maximum possible oscillation stroke with the distance in millimetres. The total stroke distance is 1.32 metres, leaving some margin with the design stroke of 1.20 metres. This design complies with the maximum design amplitude.

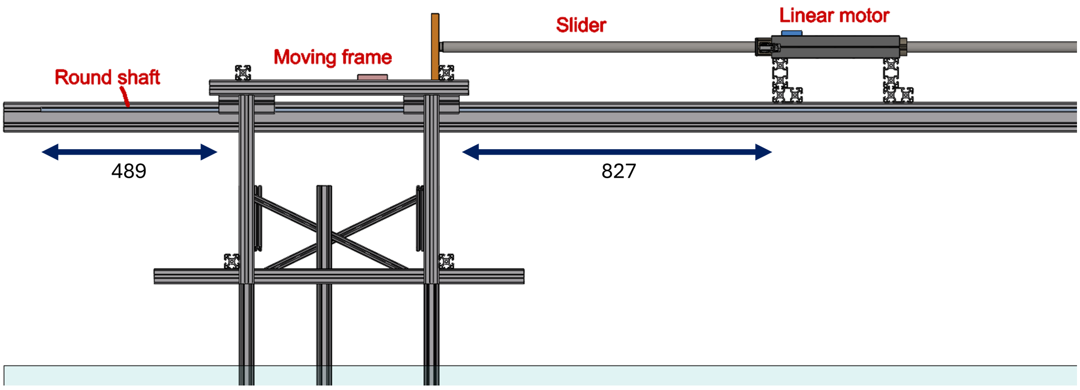

Figure 2.8: Maximum possible oscillation stroke for the oscillation tests.

3

Experiments

3.1. Test facility

The tests are conducted in the small towing tank at Delft University of Technology. The specifications of Towing Tank No. 2 are presented in Table 3.1.

Table 3.1: Dimensions of TU Delft Towing Tank No. 2 [47]

Wave Tank No. 2	
Length (m)	85.0
Width (m)	2.75
Water depth (m)	1.10

3.2. Models

Figure 3.1 shows the three scaled models that are used in the experiments, including the outer frames and the dimensions of the model. The panel with the larger hole size is shown on the left, the panel with the smaller hole size is depicted in the middle, and the AdBm NMS panel is depicted on the right. The model with the smaller holes is named model SH, and the model with the bigger hole size is named model BH. The properties of the panels are provided in Table 3.2. These properties are used for further analyses.

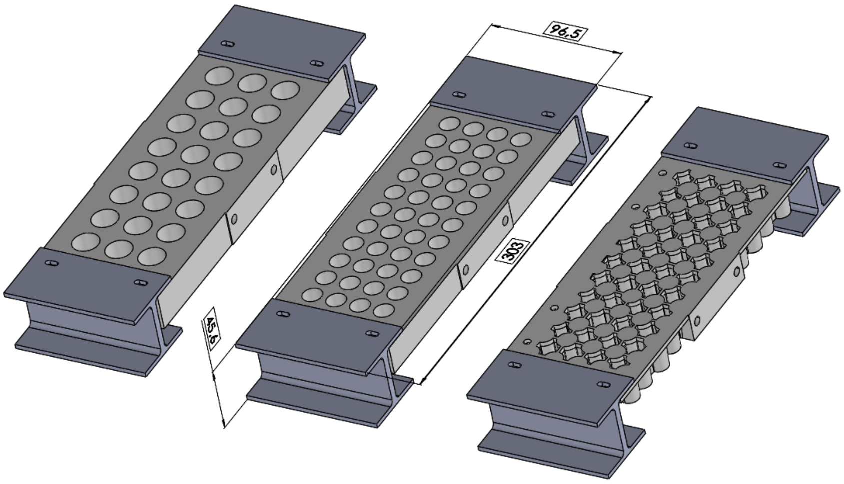

Figure 3.1: The three models that are used in the test.

Table 3.2: Model properties

Variable	Symbol	Panel with bigger hole size	Panel with smaller hole size	AdBm panel
Model length (mm)	L_m	303	303	303
Model width (mm)	W_m	96.5	96.5	96.5
Model height (mm)	H_m	45.6	45.6	45.6
Model volume (m^3)	V_m	5.45E-04	4.58E-04	2.74E-04
Model mass (kg)	M_m	0.31	0.30	0.26
Panel height (mm)	H_p	26	21	21
Amount of holes	n_h	24	44	–
Hole size diameter (mm)	D_h	18.5	13.6	–
Perforation ratio	τ	0.22	0.22	0.22

3.3. Experimental setup

This section describes the experimental setup used to achieve the objective of this study. A picture of the experimental setup is shown in Figure 3.2, where the setup is connected to the green towing carriage. Figure 2.8 is used to explain how an oscillating motion is generated. A linear motor is used to perform the oscillations. This is an electromagnetic direct drive that contains windings. To generate a linear motion, a slider containing magnets moves through the motor. The linear motor is connected to a sine wave generator where the oscillation amplitude and frequency can be set. The slider is connected to a wooden board that is connected to a moving frame that can move horizontally using wheels on a round shaft.

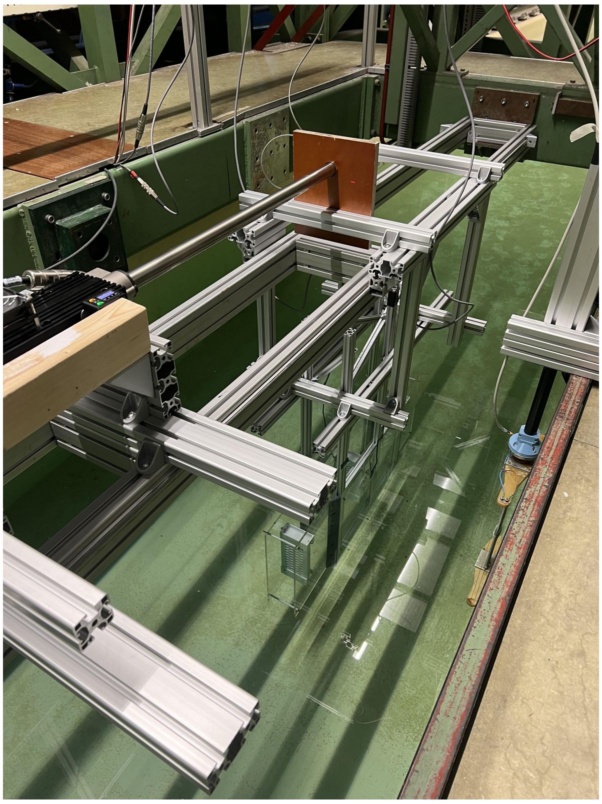

Figure 3.2: Picture of the experimental setup.

Figure 3.3 shows the side view of the whole setup with relevant dimensions in millimetres. Three different configurations are used in the experiments and are illustrated in Figure 3.4. Figure 3.4a shows the configuration using three vertically orientated panels. This configuration is used to measure the hydrodynamic loads in the heave direction and investigates the interaction effects between the panels. Figure 3.4b shows the configuration using one panel to compare the value of the hydrodynamic coefficients with the configuration using three panels. Figure 3.4c shows the configuration that is used to determine the coefficients in the surge direction.

Aluminium ITEM profiles with sizes 80x40, 40x40, 40x20 and 20x20 mm are used and connected. The water level is 1.1 metres and the distance from the top of the model to the water surface is 0.3 metres. There is enough space between the water surface and the horizontal beam above for the required waves. The fully submerged section is attached to the moving frame, causing this part to follow the same motion. Aluminium 40x20 profiles are used for the underwater section to minimise flow disturbances.

It is explained in Chapter 1 that the system is divided and the loads will be determined on a single panel, including frames. Two end plates are used to prevent fluid from flowing along the longer edges, thereby creating a two-dimensional flow regime because panels are arranged next to each other in practice. These end plates are made of PMMA and have a thickness of 6 millimetres. Both plates are connected to three vertical profiles to create more plate stiffness. Crossed 20×20 profiles are attached to the tops of the six vertical profiles to increase structural stiffness. Additionally, the plates are connected by four 3D-printed circular hollow rods in the corners to prevent bending of the PMMA plate in the areas near the corners. The front view and the isometric view are illustrated in Figures 3.5a and 3.5b, respectively.

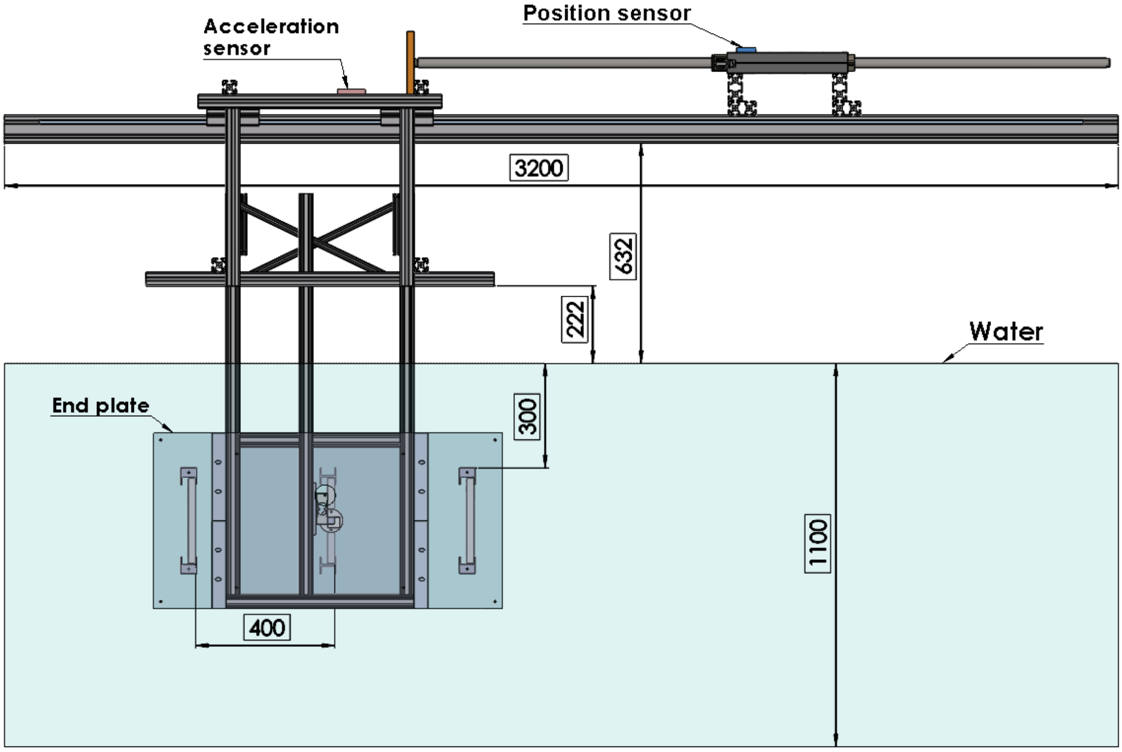

Figure 3.3: Side view of the experimental setup from Solidworks. The numbers are dimensions in millimetres.

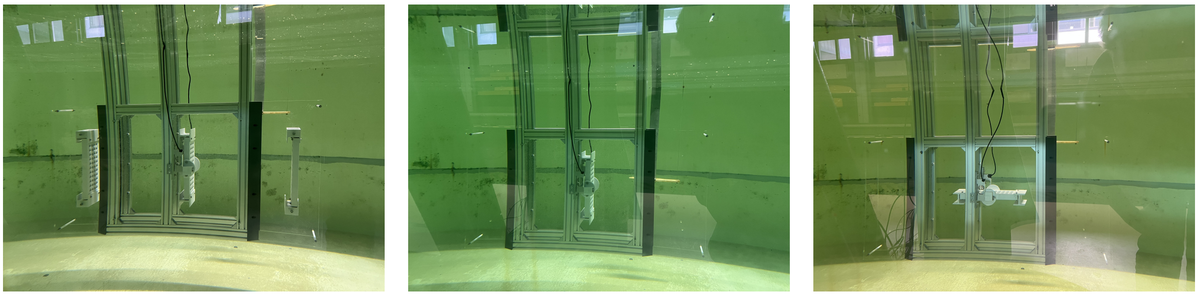

(a) Three vertically orientated panels in series.

(b) One vertically orientated panel.

(c) Horizontally orientated panel.

Figure 3.4: Three different panel configurations used in the experiments.

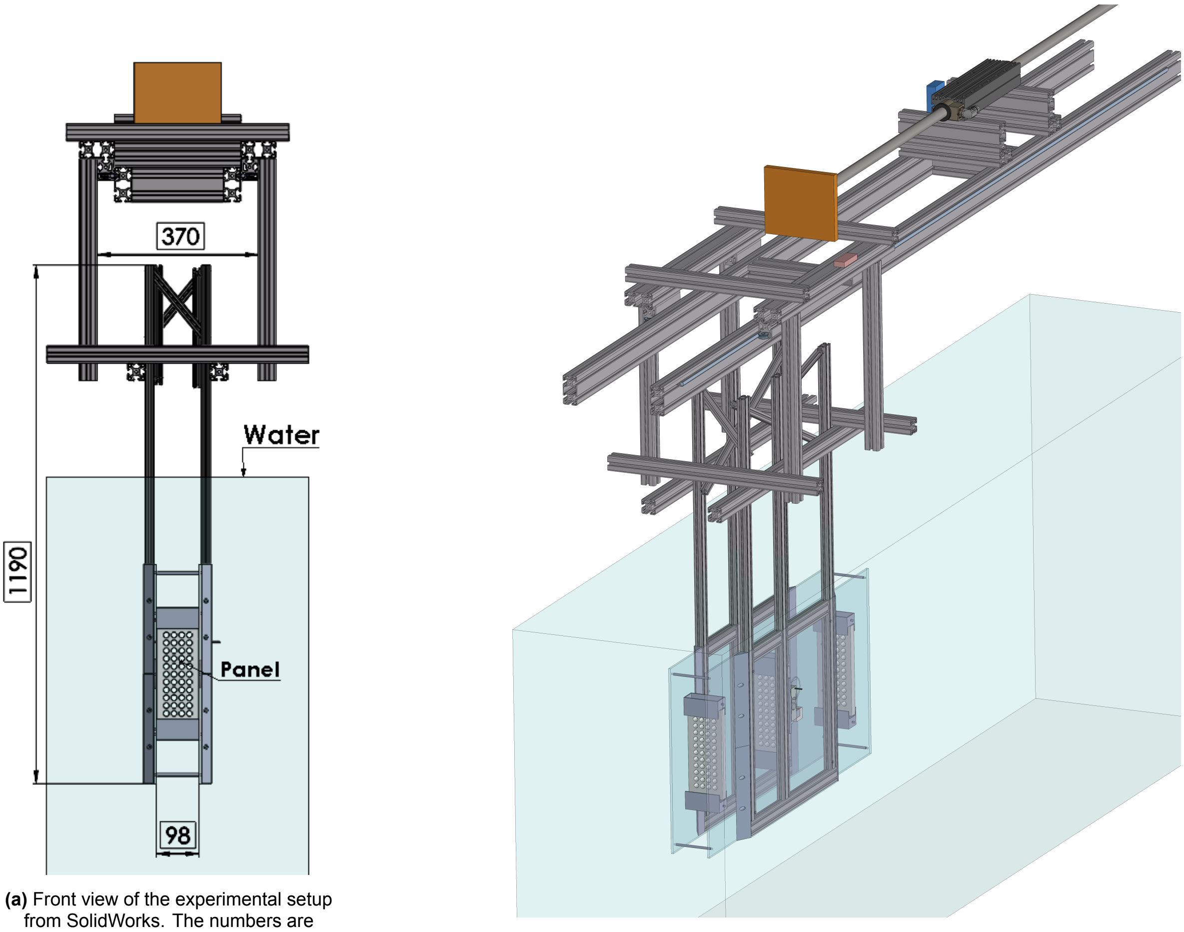

(a) Front view of the experimental setup from SolidWorks. The numbers are dimensions in millimetres.

(b) View from above of the experimental setup.

Figure 3.5: Two views of SolidWorks sketches of the setup.

Figure 3.6a provides a closer look at the end plates with labelled important components. Important parts are explained in more detail below.

- The circular disc, small block, wings, panels, and panel frames are 3D-printed.
- Two load cells are used to measure the total load in the horizontal direction. Both load cells can be seen in Figure 3.6b. It is important that the load cells do not affect the flow of the fluid around the model and are positioned for this reason on the outside of the end plates. Two load cells are used so that the model cannot rotate around the vertical axis and the entire horizontal force on the model is measured. The load cells are only capable of measuring forces in one direction. However, the aim of the present study is to determine the hydrodynamic coefficients in the horizontal (surge) and vertical (heave) directions. A circular disc is designed and connected to the panel and load cell, making it possible to rotate the panel 90 degrees to measure the loads on the panel in two directions without changing the position of the load cells. Figure 3.6b shows a closer view of one load cell and the configuration in which the model is orientated horizontally. Both load cells are connected to the middle of the longer edges of the panels in the centre by a small block and a circular disc. It is possible to disconnect the panel from the disc to change the models in Figure 3.1. The load cell is attached to an aluminium block, which is attached to the vertical 40x20 centre aluminium profile.
- The circular disc goes through the end plate with a clearance of 0.75 mm on the side to ensure that the load cell measures the force well. The maximum deflection of the load cell is 0.3 millimetres, and as a result, the circular disc is not able to make contact with the end plate and therefore will not affect the test results. Similarly, there must be a small space left between the panel and the end plates to prevent friction. Therefore, there is 0.75 millimetre space between the longer

edges of the panel and the inside of the end plates. The clearance between the panel and the end plates and between the circular disc and the end plates can be observed in Figure C.1a and Figure C.1b.

- A side plate is placed on the sides of the 40x20 profiles to prevent flow disturbances during oscillations. For the same reason, triangle-shaped wings are attached to the sides of the 40x20 vertical profiles.

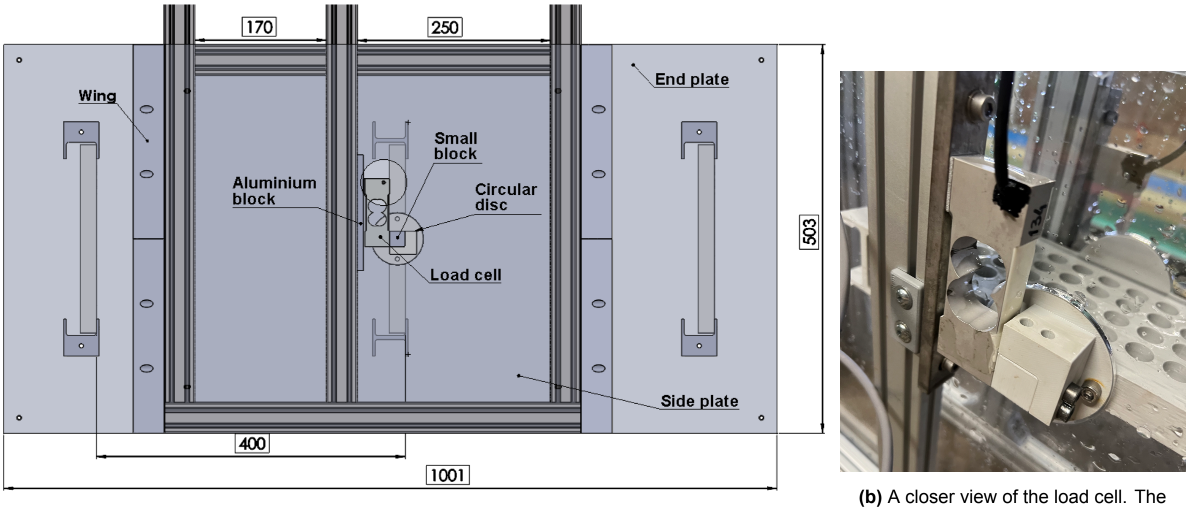

(a) Closer view of the side view sketch of the end plates. The numbers are the dimensions in millimetres.

(b) A closer view of the load cell. The panel is rotated 90 degrees to measure horizontal forces on the panel.

Figure 3.6: Two closer views of the end plates.

3.4. Measurement equipment

Table 3.3 provides an overview of the measurement devices used in the setup, including their measurement range and uncertainty. Measurement devices are used to determine the forces, position, acceleration, and elevation of the waves. The load cells and wave height sensors are calibrated, and the results are provided in Appendix A. The location of the position sensor and the acceleration sensor is shown in Figure 3.3, and both are used for forced oscillation tests. The position sensor measures the distance from the moving wooden board, and the data is used to check the (sinusoidal) oscillation motion of the panel because the panel follows the motion of the moving frame. The acceleration sensor is attached to the moving frame to measure the acceleration of the oscillation.

Table 3.3: Overview of the measurement devices.

Name	Measurement device	Measurement range	Uncertainty	Value
Load cell 1	Zemic L6J-C3D-3kg-0.45B	± 30 N	Averaged normalised residual	± 0.01%
Load cell 2	Zemic L6J-C3D-3kg-0.45B	± 30 N	Averaged normalised residual	± 0.008%
Position sensor	Baumer OM70-11112012	150 - 1500 mm	Linearity error	± 0.32%
Acceleration sensor	NXP MMA3201KEG	$\pm 40g$	Linearity error	± 1.0%
Wave height sensor 1 (front)	TU Delft	± 200 mm	Averaged normalised residual	Table A.2
Wave height sensor 2 (model height)	TU Delft	± 200 mm	Averaged normalised residual	Table A.2

Two wave height sensors are used in the wave tests to determine wave particle velocities and accelerations from the undisturbed incoming wave. One sensor is placed in front of the model to measure the wave elevation in time of the undisturbed wave. The second sensor is placed at the same lateral height as the model to measure the phase difference between the wave position of the wave sensor in front of the model and the model itself. The phase difference between the measured wave elevation of both wave height sensors is used to determine the velocities and acceleration of the undisturbed wave fluid particles in time. It is not possible to relate the undisturbed wave particle kinematics to the measured force without using two wave height sensors. Figure 3.7 contains a picture of the two wave height sensors. The distance between the sensors is 4.5 metres, and both wave height sensors are calibrated each day before the tests start.

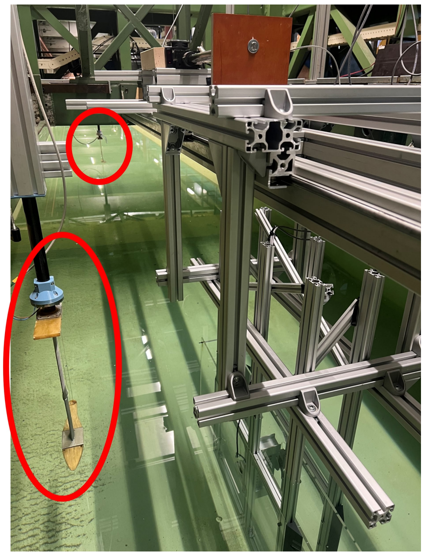

Figure 3.7: Picture of the wave height sensor in front of the model and on the same height as the model.

3.5. Data-acquisition

All data is converted from analogue to digital with a sample rate f_s of 1000 Hz. An analogue filter is used to prevent aliasing before A/D conversion. The sample rate is high enough because the highest oscillation and wave frequency is 2.21 rad/s, which is equal to 0.35 Hz. According to the Nyquist rule, the sample rate must be a minimum of twice the highest frequency for periodic signals [50]. The Zemic load cells are connected to a Peekel Picas multi-channel compact amplifier system. The load cells contain strain gauges in a Wheatstone bridge, which measures the change in resistance when the strain gauge deforms due to a force applied. This resistance change is converted into a voltage signal, which is amplified. The amplified signal is then converted into a force value in Newtons by a calibration factor given in Appendix A. The wave height sensors are connected to the TU Delft wave height meter with a +/- 10 V output. The calibration factors for both wave height sensors are given in Appendix A.

3.6. Test conditions

This section contains the test conditions for both the forced oscillation and wave tests that are used to answer the research questions.

3.6.1. Forced oscillation test conditions

Tables 3.4, 3.5 and 3.6 show the test plan applied in the forced oscillation test for the model with the smaller hole size, the model with the bigger hole size and the AdBm model, respectively. The limited test time leads to a limitation in the number of test amplitudes and frequencies. Because the KC number is more dominant than the Re number, the number of different amplitudes is higher than the number of different tested frequencies. Note that testing different frequencies using one amplitude investigates the effect of the Reynolds number. This can be explained by substituting the maximum oscillation velocity $u_{max} = \omega A_{osc}$ in Equation 1.2, where A_{osc} is the oscillation amplitude. The combination of KC number and frequency covers the range of study provided in Table 2.3. The oscillation frequencies are related to the wave frequencies given in Table 2.3 by applying the Froude scaling factor in Table 2.6.

The heave tests are the tests where the panel is orientated vertically, and the surge tests are the tests where the panel is orientated horizontally. The surge test and the heave test with a single panel and a panel in series are performed for the panel with the smaller holes. This covers the research on the effects of KC, Re, and interaction on the hydrodynamic coefficients. Due to the test time limit, only the heave test with one panel is conducted for the panel with a bigger hole size. This panel covers the study range for the panels that are arranged between 10 and 20 metres in Table 2.3. However, to investigate the effect of the hole size difference on the hydrodynamic coefficients, higher amplitudes are also taken for comparison. When performing the oscillation test using three models, the ratio between the distance of the models and the length of the model is 1.3. Using the findings in the study of Li, no hydrodynamic effects are expected for A = 0.07 m for the perforated panels in series used in this study [25]. Furthermore, too low forces are expected in the surge direction for A = 0.07 m, leading to the oscillation starting at A = 0.17 m for the surge oscillations.

Table 3.4: Forced oscillation test conditions for the perforated model with smaller hole size.

Model	**SH**	1 panel - heave			3 panels - heave			1 panel - surge		
KC	Amplitude (m)	Frequency (rad/s)			Frequency (rad/s)			Frequency (rad/s)		
1.5	0.07	2.21								
3.5	0.17	2.21	1.47		2.21	1.47		2.21	1.47	
5.5	0.26	2.21	1.47	1.10	2.21	1.47		2.21	1.47	
7.5	0.36	2.21	1.47	1.10	2.21	1.47	1.10	2.21	1.47	1.10
9.5	0.46		1.47	1.10		1.47	1.10		1.47	1.10
11.5	0.55			1.10			1.10			1.10
12.5	0.60			1.10			1.10			1.10

Table 3.5: Forced oscillation test conditions for the perforated model with bigger hole size.

Model	**BH**	1 panel - heave		
KC	Amplitude (m)	Frequency (rad/s)		
1.5	0.07	2.21		
2.5	0.12	2.21		
3.5	0.17	2.21	1.47	
4.5	0.22	2.21	1.47	
5.5	0.26	2.21	1.47	1.10
7.5	0.36		1.47	1.10
9.5	0.46		1.47	1.10
11.5	0.55			1.10
12.5	0.60			1.10

Table 3.6: Forced oscillation test conditions for the AdBm model

Model	**AdBm**	1 panel - heave			3 panels - heave			1 panel - surge		
KC	Amplitude (m)	Frequency (rad/s)			Frequency (rad/s)			Frequency (rad/s)		
3.5	0.17	2.21			2.21			2.21		
5.5	0.26	2.21	1.47		2.21			2.21		
7.5	0.36	2.21	1.47	1.10		1.47		2.21	1.47	
9.5	0.46		1.47	1.10		1.47			1.47	
11.5	0.55			1.10			1.10			1.10
12.5	0.60			1.10			1.10			1.10

3.6.2. Wave test

Table 3.7 shows the test parameters for the wave test with a fixed structure using the wave limits of Figure 2.6. The wave tests are performed on the model with the smaller hole size and the AdBm model. KC values are calculated with the maximum wave particle velocities of Equation 2.1 at the depth of the position of the load cells. The frequencies used in this table are below the deep-water frequency mentioned in Subsection 2.3.3, resulting in intermediate water waves being generated. As a result, the orbital wave particle trajectories have an elliptical shape.

Table 3.7: Test matrix for wave test with a fixed model.

Test type	Amplitude (m)	Frequency (rad/s)		KC	
Waves with one panel	0.05	2.21		1.4	
	0.09	2.21	1.47	2.4	3.7
	0.13	2.21	1.47	3.5	5.2
	0.17	2.21		4.5	
	0.20	2.21		5.4	
Waves with three panels	0.13	2.21		3.5	
	0.17	2.21		4.5	
	0.20	2.21		5.4	

3.6.3. Wave limits during installation

Before starting the experimental tests, the waves were set and it was found that the maximum wave amplitudes were significantly lower than expected. For ω = 2.21 rad/s, a maximum amplitude of approximately 0.12 m was reached, and for ω = 1.47 rad/s, around 0.09 m. This results in a maximum amplitude reduction of 58$\%$. The new amplitude and frequency parameters are listed in Table 3.8.

Table 3.8: New test plan for wave tests with fixed model.

Amount of panels	ω (rad/s)	Amplitude (m)
3	2.21	0.12
1	2.21	0.12
1	2.21	0.09
1	1.47	0.09
1	2.21	0.05

3.7. Test procedure

3.7.1. Forced oscillation test procedure

A total of 35 oscillation cycles are measured for each oscillation test, resulting in test times of 100, 150, and 200 seconds for the highest, middle, and lowest frequencies, respectively. A waiting time of 20-30 minutes is taken after each test, allowing the waves created on the surface by the previous test to dissipate.

3.7.2. Wave test procedure

The measurements are started immediately after the wave maker is started. The test time is based on the phase and group velocity of the wave, which are given in Equation 3.1 and Equation 3.2, respectively. The group velocity is the velocity of the energy of a group of waves that travels. The group velocity is used to know when the reflected waves from the beach reach the model. For intermediate water waves, the phase velocity and the group velocity are equal to Equations 3.1 and 3.2, respectively [44]. The phase velocity is equal to 2.99 and 3.15 m/s for the higher and lower wave frequencies, respectively. The group velocity for the wave with 2.21 rad/s is 2.48 m/s, and the group velocity for the wave with 1.47 rad/s is 2.91 m/s. The time it takes the waves to travel from the model to the beach and back is approximately 44 seconds for the higher-frequency wave and 38 seconds for the lower-frequency wave. Therefore, 12 wave cycles are used for the data processing for waves with a higher frequency and 7 cycles for the lower frequency waves. The duration of the wave test was set to 60 seconds. A thirty-minute waiting time is taken after each wave test until the waves are completely dampened.

$$c = \frac{\lambda}{T} = \frac{\omega}{k} \tag{3.1}$$

$$c_g = \frac{c}{2} \cdot \left(1 + \frac{2kh}{\sinh(2kh)}\right) \tag{3.2}$$

3.7.3. Test configuration order

First, tests are performed using three vertically orientated panels. The outer panels are then removed to perform the tests using a single vertically orientated panel. Lastly, the panel is rotated 90 degrees to perform the surge oscillation tests.

3.8. Data processing

This section describes how the data from the experiments will be analysed to be able to find the hydrodynamic coefficients. Both the post-processing for the forced oscillation tests and the wave tests will be handled.

3.8.1. Forced oscillation data processing

Firstly, the excitation of the oscillations is analysed. It is essential to associate the correct velocities and accelerations with the force signal to accurately determine the hydrodynamic coefficients. The velocity signal is determined from the position signal. Figure 3.8 contains two examples of a position signal for a random time interval. This figure presents the measured signal, a sinusoidal fit to the measured data, and a filtered signal. Although the motion is driven by a sine wave generator, the measured signal is not a perfect sine wave, as differences in the peaks can be observed in the figure. However, the frequencies of the input signal and the measured signal are in line with each other. The difference is because the linear motor does not convert the motion into a perfect sine wave. Very precise PID tuning is needed to achieve a perfect motion, however, this is time-consuming. The differences in the peaks increase with increasing oscillation velocity and the largest difference can be seen in Figure 3.8a. Assuming the position signal to be a perfect sine wave may lead to the use of incorrect velocity and acceleration in the determination of the hydrodynamic coefficients. For this reason, the low-pass-filtered position signal is used. This filtered signal fits with the measured position.

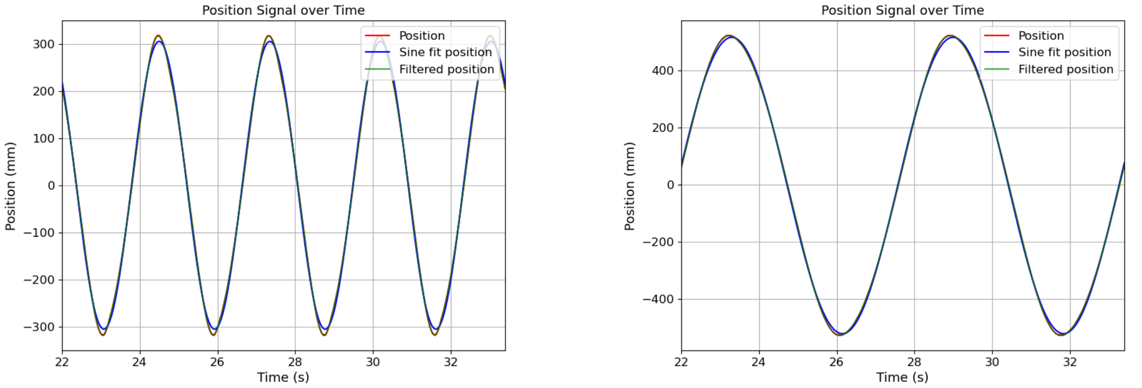

(a) Position signal, sinusoidal fit and filtered signal for A = 0.32 m, ω = 2.21 rad/s.

(b) Position signal, sinusoidal fit and filtered signal for A = 0.53 m, ω = 1.10 rad/s.

Figure 3.8: Comparison of position signals for different amplitudes and angular frequencies.

The velocity is determined by taking the derivative of the filtered position signal. This result can be observed in Figure 3.9, where the velocity and the velocity times the absolute velocity are plotted over time for A = 0.53 m and ω = 1.10 rad/s.

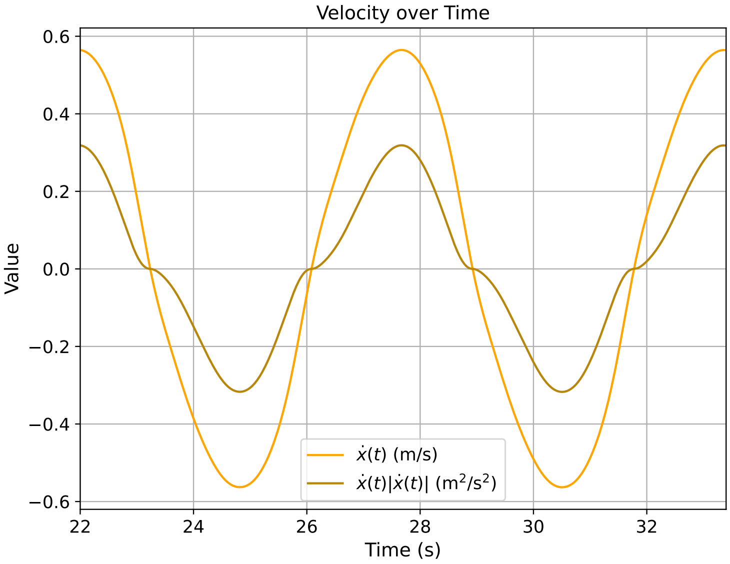

Figure 3.9: Example of the velocity and the velocity times absolute velocity signals in time derived from the position.

The acceleration signal was measured using an accelerometer. Two raw measured acceleration signals in time are shown in Figure 3.10 with on the left the lowest oscillation acceleration and on the right the highest oscillation acceleration. Both signals contain significant noise, and therefore Figure 3.11 is used to quantify the frequencies present in the raw measured acceleration signal of the oscillation test with the lowest and highest maximum acceleration value. Both signals contain a significant amount of peaks at different frequencies, which explains the noisy signal in the raw data. Probably, this noise originates from the vibrations of the moving frame during oscillation, to which the sensor is attached.

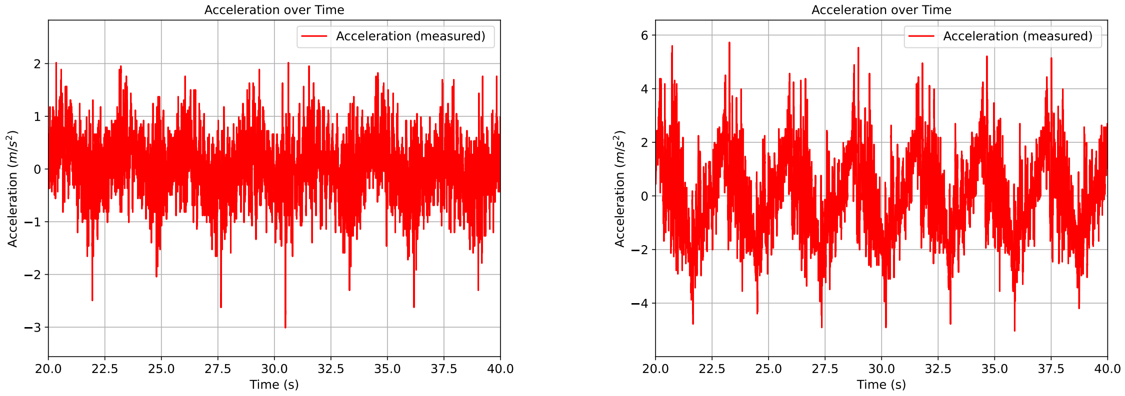

(a) Forced oscillation with ω = 2.21 rad/s and A = 0.07 m. **(b)** Forced oscillation with ω = 2.21 rad/s and A = 0.32 m.

Figure 3.10: Raw measured acceleration signal for two forced oscillation tests, with on the left the lowest maximum acceleration value and on the right the highest maximum oscillation acceleration.

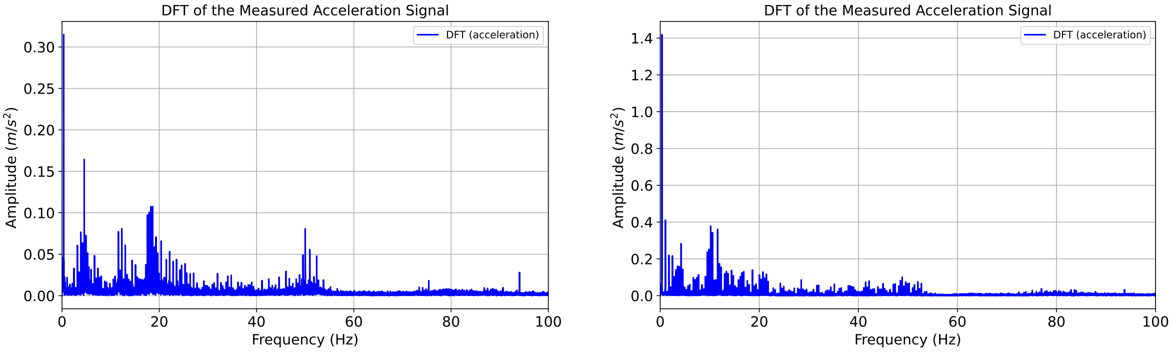

(a) Forced oscillation with ω = 2.21 rad/s and A = 0.07 m. **(b)** Forced oscillation with ω = 2.21 rad/s and A = 0.32 m.

Figure 3.11: DFT of the acceleration signal for two forced oscillation test, with on the left the lowest maximum acceleration value and on the right the highest maximum oscillation acceleration.

Two methods were applied to determine the acceleration:

1. The first method involves taking the derivative of the velocity.
2. The second method consists of carefully filtering the measured acceleration signal with the same cutoff frequency as for the force and the position signals.

Both methods and the measured acceleration are illustrated in Figure 3.12. It can be concluded that the blue and green lines mostly match each other. The acceleration resulting from applying the first method is taken to determine the value of the hydrodynamic coefficients because the second method consists of a precise filter process due to the high number of peaks in Figure 3.11. More interesting are the tests with a higher acceleration value. An example is illustrated in Figure 3.17. Each cycle period contains a small peak and trough on the positive slope side and on the negative slope side. This is related to the difference in the measured position and the sinusoidal fit of the position in Figure 3.8a.

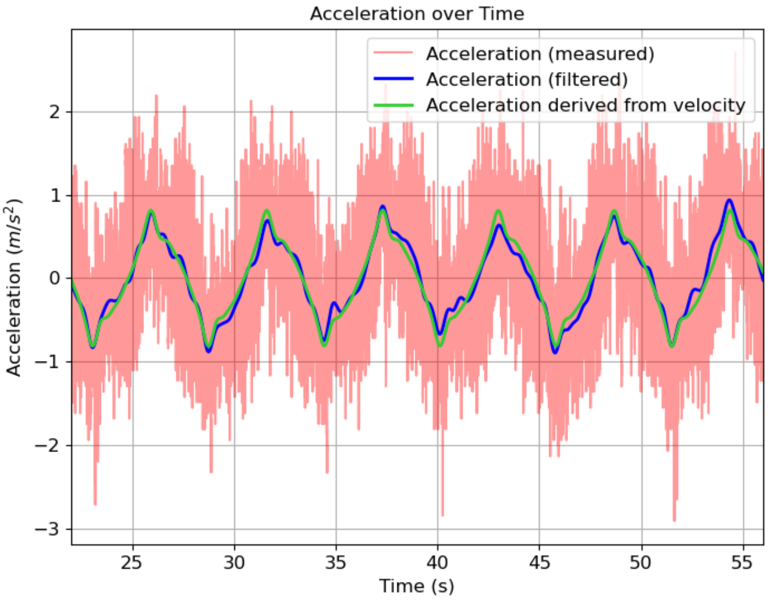

Figure 3.12: Measured and filtered acceleration and the acceleration derived from the velocity in time for A = 0.52 m and ω = 1.10 rad/s.

With the position, velocity, and acceleration signals determined, the force signals of both load cells are analysed. The raw data of a force signal is illustrated in Figure 3.13. It can be concluded from the figure that the signals are well in phase, which is checked for every run. This is important because both forces are added to each other to obtain the total measured force. In addition, the signal contains noise that needs to be filtered. This noise is related to the high-frequency vibrations that are present in the movement of the oscillations, as discussed earlier in the acceleration signals. It is essential for the filter process to investigate which frequencies are present in the force signal.

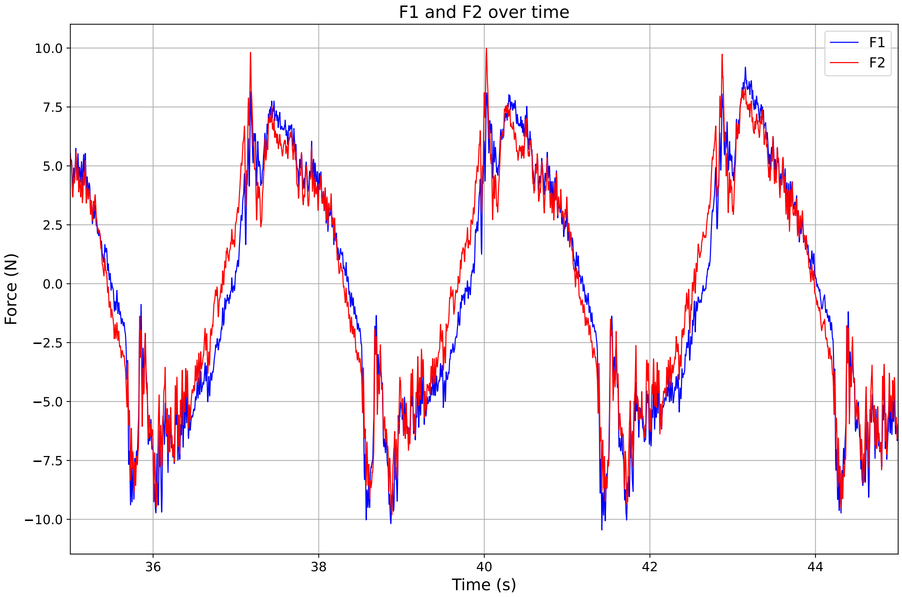

Figure 3.13: Force signal of both load cells of forced oscillation test with A = 0.25 m and ω = 2.21 rad/s for a single perforated model with small holes from t = 35 s to t = 45 s.

A Discrete Fourier Transform (DFT) is applied to indicate which frequencies are dominant in the force signals. This method transforms the discrete-time signal into the frequency domain and shows which frequencies are most dominant in the signal. An example is illustrated in Figure 3.14, where a DFT is performed on the two force signals. It can be seen that the frequency at the highest peak is the same as the input frequency. Another observation is that multiple peaks are visible in both Fourier transforms and that these peaks are exactly at the same frequencies for F1 and F2. An overview of the magnitude values and the corresponding peaks is given in Table 3.9. The frequencies of the peaks are positioned at higher orders of the first peak frequencies. The order of the frequency is determined with

$$\omega = n \cdot \omega_1, \tag{3.3}$$

where n is the order, ω_1 the oscillation frequency and ω the nth order frequency.

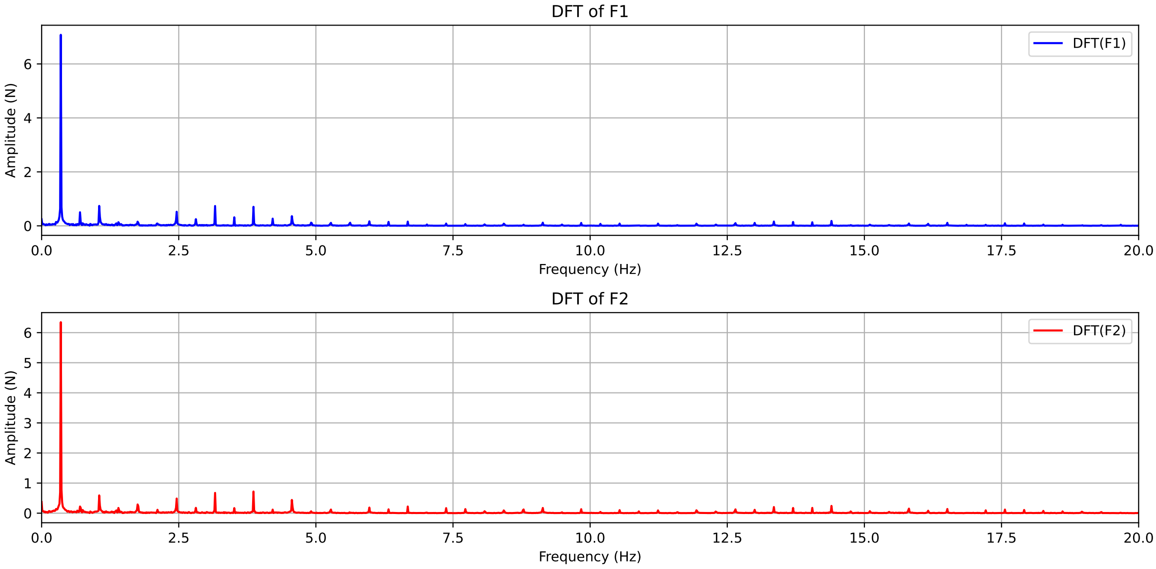

Figure 3.14: Discrete Fourier Transform of forced oscillation test with A = 0.25 m and ω = 2.21 rad/s for a single perforated model with small holes.

Table 3.9: Amplitude of the peaks from figure 3.14 with the corresponding frequency and the value of the frequency order.

Frequency (Hz)	Frequency (rad/s)	Order n	Magnitude F1 (N)	Magnitude F2 (N)
0.35	2.21	1	7.05	6.42
0.70	4.40	2	0.49	0.15
1.05	6.60	3	0.79	0.64
1.40	8.80	4	0.17	0.21
1.75	11.0	5	0.19	0.35
2.47	15.5	7	0.41	0.38
3.17	19.9	9	0.62	0.57
3.87	24.3	11	0.68	0.69
4.57	28.7	13	0.43	0.52

Since relatively low frequencies are used and no peaks can be seen below the oscillation frequency from the Discrete Fourier Transforms, a Butterworth low-pass filter is used to filter the force signal. It is important to choose the right cutoff frequency, because if filtering is done near the oscillation frequency, then there is a risk of hydrodynamic effects being attenuated [32]. Figure 3.15 and Figure 3.16 confirm this. These figures contain two oscillation periods and show that too low cutoff frequencies can cause possible hydrodynamic effects to be neglected and that higher orders tend toward the measured force signal. Figure 3.15 contains the oscillation with the highest maximum velocity and acceleration value, where peaks and troughs can be observed at the upper and lower extremes of the force signal. Figure 3.16 shows the filtered forces with a lower oscillation velocity than the figure above, and it can be seen that the filtered signals converge more rapidly. Therefore, the 9^{th} order of frequency is taken as the cutoff frequency for oscillations with a velocity higher than 0.5 m/s and the 7^{th} order for oscillations lower than 0.5 m/s. Additionally, higher orders of cutoff frequencies do not result in differences in the final value of the hydrodynamic coefficients.

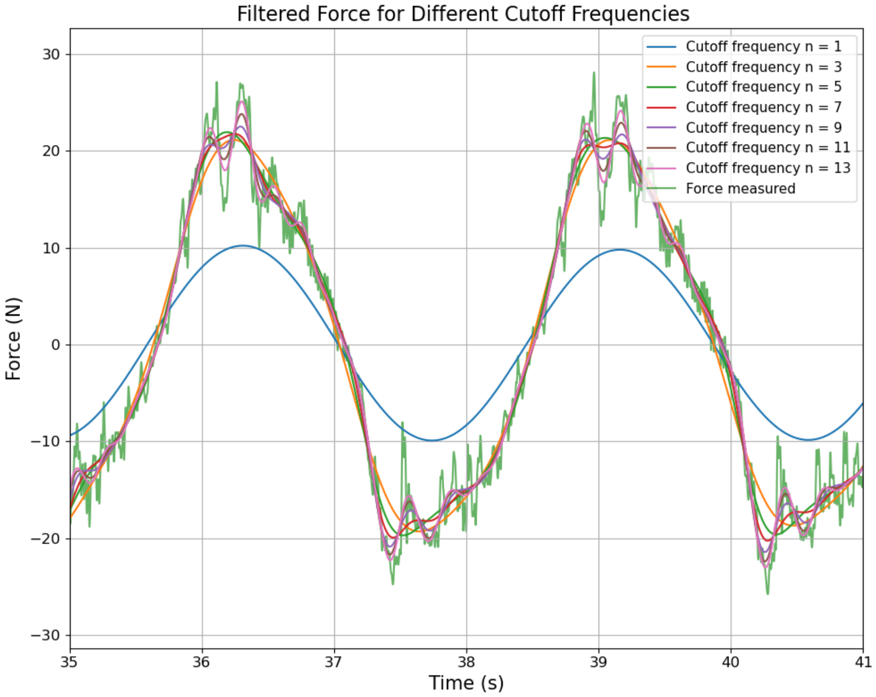

Figure 3.15: Measured force with ω = 2.21 rad/s for a single perforated model with small holes, A = 0.32 m and maximum oscillation velocity is 0.70 m/s.

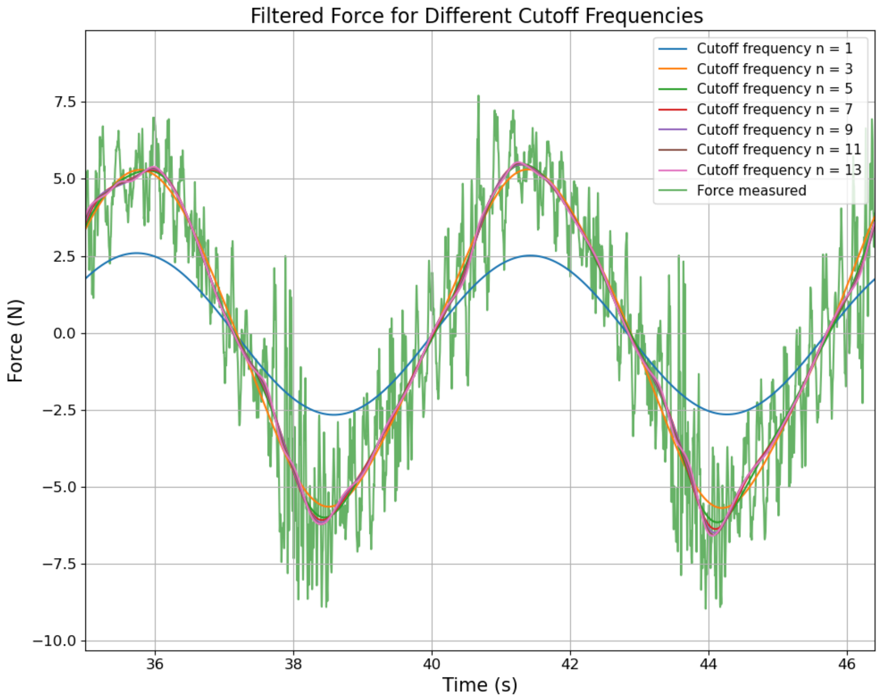

Figure 3.16: Measured force with ω = 1.10 rad/s for a single perforated model with small holes, A = 0.32 m and maximum oscillation velocity is 0.46 m/s.

The presence of multiple peaks and troughs at the upper and lower extremes of the force signal can be explained by the peaks and troughs in the high amplitude acceleration signal (Figure 3.17). Figure 3.18 provides the normalised acceleration and force of the same run as in Figure 3.17. It is observed that the small peaks and troughs are in the same phase and are related to each other.

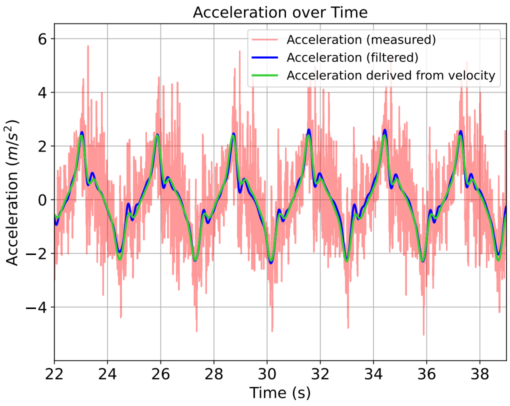

Figure 3.17: Measured and filtered acceleration and the acceleration derived from the velocity in time for A = 0.31 m and ω = 2.10 rad/s.

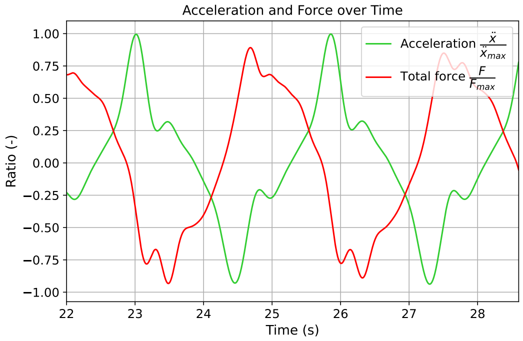

Figure 3.18: Normalised force and oscillation acceleration.

3.8.2. Data processing waves

First, the data of the measured wave elevation are discussed, which is used to determine the water particle velocities and accelerations. The wave sensor positioned in front of the model is labelled as sensor 1, and the wave height sensor, which is on the same lateral height as the model, is named wave height sensor 2. Figure 3.19 contains the raw measured wave elevation data for both sensors in the entire measurement duration with the models installed in the water. It takes some time when the waves are steady and stable. The most reproducible waves are expected in the interval between the first steady wave and when the wave reflected from the beach reaches the sensor. However, it is not exactly known when the first steady wave can be obtained because the graph shows that the elevation and shape of the waves are not exactly consistent in the time range. One possible explanation is that the wave maker does not generate the same wave in each cycle. This makes it challenging to reconstruct an identical theoretical wave equal to the measured wave. Ultimately, the velocities and accelerations are derived from a reconstructed theoretical wave that is as representative as possible of the measured wave elevation. It is essential for the postprocess to select a time window that begins with the arrival of the first well-formed wave and ends just before the reflected wave reaches the model again. Furthermore, the figure shows that the waves have wide troughs and steep crests. This indicates that shallow-water effects and higher-order waves are present. Therefore, first- and second-order wave elevations have to be compared with the measured data. Both first- and second-order wave theories are described in Appendix B.

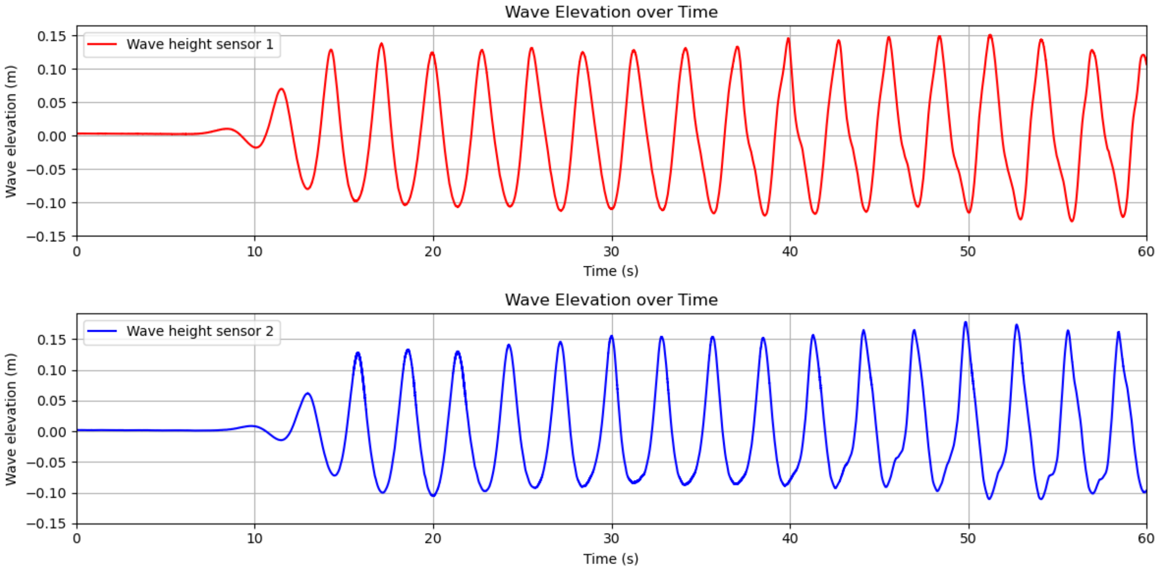

Figure 3.19: Measured wave elevations for the wave test with ω = 2.21 rad/s and A = 0.12 m with panels in series.

Figure 3.20 presents the same wave elevation measured as in Figure 3.19, alongside the theoretical first- and second-order wave elevations in time. Equation B.12 and Equation B.16 are used to plot first- and second-order wave elevations. First, this figure is used to evaluate which wave theory best matches the measured wave profiles. Second, it is used to assess the phase difference between the two sensors.

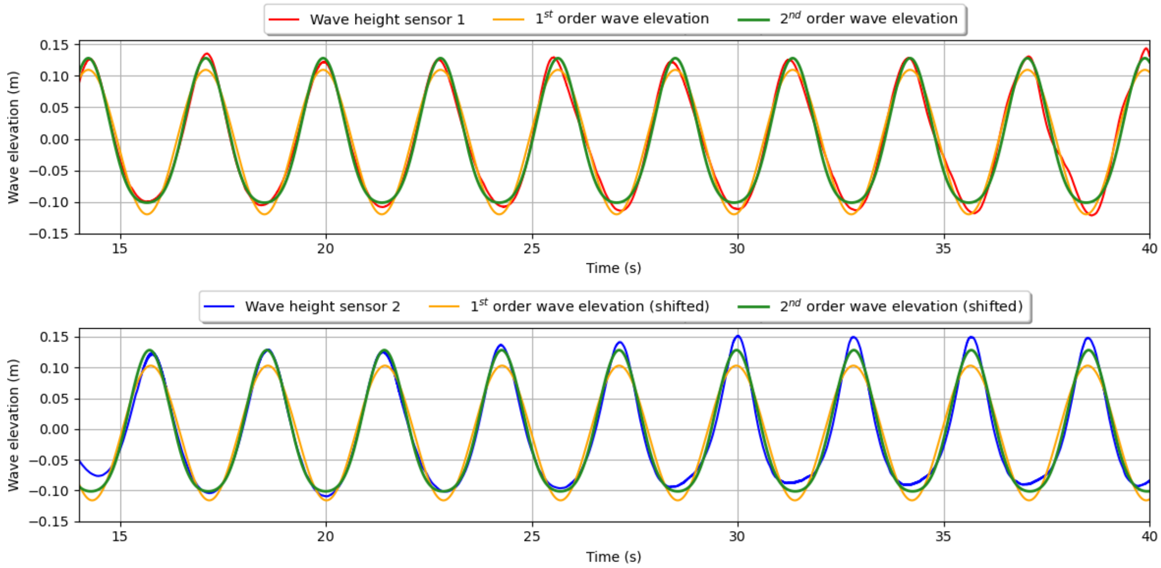

Figure 3.20: Comparison of measured, first-order and second-order wave elevation for wave test with ω = 2.21 rad/s and A = 0.12 m with panels in series.

Table 3.10 is used to find which wave theory order is more accurate compared to the undisturbed measured wave elevation. ω and A are the input parameters for the wave frequency and wave amplitude, respectively. The table lists the RMSE values for the first- and second-order wave profiles compared to the measured wave data. The theory of RMSE is described in Appendix B and the lower the RMSE value, the more accurate the prediction. Based on these results, it can be concluded that the second-order wave profile is a better representation of the measured data and that Equation B.18 and Equation B.20 are used to calculate the fluid particle velocity and acceleration, respectively. However, relatively high differences are observed for the lower frequency wave test. For this reason, the wave height signal of this test is shown in Figure 3.21. Wide troughs and steep crests become more significant in this figure. The measured wave profile closely resembles the characteristics of a cnoidal wave.

Table 3.10: Comparison of the first and second order wave elevation.

Panel amount	ω (rad/s)	A (m)	RMSE 1^{st} order (m)	RMSE 2^{nd} order (m)
3	2.21	0.12	0.013	0.011
1	2.21	0.12	0.013	0.012
1	2.21	0.09	0.009	0.007
1	1.47	0.09	0.020	0.012
1	2.21	0.05	0.004	0.003

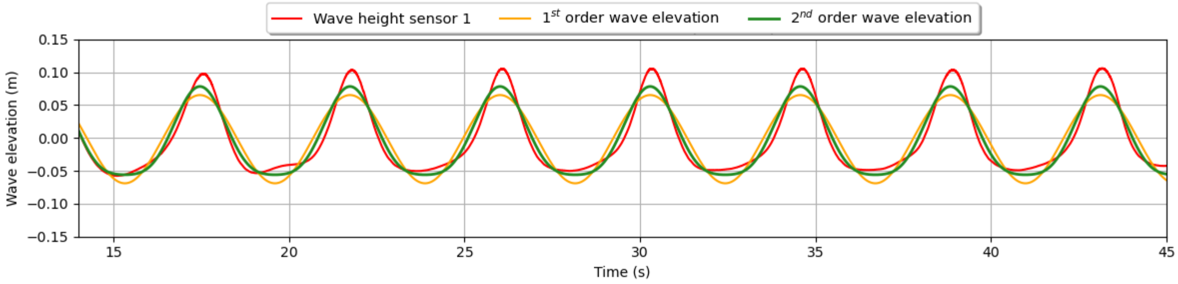

Figure 3.21: Measured wave elevation for the wave test with ω = 1.47 rad/s and A = 0.09 m.

The graph at the bottom of Figure 3.20 contains the shifted theoretical wave elevation using the phase difference between the two sensors. This phase difference is used to match the velocity and acceleration of the right fluid particle with the measured force. The resulting particle velocities and acceleration for both the first- and second-order wave profiles are provided in Figure 3.22 using the same phase as the shifted waves from the bottom graph of Figure 3.20. The load cell is placed at a water depth of 0.45 m, therefore, the velocities and accelerations are determined for this depth. Small differences in the amplitude values of the velocities and accelerations can be observed. This is due to the fact that second-order components decay more quickly with increasing depth, making first-order components more dominant [36].

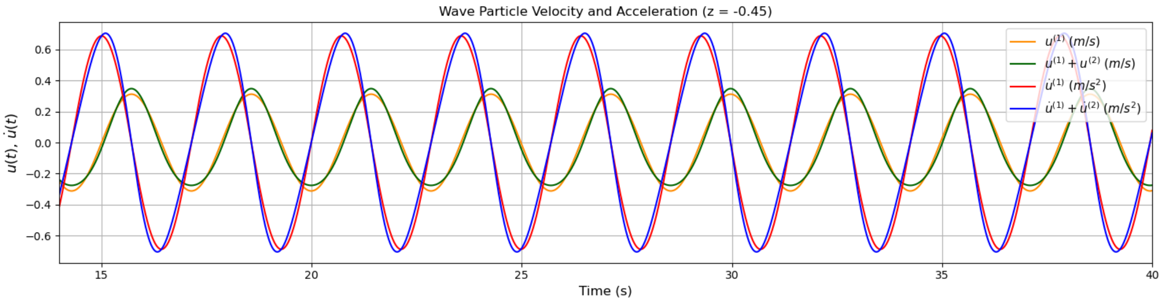

Figure 3.22: Comparison of the theoretical first- and second-order wave particle velocities and accelerations at a depth of 0.45 m.

The calculated velocities and accelerations of the fluid particles must be coupled with the measured forces to determine the values of the hydrodynamic coefficients. Figure 3.23 provides the raw measured force of both load cells and the total force resulting from the wave test of Figure 3.19. In contrast with the raw force signals of the forced oscillation test, the raw force signal of the wave test contains significantly less noise. Therefore, the raw measured force is used to determine the coefficient values. Moreover, both force signals are in phase, which allows them to be summed to get the total measured force.

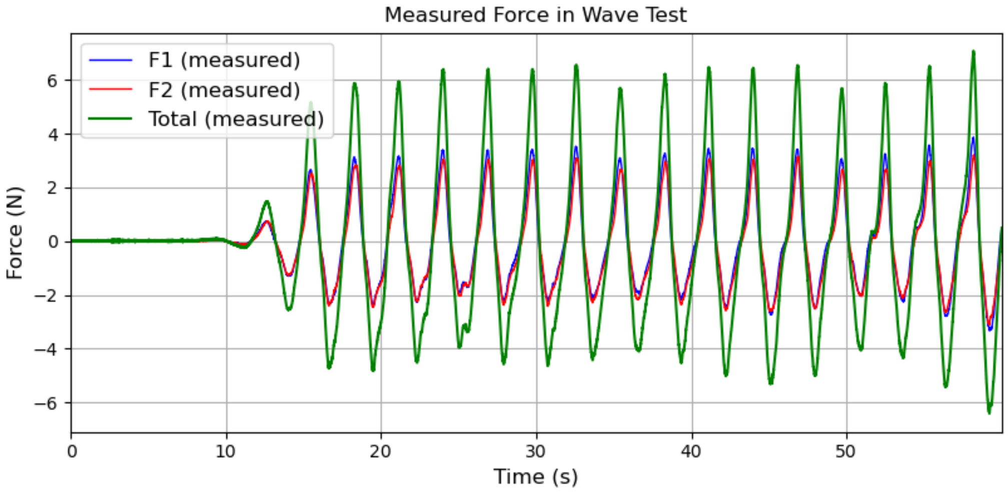

Figure 3.23: Measured force during the wave test with ω = 2.21 rad/s and A = 0.12 m with panels in series.

4

Determining the coefficients

This chapter outlines how the hydrodynamic coefficients are determined for both the forced oscillation tests and the wave tests by applying the hydrodynamic load equation given in Equation 1.15. This equation is reformulated in Equation 4.1.

$$F_{hyd}(t) = \underbrace{\rho V \dot{u}(t)}_{\text{FK}} + \underbrace{\rho V_r \mathbf{C_a}(\dot{u}(t) - \ddot{x}(t))}_{\text{Added mass}} + \underbrace{\frac{1}{2}\rho S \mathbf{C_d}(u(t) - \dot{x}(t))\,|(u(t) - \dot{x}(t))|}_{\text{Drag force}} + \underbrace{\rho V_r \omega \mathbf{C_b}(u(t) - \dot{x}(t))}_{\text{Linear damping}} \tag{4.1}$$

Forced oscillation tests are performed in still water, leading to $\dot{u}(t) = 0$ and $u(t) = 0$ and result in the hydrodynamic equation given in Equation 4.2.

$$F_{hyd}(t) = \underbrace{-\rho V_r \mathbf{C_a}\ddot{x}(t)}_{\text{Added mass}} - \underbrace{\frac{1}{2}\rho S \mathbf{C_d}\dot{x}(t)\,|\dot{x}(t)|}_{\text{Drag force}} - \underbrace{\rho V_r \omega \mathbf{C_b}\dot{x}(t)}_{\text{Linear damping}} \tag{4.2}$$

The model is fixed during the wave tests, which leads to $\ddot{x}(t) = 0$ and $\dot{x}(t) = 0$ and results in the hydrodynamic equation given in Equation 4.3.

$$F_{hyd}(t) = \underbrace{\rho V \dot{u}(t)}_{\text{FK}} + \underbrace{\rho V_r \mathbf{C_a}\dot{u}(t)}_{\text{Added mass}} + \underbrace{\frac{1}{2}\rho S \mathbf{C_d} u(t)\,|u(t)|}_{\text{Drag force}} + \underbrace{\rho V_r \omega \mathbf{C_b} u(t)}_{\text{Linear damping}} \tag{4.3}$$

S is taken as $W_m \times H_m$ for surge oscillations and $W_m \times L_m$ for heave oscillations. The dimensional added mass and linear damping are nondimensionalised by Equation 1.7 and Equation 1.8, respectively, where $V_r = \frac{\pi}{4}L_m^2 W_m$ for the heave oscillation test. This volume is based on the figure on the right in Figure 1.7 and corresponds analytically to the volume of a circular cylinder between the end plates. To provide insight into how this reference volume is defined, a schematic sketch is shown in Figure 4.1. The reference volume in the surge direction is defined as $V_r = L_m W_m H_m$.

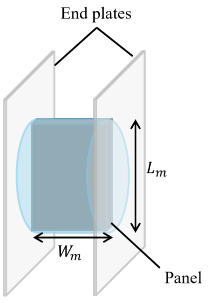

Figure 4.1: Schematic sketch of the reference volume in blue used in the heave forced oscillations.

First, the forced oscillation model will be described. Second, the wave test with a fixed structure will be handled. Both approaches employ the ordinary least squares method to obtain the hydrodynamic coefficients.

4.1. Forced oscillation

Equation 4.2 is used for the forced oscillation test, where a body is moving in still water. The load cells also measure the inertia force of the dry mass (M_{dry}) during the oscillation test. The dry mass is the total mass of the model, the two circular discs, the two small blocks, and half of the mass of the load cells. Consequently, Equation 4.4 is used to find the coefficients for the oscillation tests, where F_{LC} is the total measured force from the load cells.

$$F_{LC}(t) = -(M_{dry} + \rho V_r \mathbf{C_a})\ddot{x}(t) - \frac{1}{2}\rho S \mathbf{C_d}\dot{x}(t)|\dot{x}(t)| - \rho V_r \omega \mathbf{C_b}\dot{x}(t) \tag{4.4}$$

A substitution of Equation 4.4 in Equation B.3 results in the set of equations given in Equation 4.5. The coefficients can be found using Equation B.6.

$$\begin{bmatrix} -\rho V_r \ddot{x}(t_1) & -\frac{1}{2}\rho S \dot{x}(t_1)|\dot{x}(t_1)| & -\rho V_r \omega \dot{x}(t_1) \\ \vdots & \vdots & \vdots \\ \vdots & \vdots & \vdots \\ -\rho V_r \ddot{x}(t_n) & -\frac{1}{2}\rho S \dot{x}(t_n)|\dot{x}(t_n)| & -\rho V_r \omega \dot{x}(t_n) \end{bmatrix} \begin{bmatrix} \mathbf{C_a} \\ \mathbf{C_d} \\ \mathbf{C_b} \end{bmatrix} = \begin{bmatrix} F_{LC}(t_1) + M_{dry}\ddot{x}(t_1) \\ \vdots \\ \vdots \\ F_{LC}(t_n) + M_{dry}\ddot{x}(t_n) \end{bmatrix} \tag{4.5}$$

4.2. Wave tests

The hydrodynamic coefficients in the wave tests are determined using Equation 4.6. Note that V_m is the exact volume of the model. This results in the system of equations in Equation 4.7.

$$F_{LC}(t) = (\rho V_m + \rho V_r \mathbf{C_a})\dot{u}(t) + \frac{1}{2}\rho S \mathbf{C_d} u(t)|u(t)| + \rho V_r \omega \mathbf{C_b} u(t) \tag{4.6}$$

$$\begin{bmatrix} \rho V_r \dot{u}(t_1) & \frac{1}{2}\rho S u(t_1)\,|u(t_1)| & \rho V_r \omega u(t_1) \\ \vdots & \vdots & \vdots \\ \vdots & \vdots & \vdots \\ \rho V_r \dot{u}(t_n) & \frac{1}{2}\rho S u(t_n)\,|u(t_n)| & \rho V_r \omega u(t_n) \end{bmatrix} \begin{bmatrix} \mathbf{C_a} \\ \mathbf{C_d} \\ \mathbf{C_b} \end{bmatrix} = \begin{bmatrix} F_{LC}(t_1) - \rho V_m \dot{u}(t_1) \\ \vdots \\ \vdots \\ F_{LC}(t_n) - \rho V_m \dot{u}(t_n) \end{bmatrix} \tag{4.7}$$

The velocity and acceleration of the fluid particles are calculated with Equation B.18 and Equation B.20, respectively, for a water depth of 0.45 m where the load cells are positioned. Twelve force cycles are used for the wave frequency of 2.21 rad/s, and seven force cycles are used for the wave period of 1.47 rad/s. This is the time interval that starts when 3-4 built-up wave cycles are measured up to the time the reflected waves reach wave height sensor 2.

4.3. Multicollinearity problem

During post-processing, it is observed that there is a high correlation between the quadratic and linear velocity terms. The theory of correlation is described in Appendix B.2. The drag coefficient is related to the quadratic velocity, and the linear damping coefficient to the linear velocity. Due to the high correlation, there is a large standard error in the resulting value for the hydrodynamic coefficient of the least squares regression method. This is known as multicollinearity, which can result in unstable and incorrect values for the drag and damping coefficient in the least squares method [51]. The correlation between the quadratic velocity and the linear velocity is 0.98, which causes multicollinearity. According to M.P. Allen, the most appropriate solution to this problem is to remove one variable [51]. Therefore, in the present study, two models will be used, which separate the quadratic drag coefficient and the linear damping coefficient. An overview of these models is provided in Table 4.1. Both models will be compared to assess which model offers the most accurate hydrodynamic load estimation.

Table 4.1: Overview of two models used to determine the drag and damping coefficients separately.

	Added mass and quadratic drag	**Added mass and linear damping**
Forced oscillation test	$F(t) = -\rho V_r \mathbf{C_a} \ddot{x}(t) - \frac{1}{2}\rho \mathbf{C_d} S \dot{x}(t)\lvert\dot{x}(t)\rvert$	$F(t) = -\rho V_r \mathbf{C_a} \ddot{x}(t) - \rho V_r \omega \mathbf{C_b} \dot{x}(t)$
Wave tests	$F(t) = (\rho V_m + \rho V_r \mathbf{C_a})\dot{u}(t) + \frac{1}{2}\rho \mathbf{C_d} S u(t)\lvert u(t)\rvert$	$F(t) = (\rho V_m + \rho V_r \mathbf{C_a})\dot{u}(t) + \rho V_r \omega \mathbf{C_b} u(t)$

4.4. Predicted forces from the regression method

This section presents examples of the measured force signals used to determine the coefficients and the resulting fitted force curves obtained by the regression method for various test configurations. First, it is described how the accuracy of the ordinary least squares fits compared to the experimental data results is assessed. The following section presents an accuracy analysis of both models and a comparison between them.

The accuracy of the OLS method is evaluated using the coefficient of determination (R^2), the root mean squared error ($RMSE$) and its normalised form ($NRMSE$), which are described in Appendix B.3. The full range of measured data is used to normalise $RMSE$. The regression model is more accurate for R^2 values near 1.0 and $RMSE$ and $NRMSE$ values near zero. The resulting values of the hydrodynamic coefficients for the experimental tests and the corresponding R^2, $RMSE$ and $NRMSE$ of both fitted models are given in Appendix D.

Figure 4.2 contains two examples of the measured force signal and the fitted forces of the forced oscillation tests with the BH model. The difference in the two predicted force curves arises from the use of a quadratic velocity term in the drag model and a linear velocity in the linear damping model. It can be observed that the discrepancies between the fitted curves and the measured curves are higher in the right figure, especially in the upper and lower peaks. This is related to the previously mentioned small peaks and troughs on both the positive and negative slope sides of the acceleration signal. These small peaks and troughs become more significant as the oscillation acceleration increases, which leads to a decrease in the accuracy of the predicted signals.

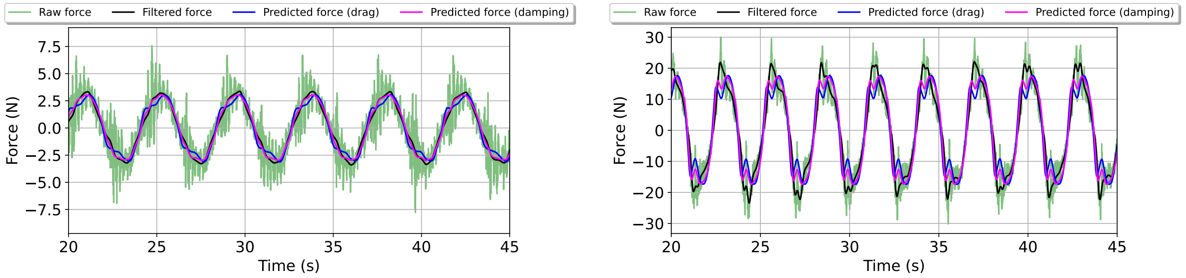

(a) Forced oscillation with ω = 1.47 rad/s and A = 0.16 m.

(b) Forced oscillation with ω = 2.21 rad/s and A = 0.32 m.

Figure 4.2: Raw force, filtered force and the predicted forces of the quadratic drag model and linear damping model of two different forced oscillation tests on model BH.

Figure 4.3 shows an example of the measured force and the fitted force of a surge forced oscillation test. The measured forces in this direction are lower than those observed in the heave oscillation tests as a result of the smaller normal surface area in the direction of oscillation. As a result, the difference in force values in Newtons in the peaks is also lower compared to the heave oscillations, leading to higher accuracy.

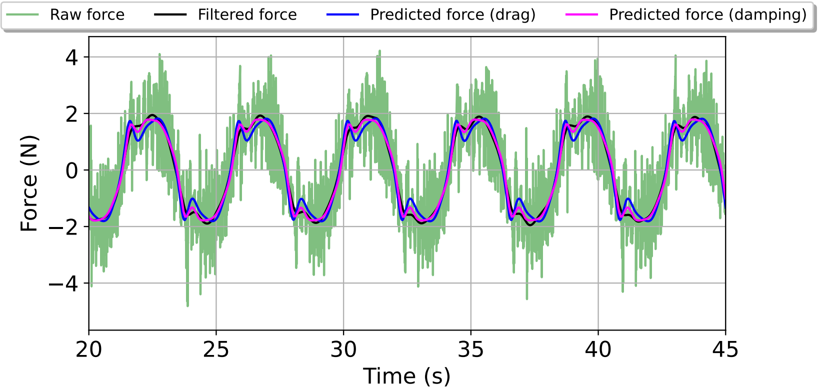

Figure 4.3: Raw force, filtered force and the predicted forces of the quadratic drag model and linear damping model of the surge forced oscillation test with ω = 1.47 rad/s and A = 0.44 m.

Figure 4.4 shows an example of the measured forces of ten wave periods and the corresponding predicted forces. Discrepancies can be observed in the extreme values of the signal. This is a consequence of the fact that the reconstructed wave, from which velocities and accelerations are derived, is not exactly identical to the actually measured wave.

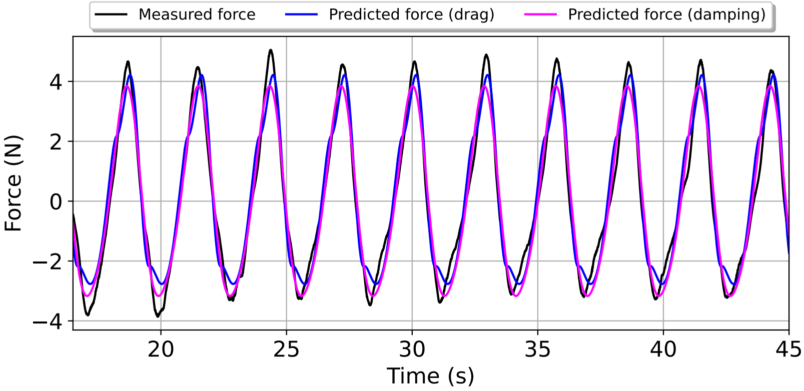

Figure 4.4: Measured force, and predicted forces of the quadratic drag model and linear damping model of the wave test using a single panel with ω = 2.21 rad/s and A = 0.09 m.

4.5. Comparing the force models

Two hydrodynamic models were previously introduced: one model includes the added mass and drag contributions, and the other model includes the added mass and linear damping. This section discusses which model is the most accurate representation compared to the measured data. An overview of the values of the hydrodynamic coefficients and the corresponding R^2, $RMSE$ and $NRMSE$ of both fitted models are given in Appendix D for every test configuration. All tests show higher R^2 and lower $RMSE$ values for the model using linear damping. An overview of the averaged values of R^2 and $NRMSE$ for the quadratic drag and linear damping model is provided in Table 4.2 for every type of test. SH is the model with the smaller hole size, and BH is the model with the larger hole size. Based on the values in this table, it can be concluded that the linear damping model is more accurate in predicting the hydrodynamic loads.

Table 4.2: Averaged values for R^2 and $NRMSE$ for both quadratic damping and linear damping models for each test.

Test type	**Model**	$\overline{R^2_{C_d}}$	$\overline{R^2_{C_b}}$	$\overline{NRMSE_{C_d}}$	$\overline{NRMSE_{C_b}}$
Forced oscillation - heave - 1 panel	SH	0.90	0.97	9.1%	5.4%
Forced oscillation - heave - 1 panel	BH	0.91	0.97	9.0%	5.2%
Forced oscillation - heave - 3 panels	SH	0.92	0.96	8.6%	5.8%
Forced oscillation - surge	SH	0.97	0.99	5.9%	2.6%
Wave tests	SH	0.93	0.95	7.4%	6.3%

Table 4.3 lists the minimum and maximum values for the coefficient of determination and the normalised root mean squared error of the linear damping model. The high R^2 and low $NRMSE$ values indicate that the linear damping force equation is accurate, except for the higher period wave test due to the less accurate wave elevation predictions in Figure 3.21. Moreover, it has been observed that less accurate values are related to the tests in which high values of force amplitudes were measured.

Table 4.3: Overview of minimum and maximum values of $R^2_{C_b}$ and NRMSE$_{C_b}$.

Test type	**Model**	$R^2_{C_b}$	**NRMSE**$_{C_b}$ %
Forced oscillation – heave – 1 panel	SH	[0.92, 0.98]	[3.6, 7.5]
Forced oscillation – heave – 1 panel	BH	[0.93, 0.98]	[3.7, 8.1]
Forced oscillation – heave – 3 panels	SH	[0.94, 0.98]	[4.3, 7.5]
Forced oscillation - surge	SH	[0.99, 1.0]	[2.1, 3.1]
Wave tests	SH	[0.88, 0.98]	[4.3, 9.2]

Figure 4.5 contains all measured force amplitudes for model SH and model BH of the forced oscillation tests with their corresponding $NRMSE$ values. This figure indicates that the predicted forces from the regression method are less accurate for the oscillation tests that result in high force amplitudes. Higher force amplitudes are related to higher oscillation velocities and accelerations. To provide an indication of the less accurate predictions, Figure 4.6 is shown. This is the same oscillation test as in Figure 4.2b and is related to the rightmost point in Figure 4.5. The figure shows the raw measured force, the filtered force and the predicted forces from both the quadratic drag and linear damping models over time. The predicted forces tend to be less accurate in the regions where the acceleration signal displays small peaks and troughs near the extreme values. As mentioned above, these peaks and troughs are more significant at higher oscillation acceleration values, leading to less accurate force predictions in this region.

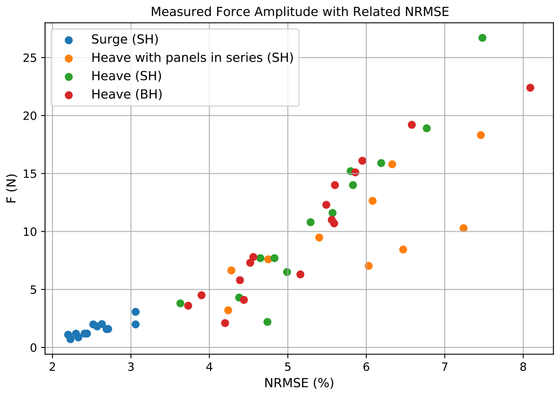

Figure 4.5: Measured force amplitudes versus the corresponding $NRMSE$ from the forced oscillation tests.

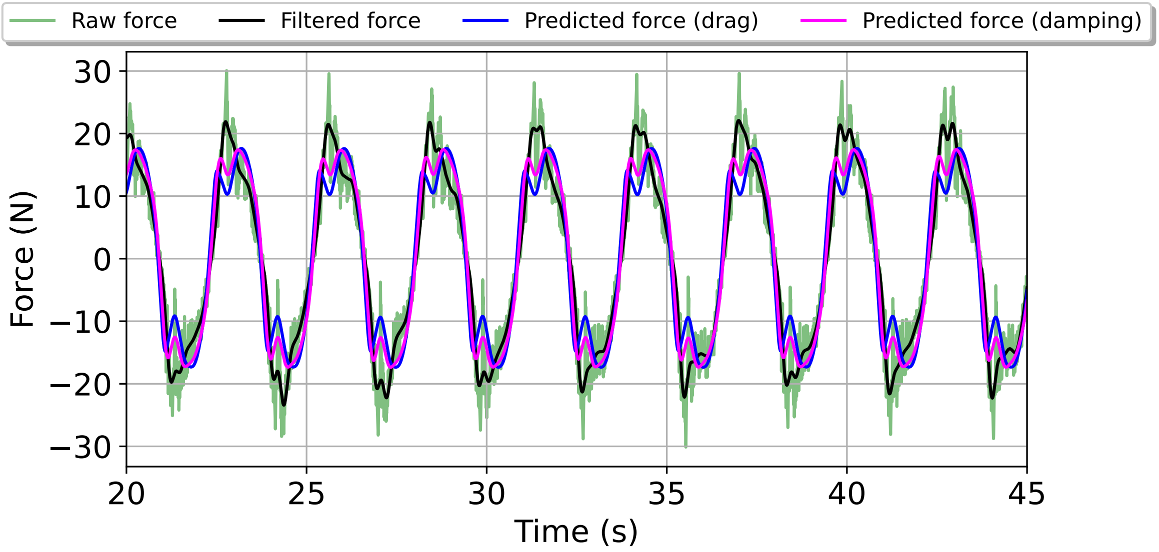

Figure 4.6: Measured and predicted forces from the quadratic drag model and the linear damping model for the forced oscillation test with T = 2.85 s and A = 0.31 m using a single BH panel.

Consequently, the force equation including the added mass and linear damping is more accurate than the force equation including the quadratic drag to estimate the hydrodynamic loads on the perforated panels. The resulting boundary values of R^2 and $NRMSE$ from the experiments indicate that the linear damping model is accurate. The predicted forces from the least squares method tend to be less accurate in the extreme value regions for higher force amplitudes. This is caused by the small peaks and troughs near the extremes of the acceleration, which are more significant for oscillations with high accelerations.

Although the model including the quadratic drag force is less accurate, the drag coefficients will still be determined in the results for the following reasons:

1. It is useful to determine the drag coefficient because this coefficient can be used in software for hydrodynamic analysis.
2. The trend of the drag coefficient can be compared with the results in the literature.
3. The objective remains to investigate the effects of the interaction on the values of C_d.
4. The results of the quadratic drag term provide insight into the dominance of form drag for different test conditions.

5

Results

The objective of this study is to determine the hydrodynamic coefficients in the form of added mass, quadratic drag, and linear damping. In this study, both forced oscillation tests in still water and fixed structure wave tests are conducted. First, the results of the forced oscillation tests will be described. Secondly, the results of the wave tests are described and compared with those of the oscillation tests. The results concerning the AdBm model will be available two years after publication (October 16, 2027) and can be requested from Dr.-Ing. S. Schreier and Dr. Ir. H.J. de Koning Gans.

In this chapter, the values of C_a, C_d and C_b are plotted as a function of KC. Table D.1 provides an overview of the KC values for the first 20 metres and the range of periods for a wave height of 2.5 m. This table can be used to connect the resulting hydrodynamic coefficient value with the depth of the panel and the wave period.

5.1. Results of the forced oscillation test

Table 5.1 lists an overview of the scaled frequencies and periods and the corresponding symbols used in the figures in this section. The lowest period value is related to the wave period of 4.5 seconds, and the highest period value is related to the wave period of 9.0 seconds. The Keulegan-Carpenter numbers are calculated using Equation 1.4.

Table 5.1: Frequency, periods and the symbols used in the figures for the forced oscillation results.

Frequency (rad/s)	Period (s)	Symbol
2.21	2.85	•
1.47	4.27	+
1.10	5.69	★

5.1.1. Results of the forced oscillation tests using a single vertically oriented panel

This subsection contains the results of the test configuration shown in Figure 3.4b.

Results for the panel with smaller hole size (model SH)

Figure 5.1a presents the values of the added mass and drag coefficients plotted against the corresponding KC number for the oscillation test with a single perforated panel with a smaller hole size. In addition, the figure includes curve fits for both C_a and C_d. The drag coefficient is estimated in the form of

$$C_d = d_1 \cdot KC^{d_2}. \tag{5.1}$$

Equation 5.1 is based on the analytical equation for the drag coefficient, which is given in Equation 1.9. For the added mass, a linear curve fit estimation is used in the form of

$$C_a = a_1 \cdot KC + a_2. \tag{5.2}$$

It can be seen that C_d decreases with increasing KC number, while the value of the added mass increases linearly as a function of KC. Low oscillation amplitudes correspond to low KC values, while higher amplitudes lead to higher KC values. The highest KC values are associated with panels positioned near the water surface, while the lower KC values are related to the deeper arranged panels. Only minimal differences are observed between the measured drag coefficients and the fitted purple line, which is supported by the high value of the coefficient of determination for the fitted drag curve in Table 5.2. This table lists the values of the parameters for the fitted hydrodynamic coefficient lines with their R^2 values. It can be seen that the value of d_2 is identical to the theoretical value of $-\frac{1}{3}$ in Equation 1.9. In contrast, there are some differences in the values for the added mass for different frequencies. Lower frequencies tend to result in slightly higher values of the added mass coefficient, which is consistent with the finding of Tao and Dray [28]. Nevertheless, these differences are minor, and due to the high R^2 value of the added mass fit across the entire range of data, the fitted curve is used for subsequent graphs.

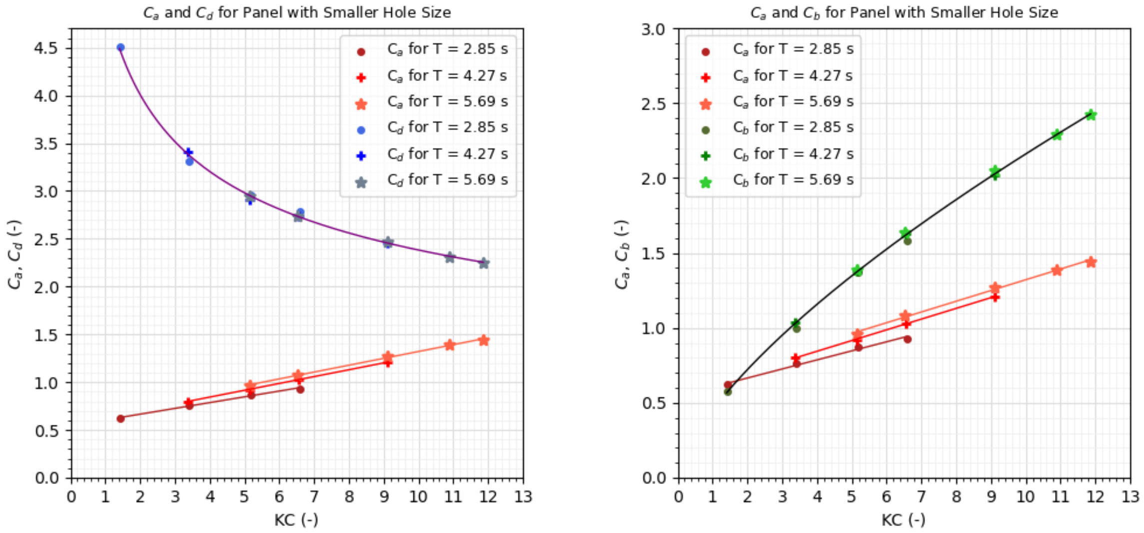

(a) Added mass and drag coefficients for a single perforated panel with smaller hole size.

(b) Added mass and damping coefficients for a single perforated panel with smaller hole size.

Figure 5.1: Results of model SH of forced oscillation tests using a single panel.

Figure 5.1b contains the added mass and linear damping coefficients of the linear damping model plotted as a function of KC. Linear damping coefficients are estimated with Equation 5.3. The added mass coefficients are identical to those in Figure 5.1a. Similarly with the drag coefficient, the values of the damping coefficient are independent of the oscillation frequency, and the values can be estimated from Equation 5.3 with the corresponding fit parameters provided in Table 5.2. The value of b_1 corresponds to the theoretical value of $\frac{2}{3}$ in Equation 1.10, which means that the trend of the damping coefficient is in line with the literature.

$$C_b = \frac{b_1}{\pi^2} \cdot KC^{b_2} \tag{5.3}$$

Table 5.2: Fitted parameters for added mass (C_a), drag (C_d), and linear damping (C_b).

Added mass (C_a)

	a_1	a_2	R^2
C_a (T = 2.85s)	0.060	0.54	0.991
C_a (T = 4.27s)	0.072	0.56	0.9995
C_a (T = 5.69s)	0.072	0.60	0.996
All C_a values	0.078	0.50	0.972

Drag (C_d) and damping (C_b)

			R^2
Fit for C_d values	d_1 = 5.02	d_2 = -0.32	0.997
Fit for C_b values	b_1 = 4.44	b_2 = 0.68	0.998

Results for the panel with bigger hole size (model BH)

Figure 5.2a contains the added mass and drag coefficients as functions of KC for the oscillations with the panel with a bigger hole size across different periods. The trends for both coefficients are consistent with those found for the panel with a smaller hole size: the drag coefficient decreases and the added mass increases for higher values of KC. Moreover, the added mass coefficients for lower frequencies seem to be slightly higher. Equation 5.1 is used to estimate the drag coefficient values as a function of KC with the values of d_1 and d_2 provided in Table 5.3. This model predicts the drag coefficients well. The added mass and linear damping coefficient values for the panel with a bigger hole size are shown in Figure 5.2b. Equation 5.3 is used to estimate the values of the damping coefficients, which is a reliable approximation due to the high $R^2_{C_b}$ value provided in Table 5.3.

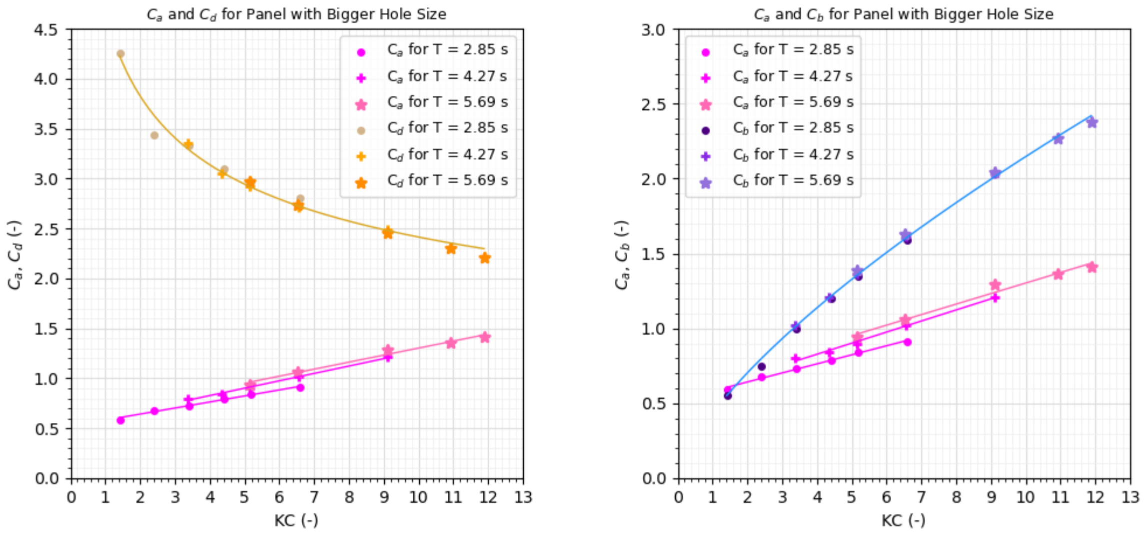

(a) Added mass and drag coefficients for a single perforated panel with bigger hole size.

(b) Added mass and damping coefficients for a single perforated panel with bigger hole size.

Figure 5.2: Results of model BH of forced oscillation tests using a single panel.

Comparing the results

Table 5.3 includes the values of the parameters for the fitted curves for C_a, C_d and C_b for model SH and model BH. The fitted curves of the models with round holes, which are given above the table, are compared in Figures 5.3a and 5.3b. In the figure on the left, C_a and C_d are plotted as functions of KC for both models, while on the right C_a and C_b are plotted as functions of KC for both models. The comparison indicates that the differences between the two models are minimal, resulting in the round hole size not influencing the hydrodynamics as long as the perforation ratio is the same. This is in line with the results in the literature, described in Section 1.6 [25][30]. Only the drag coefficient values for a KC $\leq$ 5 seem to be slightly lower for the panel with a larger hole size.

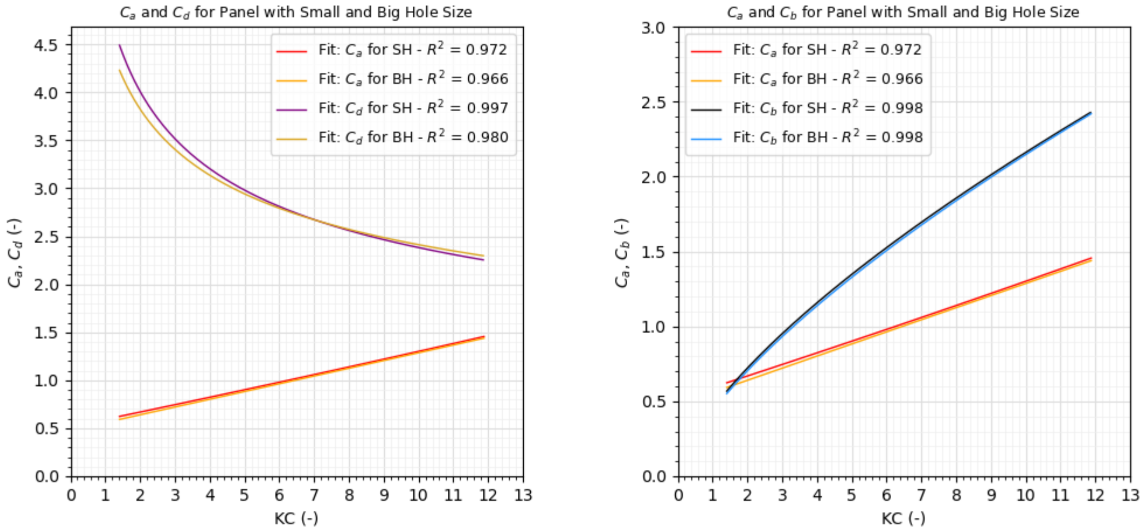

(a) Curve fits for added mass and drag coefficients for panel with smaller hole size (SH) and bigger hole size (BH).

(b) Curve fits for added mass and damping coefficients for panel with smaller hole size (SH) and bigger hole size (BH).

Figure 5.3: Comparison of the results of the forced oscillation tests using a single panel between the model SH and model BH.

$$C_a = a_1 \cdot KC + a_2, \qquad C_d = d_1 \cdot KC^{d_2}, \qquad C_b = \frac{b_1}{\pi^2} \cdot KC^{b_2}.$$

Table 5.3: Parameters for the fitted curves for the perforated panels.

Panel type	a_1	a_2	$R^2_{C_a}$	d_1	d_2	$R^2_{C_d}$	b_1	b_2	$R^2_{C_b}$
Perforated plate (SH)	0.078	0.50	0.972	5.02	-0.32	0.997	4.44	0.68	0.998
Perforated plate (BH)	0.081	0.48	0.966	4.67	-0.29	0.980	4.29	0.69	0.998

5.1.2. Results of the panels in series

It is essential to study the effect of panels placed in series on the value of the hydrodynamic coefficients to assess the interaction effects between the vertically arranged panels in practical applications. The values of the hydrodynamic coefficients of model SH are shown in Figure 5.4. In addition, both graphs include the fitted data curves from the oscillation test with a single panel for comparison. The added mass values for the series panels start to differ in comparison with the value used for a single panel for KC $\geq$ 6.5, which is related to oscillation amplitudes greater than 0.30 m. An explanation is that, due to the presence of the outer panels, the amount of volume of water that accelerates increases for oscillation amplitudes higher than 0.3 metres, whereas this additional mass can escape using one panel in the oscillation. The distance between the panels is 0.40 m, which leads to the fact that the ratio between the oscillation amplitude and the distance between the models has to be greater than $\frac{3}{4}$ to obtain interaction effects on the added mass. The added mass values start to lose the linear relation in this range, as a result, the added mass is estimated with a quadratic polynomial.

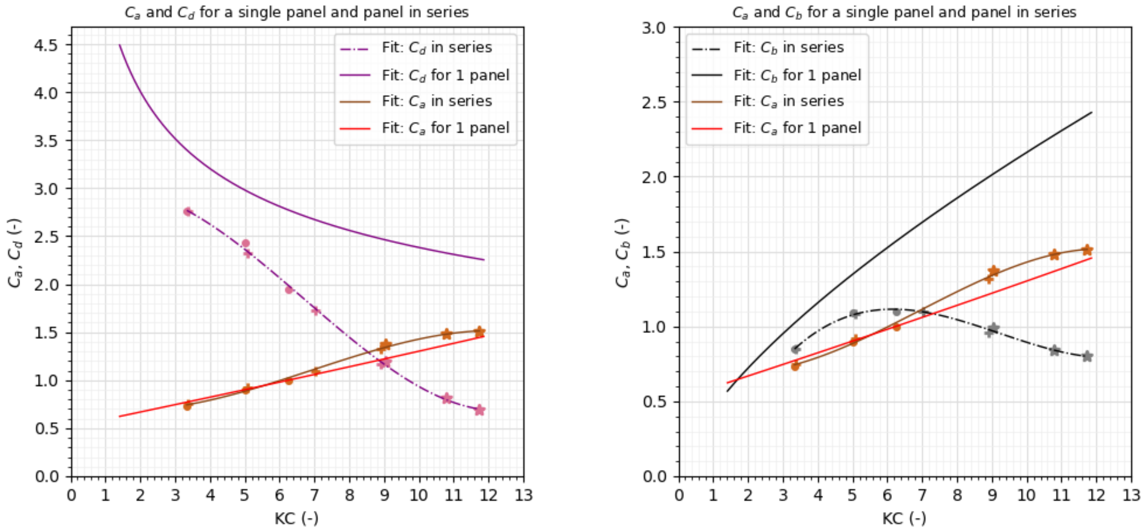

(a) Added mass and drag coefficients for panels in series.

(b) Added mass and damping coefficients for a panel in series.

Figure 5.4: Results of model SH for panels in series.

A significant difference is observed in the values of the C_d and C_b coefficients when comparing the oscillation with one panel and a series of panels. Equations 5.1 and 5.3 are no longer applicable to estimate drag and damping coefficients as a function of KC. Furthermore, the differences increase as the oscillation amplitude increases. This is consistent with the earlier mentioned findings of Tao et al. (2007) in the introduction, who conclude that the differences are caused by the vortex shedding interaction between the panels. This interaction is stronger with increasing KC. To better understand the variation in the drag and the damping coefficients, Figure 5.5 is used. This figure introduces the correction factor α_c, applied to both the drag and the damping for panels arranged in series. This correction factor is relevant to assess the interaction effects as a function of KC on the drag and damping coefficients. This factor is the ratio between the fitted lines for drag and damping estimation using a single panel and the fitted lines for drag and damping using three panels. Both lines follow the same trends, and the maximum difference between the correction lines is only 0.03. This small deviation can be attributed to the fact that the correction lines are based on fitted data, which contain uncertainties compared to the directly measured experimental values. The drag and damping coefficients for a series of panels can then be determined with Equation 5.4 and Equation 5.5, respectively. It is important to note that Figure 5.5 is only valid for KC values between 3.4 and 11.8. It is expected that the correction value tends to reach a value of one for KC values approaching zero, as the middle panel is no longer influenced by the wake field of the outer panels at low oscillation amplitudes. However, a slight increase in the correction factor is observed near the KC values below 4.0. This is an interesting value because this value is related to an oscillation amplitude of 0.2 m, which is exactly half the distance between the panels. Testing lower oscillation amplitudes will gain more insight into the values for C_d and C_b for KC $\leq$ 3.5, however, these were not conducted in this study because interaction effects were expected to be very minimal according to the literature.

$$C_{d,series} = \alpha_c \cdot C_{d,single} \tag{5.4}$$

$$C_{b,series} = \alpha_c \cdot C_{b,single} \tag{5.5}$$

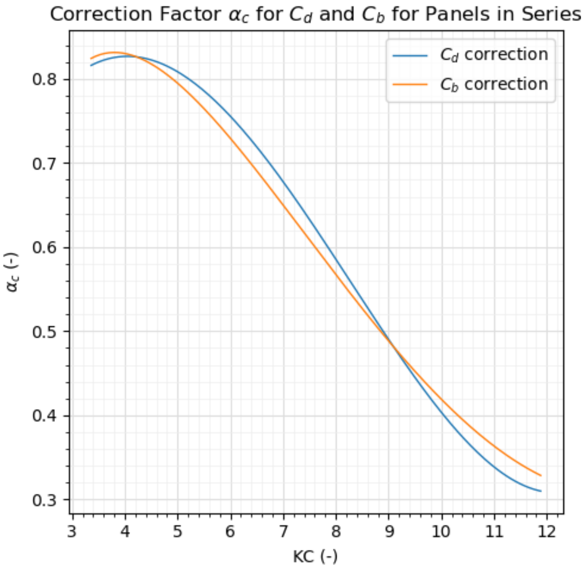

Figure 5.5: Correction factor as a function of KC on the drag and damping coefficients for panels in series (model SH).

5.1.3. Results of surge oscillation tests

This section describes the results of the oscillation tests for horizontally oriented panel oscillations. The values of the hydrodynamic coefficients as a function of KC are shown in Figure 5.6 for model SH. The drag coefficient follows the trend described by Equation 5.1 and approaches an asymptotic value of C_d = 1.8. This aligns with the steady flow drag coefficient for an H-frame, reported in DNV-RP-H103 between 1.6 and 2.1 [19]. This indicates that the panel between the frames has negligible effects on the drag coefficient for surge oscillations. Similarly, the added mass coefficient approaches an asymptotic value for the oscillation amplitudes tested. For this reason, the added mass coefficient is estimated with a quadratic polynomial in the form described in Equation 5.6.

$$C_a = a_1 KC^2 + a_2 KC + a_3 \tag{5.6}$$

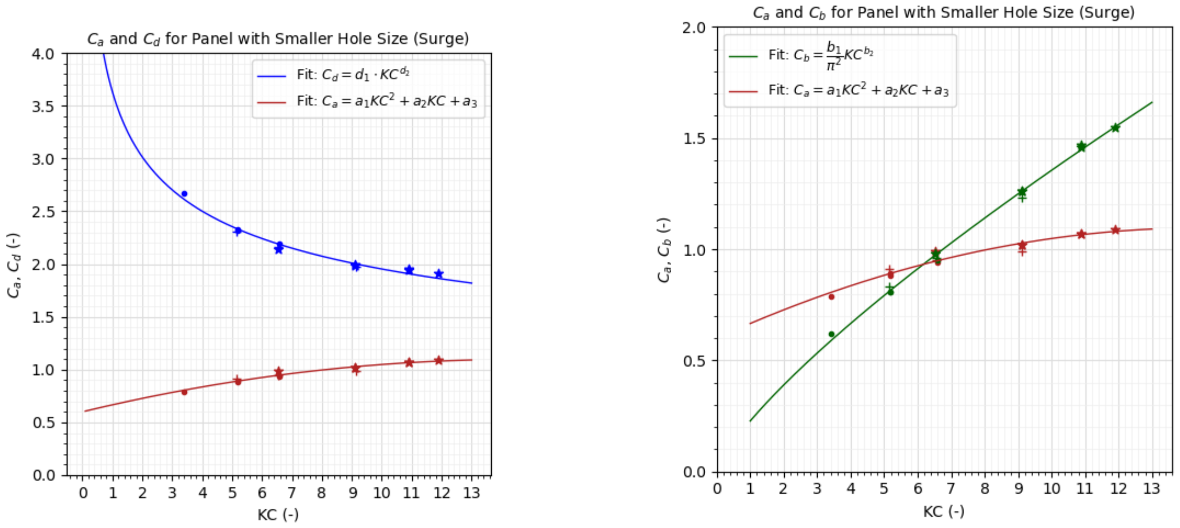

(a) Added mass and drag coefficients for forced oscillation tests in surge direction.

(b) Added mass and damping coefficients for forced oscillation tests in surge direction.

Figure 5.6: Surge oscillation results of model SH.

The linear damping coefficients in the surge oscillation direction are provided in Figure 5.6b, together with the estimated fit of Equation 5.3. This equation is an excellent fit for the measured linear damping coefficients using the fit coefficients from Table 5.4. Moreover, this table also lists the fit parameters for the added mass and the drag coefficients and their coefficients of determination. These values can be substituted in the estimation equations to find the value of the hydrodynamic coefficient as a function of KC within this range of oscillation amplitudes and frequencies.

Table 5.4: Parameters for the fitted curves for the surge oscillation tests.

Panel type	a_1	a_2	a_3	$R^2_{C_a}$	d_1	d_2	$R^2_{C_d}$	b_1	b_2	$R^2_{C_b}$
Perforated model (SH)	-0.0024	0.0683	0.600	0.952	3.635	-0.270	0.976	2.246	0.774	0.996

5.2. Results fixed structure wave tests

This section contains the results of the wave tests with a fixed structure for the model with a smaller hole size. The KC number is determined with Equation 1.3, using the maximum particle wave velocities from Stokes' second-order wave theory.

The resulting values of C_a, C_d and C_b of the model with the smaller hole size for the wave tests are provided in Figure 5.7 and compared with the fitted curves of the heave oscillation tests. As in the oscillation tests, the quadratic drag coefficient decreases with increasing KC, while the added mass increases. However, small deviations are observed between the results of the oscillation and wave tests, particularly at higher KC values. The figures also include the values for C_a, C_d and C_b for the wave period of 4.27 seconds, which are higher than for the lower wave period. This is in contrast with the oscillation results, where the frequency had little to no influence on the coefficients. These differences are in line with the study of F. Mentzoni, whose findings are described in Section 1.6. Consequently, a possible reason for the differences can be attributed to the vertical velocity component in the motion of the orbital fluid, which is not present in the oscillation test. Oscillating the model in still water will form symmetric vortices at the edges and in the holes, whereas in orbital wave fluid motion, this symmetry breaks, leading to lower pressures and lower values of hydrodynamic coefficients [21]. However, this study does not contain any numerical simulations that can confirm this conclusion.

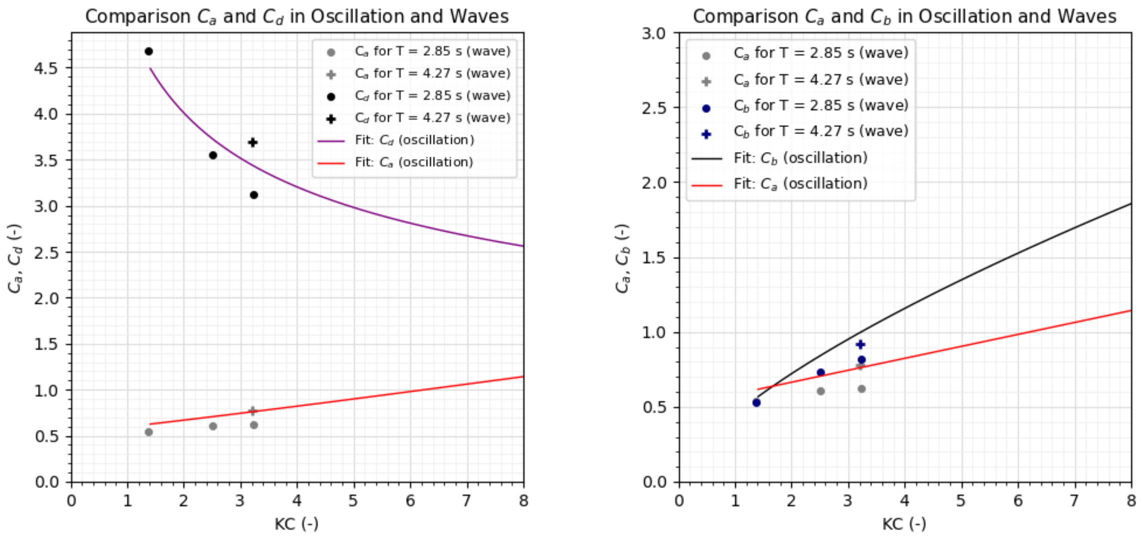

(a) Comparison of the added mass and drag coefficients for oscillation and waves.

(b) Comparison of the added mass and damping coefficients for oscillation and waves.

Figure 5.7: Results of the wave tests compared with the forced oscillation tests for model SH.

The test using three panels in series resulted in the same added mass coefficients but different values for the drag and damping coefficients. The values of the drag and damping coefficients for KC = 3.2 using three panels in series are 2.5 and 0.68 for the model SH, respectively. Using Equations 5.4 and 5.5, the value of the correction factor for C_d is 0.81 and 0.83 for C_b for the wave test. These values correspond to the correction factor for the forced oscillation tests for KC = 3.2 in Figure 5.5.

5.2.1. Comparison with F. Mentzoni

The results of the forced oscillation tests and the wave tests are discussed and compared with those in the study of F. Mentzoni to find similarities with the literature. Figure 5.8a contains normalised force results in this study, with the oscillation test results shown in blue and the wave test results shown in red. The force is normalised with $\sqrt{C_a^2 + C_b^2}$. The resulting normalised forces from the study of F. Mentzoni are shown in Figure 5.8b. The figure shows that the frequency has little to no effect on the normalised force in the oscillation tests. In contrast, for the wave test, the normalised force is influenced by the wave period. The same results are obtained in this study. As in the study of Mentzoni, the normalised force is higher for higher wave periods, and the difference in the normalised force between oscillations and waves increases for increasing KC. The red dotted line represents an estimated curve of how the normalised force may propagate as a function of KC to provide a comparison of the values of the normalised oscillation and wave force for higher KC values. However, this estimation is not validated and is only used as an indication.

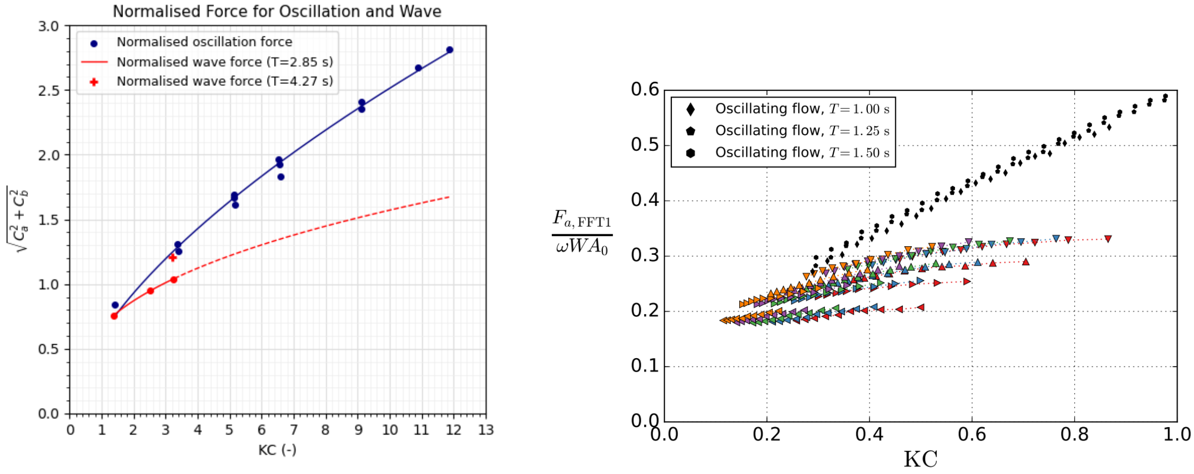

(a) Normalised force for heave oscillation tests compared with normalised force in wave tests for the panel with smaller hole size.

(b) Experimental normalised force for oscillation tests and incident wave tests from F. Mentzoni [21].

Figure 5.8: Normalised forces from forced oscillation test and wave tests compared to the results of F. Mentzoni.

In conclusion, the oscillation tests overestimate the values for the hydrodynamic coefficients, especially in the higher KC regimes. The frequency of the wave influences the values of the hydrodynamic coefficients. Longer wave periods result in higher values of the hydrodynamic coefficient for the same KC value. However, it is not known what the differences are for KC $\geq$ 3.2. Therefore, additional wave tests should be conducted in a facility with broader testing capabilities.

5.2.2. Discussion on the results of the wave tests

Forced oscillations were performed with a wider range of KC values, and the results were compared with those of the wave tests. Comparisons indicate that the forced oscillation test overestimates the values of the hydrodynamic coefficients, and the differences become more significant at higher KC values. This observation is consistent with the study of F. Mentzoni. Furthermore, the orbital shape of the particle trajectories is significantly more elliptical than the orbital shapes depicted in Figure 2.2, caused by the limited depth of the water. This leads to a difference in the orientation of the particle fluid velocity and acceleration vectors, which potentially leads to different values for C_a, C_d and C_b. Consequently, additional wave tests should be conducted in a facility with broader testing capabilities.

6

Conclusion

This study aimed to determine the hydrodynamic loads acting on noise mitigation panels used to reduce sound during monopile piling. Knowing the values of the hydrodynamic coefficients under environmental wave conditions enables estimating the hydrodynamic loads. The hydrodynamic coefficients are found for an NMS panel and two perforated panels, whose geometry is based on the NMS panels, by conducting experimental model tests. The main research question and subquestions were defined as follows:

Research question

- What are the values of the hydrodynamic coefficients in the heave and surge directions in the form of added mass, drag, and linear damping for the perforated panels in realistic wave conditions?

Research subquestions

- What are the values of the hydrodynamic coefficients in forced oscillation tests and fixed structure wave tests, and how can they be compared?
- What is the effect of multiple panels arranged in series on the hydrodynamic coefficients?

Both forced oscillation tests in still water and wave tests with a fixed model were conducted to answer the research questions. The test parameters were based on environmental wave conditions. The nondimensional Keulegan-Carpenter number (KC) is the most dominant factor in the values of the hydrodynamic coefficients. Therefore, the added mass coefficient (C_a), drag coefficient (C_d) and linear damping coefficient (C_b) are determined as a function of KC for $1.4 \leq \text{KC} \leq 11.9$. Due to multicollinearity, two load models are used: one model consisting of added mass and quadratic drag and the other model with added mass and linear damping. The force equation, including added mass and linear damping terms, is most accurate for predicting hydrodynamic loads based on accuracy analysis.

The results of the heave forced oscillation test show that the added mass increases linearly with increasing KC, while the drag coefficient decreases exponentially, and the linear damping increases exponentially. These trends are consistent with the literature, and the curves for the drag and linear damping coefficient are in line with the expected theoretical relation. Furthermore, the drag and linear damping were found to be frequency independent, whereas the added mass was slightly higher for lower oscillation frequencies. This confirms that the KC number is the most dominant nondimensional number compared to Reynolds.

The curves of the hydrodynamic coefficients in the surge directions show trends similar to the results of the heave oscillation tests. However, the added mass coefficient approached an asymptotic value within the investigated KC range. The total damping force is primarily determined by the outer frames in the surge direction.

Due to experimental limitations in wave amplitude, the maximum KC value of 3.2 was reached for the wave tests, which was expected to be 5.4. This results in a lower comparison range with the forced oscillation test. Added mass, drag, and damping coefficients in the wave test are comparable with the oscillation test for low KC values. However, the values of the hydrodynamic coefficients are higher for oscillation tests compared to wave tests at higher KC values, leading to an overprediction of the total hydrodynamic load.

It is important to investigate the interaction effects because the panels are positioned vertically under each other in practice. When three panels were placed in series, the drag and damping coefficients were significantly reduced up to 70% compared to the configuration using a single panel. This reduction becomes more pronounced with higher KC values. In contrast, the added mass coefficient showed only a slight increase at higher KC values. The results show that the interaction effects reduce the total hydrodynamic loads on the NMS panels.

In conclusion, the hydrodynamic coefficients were successfully determined in this study. The coefficients are plotted as functions of KC, and the trends show similarities with the existing literature. It is recommended to use the force model including the added mass and linear damping terms due to higher accuracy. The findings contribute to a better understanding of the hydrodynamic behaviour of the panels in the NMS and provide a basis for defining design parameters for the deployment system.

7

Recommendations

The present study can be used to determine the hydrodynamic loads on perforated noise mitigation panels used during the installation of monopiles using the experimentally determined hydrodynamic coefficients. However, the study has some limitations that can be addressed in further research. Therefore, the following recommendations are listed:

- Additional wave tests should be conducted in a facility with broader testing capabilities to test a wider range of wave amplitudes and frequencies, resulting in a larger range of KC and Re values. This will provide a more complete comparison between the forced oscillation and wave results.
- Performing tests with a higher water level will reduce the higher-order wave components and ensure that the orbital wave particle orientations and trajectories are identical to those in linear environmental waves. Moreover, higher water depths allow testing with the panel positioned horizontally and at different submergences.
- In practice, the incoming waves approach from different directions. Therefore, it is recommended to perform experimental tests that measure hydrodynamic loads in additional degrees of freedom such as sway, roll, pitch, and yaw.
- Perform a numerical analysis to validate the resulting hydrodynamic coefficients of the experiments. In addition, numerical simulations will provide more insight into the flow separations and vortex sheddings around the models, which is especially relevant when investigating interaction effects. Furthermore, numerical results may clarify the observed differences in the coefficient values between the forced oscillation and wave test results.
- Apply the experimentally determined hydrodynamic coefficients in software models that can provide an accurate estimation of the hydrodynamic loads on the entire NMS system to set up design parameters and perform a safety analysis.

References

[1] A. Tsouvalas. “Underwater noise generated by offshore pile driving”. PhD thesis. TU Delft, Nov. 2015. URL: `https://resolver.tudelft.nl/uuid:55776f60-bbf4-443c-acb6-be1005559a98`.

[2] X. Sun, D. Huang, and G. Wu. “The current state of offshore wind energy technology development”. In: *Energy* 41.1 (May 2012), pp. 298–312. DOI: `10.1016/J.ENERGY.2012.02.054`. URL: `https://www.sciencedirect.com/science/article/pii/S0360544212001685`.

[3] M. Bilgili, A. Yaşar, and E. Şimşek. “Offshore wind power development in Europe and its comparison with onshore counterpart”. In: *Renewable & Sustainable Energy Reviews* 15.2 (Feb. 2011), pp. 905–915. DOI: `10.1016/J.RSER.2010.11.006`. URL: `https://www.sciencedirect.com/science/article/pii/S1364032110003758`.

[4] A. Tsouvalas. “Underwater Noise Emission Due to Offshore Pile Installation: A Review”. In: *Energies* 13.12 (June 2020), p. 3037. DOI: `10.3390/EN13123037`. URL: `https://www.mdpi.com/1996-1073/13/12/3037/htm`.

[5] J.K. Kaldellis and M. Kapsali. “Shifting towards offshore wind energy—Recent activity and future development”. In: *Energy Policy* 53 (Feb. 2013), pp. 136–148. DOI: `10.1016/J.ENPOL.2012.10.032`. URL: `https://www.sciencedirect.com/science/article/pii/S0301421512008907`.

[6] I. Galparsoro, I. Menchaca, J.M. Garmendia, Á. Borja, A.D. Maldonado, G. Iglesias, and J. Bald. “Reviewing the ecological impacts of offshore wind farms”. In: *npj Ocean Sustainability* 1.1 (Aug. 2022). DOI: `10.1038/s44183-022-00003-5`. URL: `https://www.nature.com/articles/s44183-022-00003-5.pdf`.

[7] A. Hawkins. “The Potential Impact of Offshore Wind Farms on Fishes and Invertebrates”. In: *Advances in Oceanography & Marine Biology* 2 (Dec. 2020). DOI: `10.33552/AOMB.2020.02.000539`.

[8] P.H. Dahl, C.A.F. de Jong, and A.N. Popper. “The Underwater Sound Field from Impact Pile Driving and Its Potential Effects on Marine Life”. In: *Acoustics Today* (2015). URL: `https://api.semanticscholar.org/CorpusID:49365243`.

[9] M.A. Bellmann. “Overview of existing noise mitigation systems for reducing pile-driving noise”. In: *INTERNOISE 2014 - 43rd International Congress on Noise Control Engineering: Improving the World Through Noise Control* (Jan. 2014).

[10] K.H. Elmer and J. Savery. “New Hydro Sound Dampers to reduce piling underwater noise”. In: *Proceedings of Inter-noise 2014*. Melbourne, Australia: International Institute of Noise Control Engineering, 2014, pp. 1–10.

[11] C. Troussard, L. Dufrechou, P.A. Tremblin, and Y. Eustache. “Real-time monitoring of Coastal & Offshore Construction Noise for immediate decision making”. In: *Day 2 Tue, October 03, 2023* (Oct. 2023). DOI: `10.2118/217053-ms`.

[12] C.A.F. de Jong, M.A. Ainslie, and G. Blacquière. *Standard for measurement and monitoring of underwater noise, Part II: procedures for measuring underwater noise in connection with offshore wind farm licensing*. Tech. rep. TNO-DV 2011 C251. Commissioned by the Netherlands Ministry of Infrastructure and the Environment, Directorate-General for Water Affairs. The Hague, The Netherlands: TNO – Netherlands Organisation for Applied Scientific Research, 2011. URL: `https://tethys.pnnl.gov/sites/default/files/publications/TNO-Report-2011.pdf`.

[13] J. Elzinga, A. Mesu, E. van Eekelen, M.S. Wochner, E. Jansen, and M.J. Nijhof. “Manuscript Title: Installing Offshore Wind Turbine Foundations Quieter: A Performance Overview of the First Full-Scale Demonstration of the AdBm Underwater Noise Abatement System”. In: *Day 2 Tue, May 07, 2019* (2019). URL: `https://api.semanticscholar.org/CorpusID:150186811`.

[14] John Ginkel. *Oord, AdBm Technologies en TNO reduceren onderwatergeluid met AdBm geluidsmitigatiesysteemVan Oord reduceert onderwatergeluid bij heien op zee met het AdBm geluidsmitigatiesysteem*. May 2019. URL: `https://linkmagazine.nl/oord-adbm-technologies-en-tno-reduceren-onderwatergeluid-met-adbm-geluidsmitigatiesysteem/?v=1a13105b7e4e`.

[15] AdBm Technologies. *Technology*. Accessed on 2024-09-10. 2020. URL: `https://adbmtech.com/technology/`.

[16] Mark Wochner. *AdBm Noise Mitigation System 2018 Demonstration Results*. Tech. rep. AdBm Technologies, Aug. 2019. URL: `https://adbmtech.com/wp-content/uploads/2020/08/AdBm-2018-Demonstration-Public-Release-Final-edit.pdf`.

[17] Arunjyoti Sarkar and Ove T. Gudmestad. “Splash Zone Lifting Analysis of Subsea Structures”. In: *29th International Conference on Ocean, Offshore and Arctic Engineering: Volume 1*. International Conference on Offshore Mechanics and Arctic Engineering. June 2010, pp. 303–312. DOI: `10.1115/OMAE2010-20489`. eprint: `https://asmedigitalcollection.asme.org/OMAE/proceedings-pdf/OMAE2010/49095/303/4590415/303_1.pdf`. URL: `https://doi.org/10.1115/OMAE2010-20489`.

[18] Frøydis Solaas and Peter Sandvik. “Hydrodynamic Coefficients for Suction Anchors During Installation Operations”. In: *Proceedings of the ASME 2017 36th International Conference on Ocean, Offshore and Arctic Engineering (OMAE)*. June 2017, V009T12A031. DOI: `10.1115/OMAE2017-62447`.

[19] Det Norske Veritas. *Recommended Practice DNV-RP-H103: Modelling and Analysis of Marine Operations*. Høvik, Norway, Apr. 2011.

[20] Det Norske Veritas. *Recommended Practice DNV-RP-C205: Environmental Conditions and Environmental Loads*. August 2017. Høvik, Norway, Aug. 2017.

[21] Fredrik Mentzoni. “Hydrodynamic Loads on Complex Structures in the Wave Zone”. In: *Proceedings of the NTNU Doctoral Meeting*. ISBN: 978-82-326-4667-8.

[22] Long fei Cong and Bin Teng. “Hydrodynamic Characteristics of Square Heaving Plates with Opening Under Forced Oscillation”. In: *China Ocean Engineering* 33.6 (Dec. 2019), pp. 637–648. ISSN: 21918945. DOI: `10.1007/s13344-019-0063-z`.

[23] G.H. Keulegan and L.H. Carpenter. “Forces on cylinders and plates in an oscillating fluid”. In: *Journal of Research of the National Bureau of Standards* 60.5 (May 1958), p. 423. DOI: `10.6028/jres.060.043`.

[24] Hai zhi Liang, Kun Liu, Lu yu Li, and Jin ping Ou. “Dynamic Performance Analysis of the Tuned Heave Plate System for Semi-Submersible Platform”. In: *China Ocean Engineering* 32.4 (Aug. 2018), pp. 422–430. ISSN: 21918945. DOI: `10.1007/s13344-018-0044-7`.

[25] Jinxuan Li, Shuxue Liu, Min Zhao, and Bin Teng. “Experimental investigation of the hydrodynamic characteristics of heave plates using forced oscillation”. In: *Ocean Engineering* 66 (2013), pp. 82–91. ISSN: 00298018. DOI: `10.1016/j.oceaneng.2013.04.012`.

[26] Kie Hian Chua, David Clelland, Shan Huang, and Andy Sworn. “Model experiments of hydrodynamic forces on heave plates”. In: *Proceedings of the International Conference on Offshore Mechanics and Arctic Engineering - OMAE*. Vol. 1 B. 2005, pp. 943–948. DOI: `10.1115/OMAE2005-67459`.

[27] Kun Liu, Haizhi Liang, Jingpin Ou, Jiawei Ye, and Dongjiao Wang. “Experimental Investigation of the Performance of a Tuned Heave Plate Energy Harvesting System for a Semi-Submersible Platform”. In: *Journal of Marine Science and Engineering* 10.1 (2022). ISSN: 2077-1312. DOI: `10.3390/jmse10010045`. URL: `https://www.mdpi.com/2077-1312/10/1/45`.

[28] Longbin Tao and Daniel Dray. “Hydrodynamic performance of solid and porous heave plates”. In: *Ocean Engineering* 35.10 (2008), pp. 1006–1014. ISSN: 0029-8018. DOI: `https://doi.org/10.1016/j.oceaneng.2008.03.003`. URL: `https://www.sciencedirect.com/science/article/pii/S0029801808000589`.

[29] M. Turner, L. Wang, K. Sharman, and A. Robertson. “Heave Plate Hydrodynamic Coefficients for Floating Offshore Wind Turbines – A Compilation of Data”. In: *Proceedings of the International Offshore Wind Technical Conference (IOWTC)*. Jan. 2024. DOI: `10.1115/IOWTC2023-119414`.

[30] Xinliang Tian, Longbin Tao, Xin Li, and Jianmin Yang. “Hydrodynamic coefficients of oscillating flat plates at $0.15 \leq KC \leq 3.15$”. In: *Journal of Marine Science and Technology (Japan)* 22.1 (Mar. 2017), pp. 101–113. ISSN: 09484280. DOI: `10.1007/s00773-016-0401-2`.

[31] Xin Liang Tian, Jian Min Yang, Xin Li, and Yu Gao Shen. “Effects of Reynolds number on the hydrodynamic characteristics of heave damping plate”. In: *Chuan Bo Li Xue/Journal of Ship Mechanics* 17 (12 Dec. 2013), pp. 1392–1402. ISSN: 10077294. DOI: `10.3969/j.issn.1007-7294.2013.12.004`.

[32] Hans Lindenchrone Dueholm and Lars Kristensen. “Hydrodynamic Effects of Heave Plates”. Supervisors: Jonas Bjerg Thomsen and Mads Røge Eldrup. Master’s thesis. Aalborg, Denmark: Aalborg University, Department of Civil Engineering, 2021. URL: `http://www.civil.aau.dk`.

[33] Song Ann and Odd M. Faltinsen. “An experimental and numerical study of heave added mass and damping of horizontally submerged and perforated rectangular plates”. In: *Journal of Fluids and Structures* 39 (2013), pp. 87–101. ISSN: 10958622. DOI: `10.1016/j.jfluidstructs.2013.03.004`.

[34] Krish Thiagarajan and Javier Moreno. “Wave induced effects on the hydrodynamic coefficients of an oscillating heave plate in offshore wind turbines”. In: *Journal of Marine Science and Engineering* 8.8 (Aug. 2020). ISSN: 20771312. DOI: `10.3390/JMSE8080622`.

[35] C. Garrido-Mendoza, A. Souto-Iglesias, and K. Sharman. “Numerical Simulation of Hydrodynamics of a Circular Disk Oscillating Near a Seabed”. In: *Proceedings of the International Conference on Offshore Mechanics and Arctic Engineering - OMAE* 9 (June 2013). DOI: `10.1115/OMAE2013-11072`.

[36] Subrata K. Chakrabarti. *Handbook of Offshore Engineering*. Elsevier, June 2005. URL: `https://www.amazon.com/Handbook-Offshore-Engineering-Elsevier-Ocean-ebook/dp/B00D0V3KF0`.

[37] Mojtaba Ezoji, Naser Shabakhty, and Longbin Tao. “Hydrodynamic damping of solid and perforated heave plates oscillating at low KC number based on experimental data: A review”. In: *Ocean Engineering* 253 (2022), p. 111247. ISSN: 0029-8018. DOI: `https://doi.org/10.1016/j.oceaneng.2022.111247`. URL: `https://www.sciencedirect.com/science/article/pii/S0029801822006424`.

[38] Lixian Zhang, Wei Shi, Yuxin Zeng, Constantine Michailides, Siming Zheng, and Ying Li. “Experimental investigation on the hydrodynamic effects of heave plates used in floating offshore wind turbines”. In: *Ocean Engineering* 267 (2023), p. 113103. ISSN: 0029-8018. DOI: `https://doi.org/10.1016/j.oceaneng.2022.113103`. URL: `https://www.sciencedirect.com/science/article/pii/S0029801822023861`.

[39] B. MOLIN. “ON THE ADDED MASS AND DAMPING OF PERIODIC ARRAYS OF FULLY OR PARTIALLY POROUS DISKS”. In: *Journal of Fluids and Structures* 15.2 (2001), pp. 275–290. ISSN: 0889-9746. DOI: `https://doi.org/10.1006/jfls.2000.0338`. URL: `https://www.sciencedirect.com/science/article/pii/S0889974600903384`.

[40] Longbin Tao, Bernard Molin, Yves-Marie Scolan, and Krish P. Thiagarajan. “Spacing effects on hydrodynamics of heave plates on offshore structures”. In: *Journal of Fluids and Structures* 23.8 (2007), pp. 1119–1136. DOI: `10.1016/j.jfluidstructs.2007.03.004`. URL: `https://hal.science/hal-00442677`.

[41] J. M. R. Graham. “The forces on sharp-edged cylinders in oscillatory flow at low Keulegan-Carpenter numbers”. In: *Journal of Fluid Mechanics* 97.1 (1980), pp. 331–346. DOI: `10.1017/S0022112080002595`.

[42] Anthony J. Martyr and David R. Rogers. “Chapter 16 - The Combustion Process and Combustion Analysis”. In: *Engine Testing*. Ed. by Anthony J. Martyr and David R. Rogers. 5th ed. Oxford: Butterworth-Heinemann, 2021, pp. 537–597. ISBN: 978-0-12-821226-4. DOI: `10.1016/B978-0-12-821226-4.00016-4`. URL: `https://www.sciencedirect.com/science/article/pii/B9780128212264000164`.

[43] A. Bezunartea-Barrio, A. Maron-Loureiro, F. Moreno-Buron, S. Fernandez-Ruano, J. Rios-Tubio, J. Oria-Escudero, C. Soriano-Gomez, C. Lopez-Pavon, E. Molinelli-Fernandez, A. Souto-Iglesias, and A. Valea-Peces. “Scale effects on heave plates for floating offshore wind turbines”. In: *Proceedings of the International Conference on Offshore Mechanics and Arctic Engineering - OMAE*. Vol. 11A. 2018. ISBN: 9780791851326. DOI: `10.1115/OMAE2018-78062`.

[44] J.M.J. Journée and W.W. Massie. *Offshore Hydromechanics*. Second. Delft: Delft University of Technology, June 2008.

[45] A. M. Elzinga, J. D. Stroo, and A. A. Kana. “A comparative analysis of side and stern installation of a monopile lifting operation using a heavy lift crane vessel”. In: *International Marine Design Conference* (May 2024). DOI: `10.59490/imdc.2024.822`. URL: `https://proceedings.open.tudelft.nl/imdc24/article/view/822`.

[46] Wilson Guachamin, Lin Li, Zhen Gao, and Torgeir Moan. “Methodology for assessment of the operational limits and operability of marine operations”. In: *Ocean Engineering* 125 (Aug. 2016), pp. 308–327. DOI: `10.1016/j.oceaneng.2016.08.015`.

[47] TU Delft. *Towing Tank No. 2*. URL: `https://www.tudelft.nl/me/over/afdelingen/maritime-and-transport-technology/research/ship-hydromechanics/facilities/towing-tank-no-2`.

[48] *LINEAR MOTORS P01-48x360F*. 24. LinMot. URL: `https://shop.linmot.com/data/import/Dokumente/0185-1005-E_1V0_DS_Linear_Motors_P01-48x360F.pdf`.

[49] Mohammed (Shameem) Islam, Fatima Jahra, and Scott Hiscock. “Data analysis methodologies for hydrodynamic experiments in waves”. In: *Journal of Naval Architecture and Marine Engineering* 13.1 (2016), p. 1. DOI: `10.3329/jname.v13i1.25347`.

[50] Howard Austerlitz. *CHAPTER 4 - Analog/Digital Conversions*. Ed. by Howard Austerlitz. Second Edition. San Diego: Academic Press, 2003, pp. 51–77. ISBN: 978-0-12-068377-2. DOI: `https://doi.org/10.1016/B978-012068377-2/50004-8`. URL: `https://www.sciencedirect.com/science/article/pii/B9780120683772500048`.

[51] Michael Patrick Allen. “The problem of multicollinearity”. In: *Understanding Regression Analysis*. Boston, MA: Springer US, 1997, pp. 176–180. ISBN: 978-0-585-25657-3. DOI: `10.1007/978-0-585-25657-3_37`. URL: `https://doi.org/10.1007/978-0-585-25657-3_37`.

[52] C. Vuik, P. van Beek, F. Vermolen, and J. van Kan. *Numerieke Methoden voor Differentiaalvergelijkingen*. Delft, The Netherlands: Delft Institute of Applied Mathematics, Delft University of Technology, 2004. URL: `https://www.researchgate.net/publication/267301500_Numerieke_Methoden_voor_Differentiaalvergelijkingen`.

[53] Steven C. Chapra and Raymond P. Canale. *Numerical Methods for Engineers*. 7th ed. New York: McGraw-Hill Education, 2015. ISBN: 978-0-07-339792-4.

[54] Mia Abrahamsen Prsic, Frøydis Solaas, and Trygve Kristiansen. “Hydrodynamic Coefficients of Generic Subsea Modules in Forced Oscillation Tests—Importance of Structural Elements”. In: *Journal of Offshore Mechanics and Arctic Engineering* 146.1 (Feb. 2024). ISSN: 1528896X. DOI: `10.1115/1.4062293`.

A

Sensor calibration

A.1. Load cell calibration

Both load cells were calibrated according to ITTC standards before the experiments. The output voltages are measured in 15 steps by increasing the mass with steps of 0.2 kg starting with zero mass up to 2.8 kg and then decreasing the mass with steps of 0.2 to zero mass again. The voltage of each step is measured with a duration of 30 seconds. This procedure is performed on both the positive and negative voltage outputs of both load cells. The output voltage is corrected with the voltage value that is measured with zero mass. The vertical force is equal to the mass times the gravitational constant and is plotted against the corrected voltage to get the calibration factor. The calibration factor is equal to the inverse of the slope of Figure A.1a and Figure A.2a. The normalised residuals of the corrected voltage and the expected voltage are provided in Figure A.1b and Figure A.2b. The calibration factors and the averaged normalised residual of both load cells are given in Table A.1.

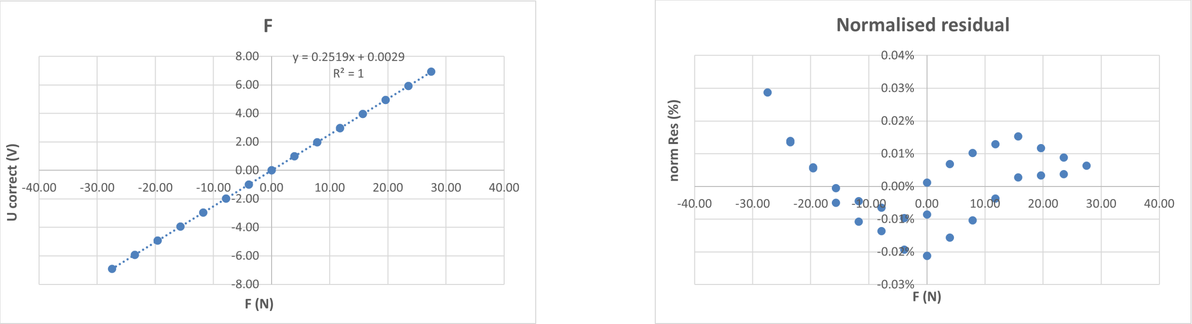

(a) Force vs corrected voltage output for load cell 1.

(b) Normalised residuals for load cell 1.

Figure A.1: Calibration results for load cell 1.

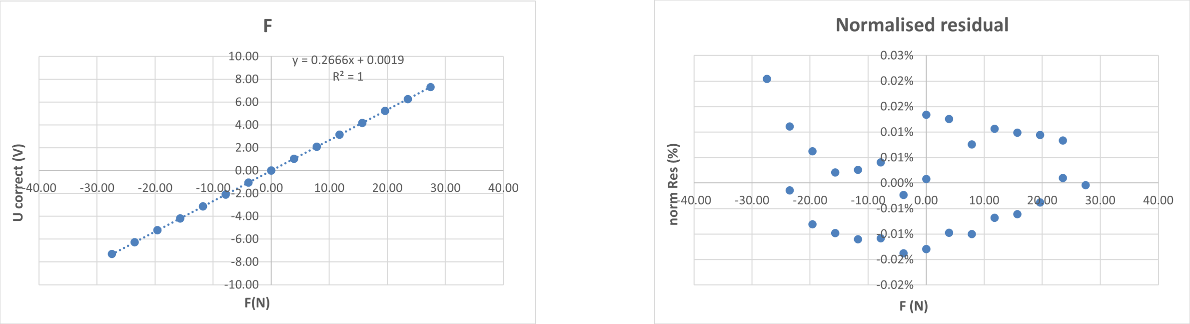

(a) Force vs corrected voltage output for load cell 2.

(b) Normalised residuals for load cell 2.

Figure A.2: Calibration results for load cell 2.

Table A.1: Calibration results of the load cells.

	Calibration factor (N/V)	Averaged normalised residual
Load cell 1	3.970	0.01%
Load cell 2	3.751	0.008%

A.2. Wave height sensor calibration

The wave height sensors are calibrated by measuring the output voltage for 11 different sensor heights with a total of 21 steps. The duration of the steps was 30 seconds with step heights of 40 mm, which start at 0 mm and increase to 400 mm and again decrease to 0 mm. The calibration is performed each day. An example of calibration measurement is given in Figure A.3 and Figure A.4 for wave height sensor 1 and wave height sensor 2, respectively. Table A.2 shows the resulting calibration factors and the averaged normalised residual values for each day.

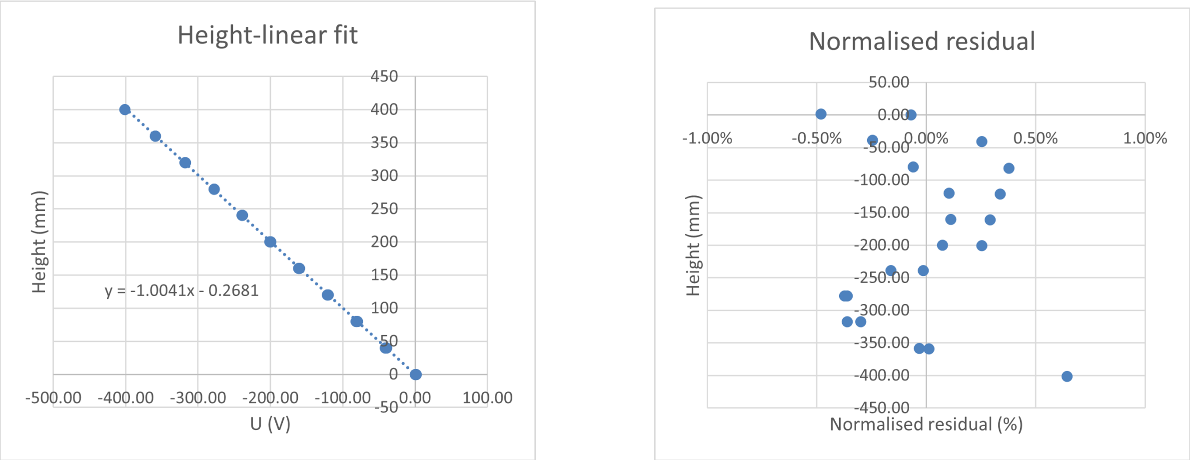

(a) Height vs voltage output for wave height sensor 1.

(b) Normalised residuals for wave height sensor 1.

Figure A.3: Calibration results for wave height sensor 1.

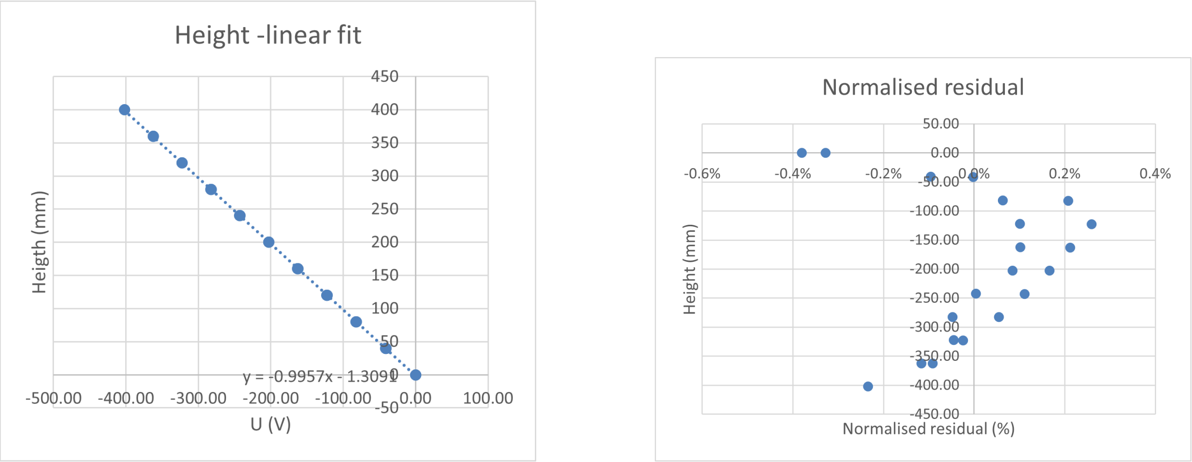

(a) Height vs voltage output for wave height sensor 2. **(b)** Normalised residuals for wave height sensor 2.

Figure A.4: Calibration results for wave height sensor 2.

Table A.2: Calibration results of the wave height sensors.

	Wave height sensor 1 (front)		Wave height sensor 2 (model height)	
	Calibration factor (mm/V)	Averaged normalised residual	Calibration factor (mm/V)	Averaged normalised residual
23-Apr	37.50	0.21%	26.48	0.12%
24-Apr	37.30	0.27%	26.52	0.13%
25-Apr	37.41	0.26%	26.50	0.11%
28-Apr	37.00	0.19%	26.93	0.11%
29-Apr	37.19	0.28%	27.01	0.09%
30-Apr	36.36	0.19%	26.95	0.10%
1-May	36.67	0.33%	26.83	0.13%

B

Data-processing

B.1. Ordinary Least Square Method

The least squares method is a numerical optimisation method, which can solve m unknowns for n equations where $n > m$ [52]. It minimises the sum of the squared value of the difference between the measured and predicted values. This is given in Equation B.1, where r_i is the residual and x_i is the variable that must be optimised.

$$\psi^2(x_1) = \sum_{i=1}^{n}(r_i)^2 \tag{B.1}$$

To achieve the minimum value

$$\frac{d\psi^2(x_1)}{dx_1} = 0 \tag{B.2}$$

is required. If there is a system with n equations and m unknowns, the system can be written as

$$\begin{bmatrix} a_1 & a_2 & a_3 \\ \vdots & \vdots & \vdots \\ \vdots & \vdots & \vdots \\ a_n & a_n & a_n \end{bmatrix} \begin{bmatrix} x_1 \\ \vdots \\ x_m \end{bmatrix} = \begin{bmatrix} b_1 \\ \vdots \\ \vdots \\ b_n \end{bmatrix}. \tag{B.3}$$

Equation B.3 can be rewritten in

$$Ax = b. \tag{B.4}$$

This is a set of equations where the matrix A has known coefficients, vector x is the vector with unknown coefficients, and vector b is the solution vector. The least square- solution of the $m \times n$ system Ax = b satisfies the $m \times m$ system

$$A^TAx = A^Tb. \tag{B.5}$$

Where the unknown coefficients in vector x can be found with

$$x = (A^TA)^{-1}A^Tb. \tag{B.6}$$

B.2. Correlation

The correlation coefficient quantifies how strongly two data sets are linearly related to each other. The value of the correlation coefficient can be found with Equation B.7, where X and Y are the data sets of the two variables. The numerator is the covariance, and the denominator is the product of the standard deviations. The coefficient has values between -1 and 1, where a value of 1 or -1 means a strong relationship between the data sets, and a value of 0 means no linear relationship. A value of +1 means that X and Y increase linearly together, and a value of -1 indicates that one data set increases while the other data set decreases.

$$\rho_{X,Y} = \frac{\text{cov}(X,Y)}{\sigma_X \sigma_Y} \tag{B.7}$$

For n samples, the correlation coefficient is equal to Equation B.8. $\bar{X}$ and $\bar{Y}$ are the means of the data set.

$$\rho_{X,Y} = \frac{\sum_{i=1}^{n}(X_i - \bar{X})(Y_i - \bar{Y})}{\sqrt{\sum_{i=1}^{n}(X_i - \bar{X})^2}\sqrt{\sum_{i=1}^{n}(Y_i - \bar{Y})^2}} \tag{B.8}$$

B.3. Goodness of the fits

B.3.1. Coefficient of determination (R^2)

The coefficient of determination indicates how well the predicted line fits the actual measured line. The coefficient is used to indicate how well the regression model represents the measured data. The coefficient of determination can be calculated with Equation B.9 [53]. The value is between 0 and 1.0, where a value of 1.0 means that the predicted data represent the measured data well. y_m is the measured value, $\bar{y}$ the average value of the measured data, and y_{pred} is the predicted value of the regression method.

$$R^2 = 1 - \frac{\sum(y_m - y_{pred})^2}{\sum(y_m - \bar{y})^2} = 1 - \frac{SS_{res}}{SS_{tot}} \tag{B.9}$$

B.3.2. Root Mean Square Error (RMSE)

The RMSE determines the average value of the sum of the quadratic residual values and determines the standard error of the estimation in the same unit as the data. The RMSE is a measure of accuracy where the spread of the data is quantified [53]. The RMSE is calculated with Equation B.10. A value of zero indicates that the predicted values match the measured data precisely. n is the amount of samples, y_m the measured value, and y_{pred} the predicted value from the regression method. Lower RMSE values lead to more accurate prediction models.

$$RMSE = \sqrt{\frac{1}{n}\sum_{i=1}^{n}(y_m - y_{pred})^2} \tag{B.10}$$

To quantify the value of the RMSE with the measured data, the RMSE value is normalised, which is named the NRMSE. The NRMSE is given in Equation B.11. The peak-to-peak value is taken to normalise the RMSE with the full range of measured data.

$$NRMSE = \frac{RMSE}{y_{m,max} - y_{m.min}} \times 100\% \tag{B.11}$$

B.4. First-order wave theory and Stokes' second-order wave theory

If the depth of the water decreases for waves with the same frequencies, the ratio $\frac{h}{\lambda}$ decreases. For deep water, this value is larger than 0.5 and $\tanh kh$ is close to one. Additionally, when the wave steepness $\frac{H}{\lambda}$ increases, higher-order effects will become more significant. The contribution of the second-order wave components increases when $\frac{h}{\lambda}$ decreases and $\frac{H}{\lambda}$ increases. This results in the wave profile having sharp crests and flat troughs, where the crests are higher than the troughs are deep. The following subsections provide the equations for the wave profile, horizontal velocities, and horizontal accelerations from Chakrabarti [36].

B.4.1. First-order wave theory

The first-order wave elevation, the horizontal particle fluid velocity, and the horizontal particle fluid acceleration are given in Equations B.12, B.13 and B.14, respectively.

- H: wave height (m)
- k: wave number ($\frac{1}{\text{m}}$)
- h: water depth (m)
- z: vertical position (negative below water surface) (m)
- T: Wave period (s)
- ω: wave frequency (rad/s)
- x: horizontal position (m)
- t: time (s)

$$\eta^{(1)} = \frac{H}{2}\cos(kx - \omega t) \tag{B.12}$$

$$u^{(1)} = \frac{\pi H}{T} \cdot \frac{\cosh(k(h+z))}{\sinh(kh)}\cos(kx - \omega t) \tag{B.13}$$

$$\dot{u}^{(1)} = \frac{2\pi^2 H}{T^2} \cdot \frac{\cosh(k(h+z))}{\sinh(kh)}\sin(kx - \omega t) \tag{B.14}$$

B.4.2. Second-order wave theory

The second-order wave elevation, horizontal particle fluid velocity component, and horizontal particle fluid acceleration component are given in Equations B.15, B.17 and B.19, respectively. The total wave elevation, horizontal particle velocity and horizontal particle acceleration, including the second-order components, are provided in Equations B.16, B.18 and B.20.

$$\eta^{(2)} = \frac{\pi H^2}{8L} \cdot \frac{\cosh(kh)}{\sinh^3(kh)}\left[2 + \cosh(2kh)\right]\cos\left(2(kx - \omega t)\right) \tag{B.15}$$

$$\eta = \eta^{(1)} + \eta^{(2)} \tag{B.16}$$

$$u^{(2)} = \frac{3}{4c}\left(\frac{\pi H}{T}\right)^2 \frac{\cosh(2k(h+z))}{\sinh^4(kh)}\cos\left(2(kx - \omega t)\right) \tag{B.17}$$

$$u = u^{(1)} + u^{(2)} \tag{B.18}$$

$$\dot{u}^{(2)} = \frac{3\pi}{2L}\left(\frac{\pi H}{T}\right)^2 \frac{\cosh(2k(h+z))}{\sinh^4(kh)}\sin\left(2(kx - \omega t)\right) \tag{B.19}$$

$$\dot{u} = \dot{u}^{(1)} + \dot{u}^{(2)} \tag{B.20}$$

C

Additional pictures from experiments

This appendix provides pictures of the experimental setup performed in the small towing tank at the University of Technology Delft.

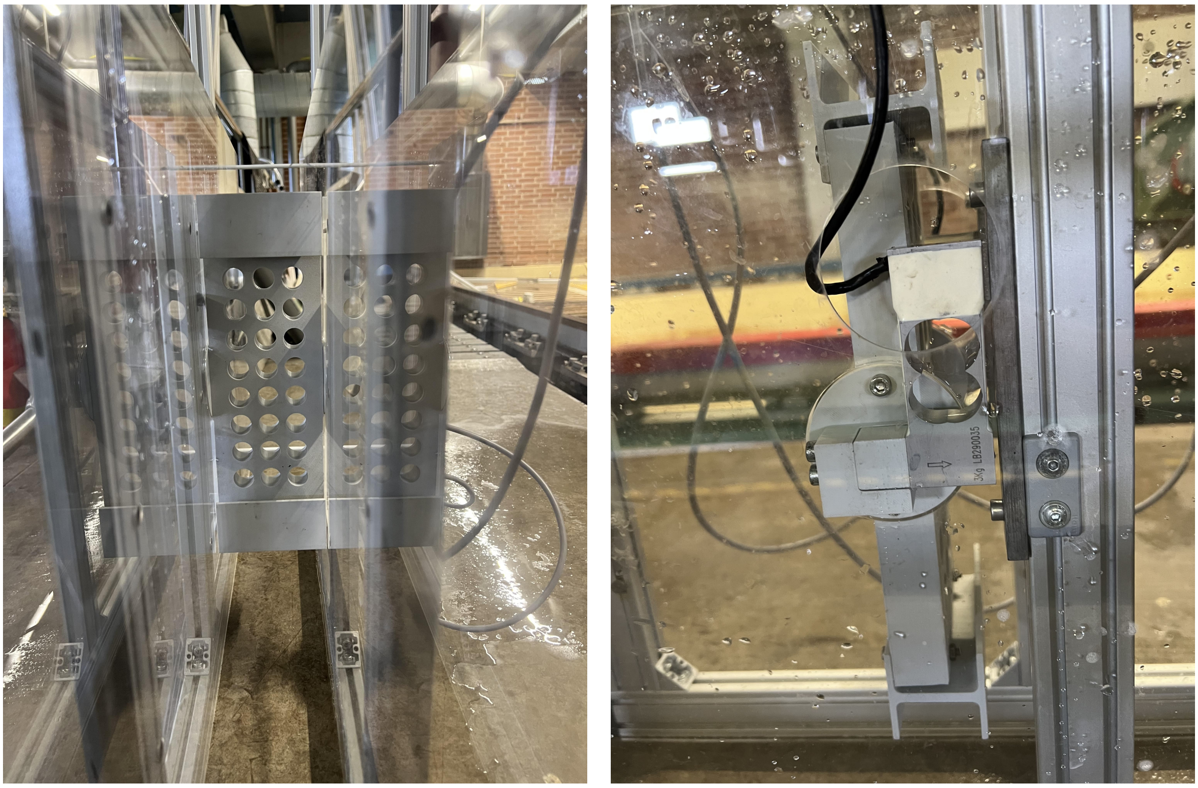

(a) Vertically oriented panel with little space between the panel and end plate.

(b) Closer view on the side of the panel.

Figure C.1: Pictures of the front and side view of the experimental setup.

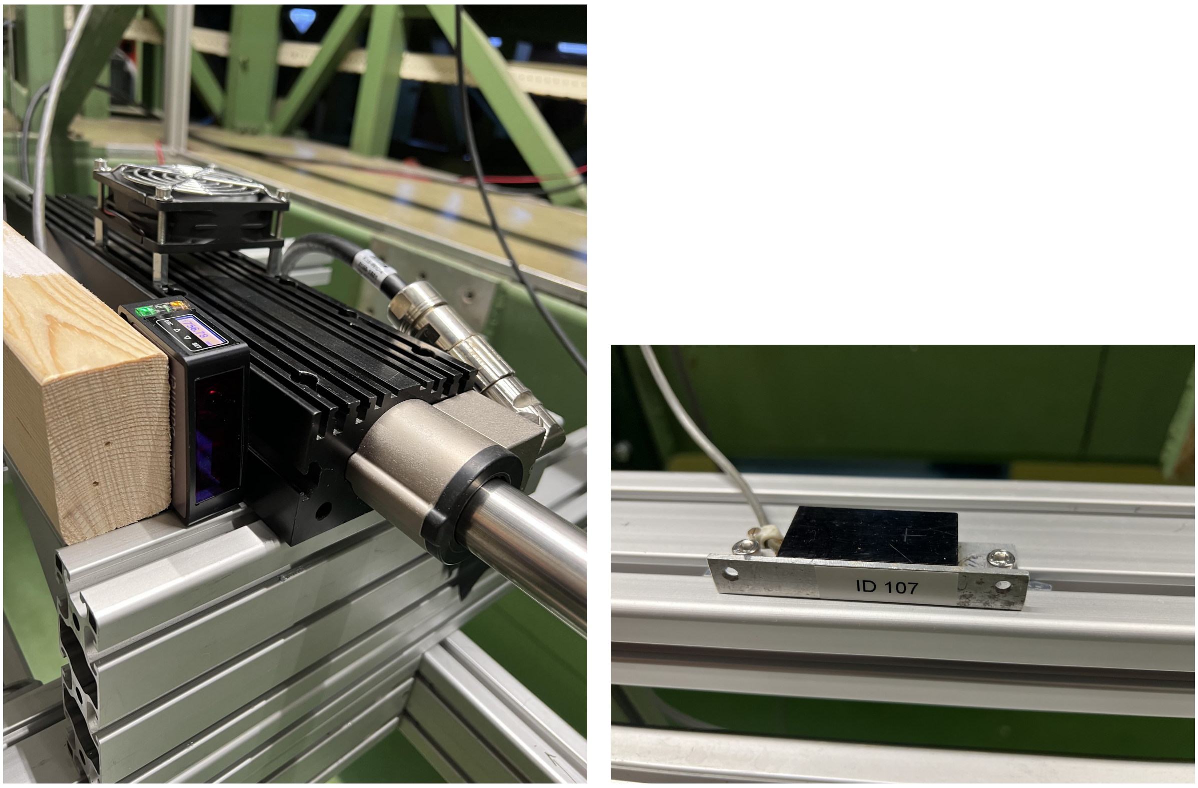

(a) Picture of the position sensor and linear motor.

(b) Picture of the acceleration sensor.

Figure C.2: Pictures of the position sensor, acceleration sensor and linear motor.

D

Overview of the results

This appendix provides an overview of the resulting values of the hydrodynamic coefficients from the experiments with the R^2, RMSE and NRMSE values. Table D.1 lists an overview of the resulting KC values for the first 20 m and wave periods between 4.5 and 12 seconds. This table consists of wave periods longer than 9.0 seconds, which are outside the range of this study. However, it cannot be ruled out that these wave periods may not be present in practice and are shown in the table for this reason.

Table D.1: Overview of the values of KC for range of wave periods for H = 2.5 m.

H = 2.5m	T = 4.5s	T = 5.0s	T = 5.5s	T = 6.0s	T = 6.5s	T =7.0s	T = 7.5s	T = 8.0s	T = 8.5s	T = 9.0s	T = 9.5s	T = 10s	T = 11s	T = 12s
Depth (m)	KC	KC	KC	KC	KC	KC	KC	KC	KC	KC	KC	KC	KC	KC
0	10.4	10.4	10.4	10.4	10.4	10.4	10.4	10.5	10.6	10.7	10.9	11.0	11.5	12.0
-1	8.5	8.8	9.1	9.3	9.4	9.6	9.7	9.8	10.0	10.2	10.4	10.6	11.1	11.7
-2	7.0	7.5	7.9	8.3	8.6	8.8	9.0	9.2	9.5	9.7	9.9	10.2	10.8	11.4
-3	5.7	6.4	7.0	7.4	7.8	8.1	8.4	8.7	9.0	9.2	9.5	9.8	10.4	11.1
-4	4.7	5.4	6.1	6.6	7.1	7.5	7.8	8.2	8.5	8.8	9.1	9.4	10.1	10.8
-5	3.8	4.6	5.3	5.9	6.4	6.9	7.3	7.7	8.0	8.4	8.7	9.1	9.8	10.5
-6	3.1	3.9	4.7	5.3	5.9	6.4	6.8	7.2	7.6	8.0	8.3	8.7	9.5	10.2
-7	2.6	3.4	4.1	4.7	5.3	5.9	6.3	6.8	7.2	7.6	8.0	8.4	9.2	10.0
-8	2.1	2.9	3.6	4.2	4.8	5.4	5.9	6.4	6.8	7.2	7.7	8.1	8.9	9.7
-9	1.7	2.4	3.1	3.8	4.4	5.0	5.5	6.0	6.5	6.9	7.4	7.8	8.6	9.5
-10	1.4	2.1	2.7	3.4	4.0	4.6	5.1	5.6	6.1	6.6	7.1	7.5	8.4	9.2
-11	1.2	1.8	2.4	3.0	3.6	4.2	4.8	5.3	5.8	6.3	6.8	7.2	8.1	9.0
-12	1.0	1.5	2.1	2.7	3.3	3.9	4.5	5.0	5.5	6.0	6.5	7.0	7.9	8.8
-13	0.8	1.3	1.8	2.4	3.0	3.6	4.2	4.7	5.2	5.7	6.2	6.7	7.7	8.6
-14	0.6	1.1	1.6	2.2	2.8	3.3	3.9	4.4	5.0	5.5	6.0	6.5	7.5	8.4
-15	0.5	0.9	1.4	1.9	2.5	3.1	3.6	4.2	4.7	5.3	5.8	6.3	7.3	8.2
-16	0.4	0.8	1.2	1.7	2.3	2.8	3.4	3.9	4.5	5.0	5.6	6.1	7.1	8.1
-17	0.4	0.7	1.1	1.6	2.1	2.6	3.2	3.7	4.3	4.8	5.4	5.9	6.9	7.9
-18	0.3	0.6	1.0	1.4	1.9	2.4	3.0	3.5	4.1	4.6	5.2	5.7	6.7	7.7
-19	0.2	0.5	0.8	1.3	1.7	2.2	2.8	3.3	3.9	4.4	5.0	5.5	6.6	7.6
-20	0.2	0.4	0.7	1.1	1.6	2.1	2.6	3.1	3.7	4.3	4.8	5.4	6.4	7.4

D.1. Overview results model SH

Table D.2: Heave forced oscillation results of model SH using one panel.

A(m)	**T (s)**	**KC**	C_a	C_d	C_b	F_{amp} (N)	$R^2_{C_d}$	$R^2_{C_b}$	**RMSE**$_{C_d}$ (N)	**RMSE**$_{C_b}$ (N)	**NRMSE**$_{C_d}$ (%)	**NRMSE**$_{C_b}$ (%)
0.07	2.85	1.4	0.62	4.51	0.58	2.2	0.94	0.98	0.34	0.21	7.7	4.74
0.16	2.85	3.4	0.76	3.31	1.00	7.7	0.92	0.98	1.35	0.74	8.8	4.83
0.16	4.27	3.4	0.80	3.41	1.04	3.8	0.95	0.98	0.51	0.28	6.7	3.63
0.25	2.85	5.2	0.87	2.96	1.37	15.9	0.88	0.96	3.27	1.97	10.3	6.19
0.25	4.27	5.1	0.92	2.91	1.38	7.7	0.91	0.97	1.31	0.72	8.5	4.65
0.25	5.69	5.1	0.96	2.94	1.39	4.3	0.92	0.98	0.72	0.38	8.2	4.38
0.32	2.85	6.6	0.93	2.78	1.58	26.7	0.84	0.92	5.62	3.99	10.5	7.48
0.32	4.27	6.6	1.03	2.74	1.63	11.6	0.89	0.96	2.15	1.15	9.3	5.57
0.32	5.69	6.5	1.08	2.74	1.64	6.5	0.90	0.97	1.29	0.65	8.8	4.99
0.44	4.27	9.1	1.21	2.46	2.02	18.9	0.87	0.95	4.05	2.56	10.7	6.77
0.44	5.69	9.1	1.27	2.47	2.05	10.8	0.90	0.97	2.00	1.14	9.3	5.29
0.53	5.69	10.9	1.39	2.31	2.29	14.0	0.89	0.96	2.78	1.63	10.0	5.83
0.57	5.69	11.9	1.44	2.25	2.42	15.2	0.90	0.97	3.10	1.77	10.2	5.80

Table D.3: Heave forced oscillation results of model SH using panels in series.

A (m)	**T (s)**	**KC**	C_a	C_d	C_b	F_{amp} (N)	$R^2_{C_d}$	$R^2_{C_b}$	**RMSE**$_{C_d}$ (N)	**RMSE**$_{C_b}$ (N)	**NRMSE**$_{C_d}$ (%)	**NRMSE**$_{C_b}$ (%)
0.16	2.85	3.40	0.73	2.76	0.85	7.0	0.90	0.96	1.38	0.85	9.8	6.0
0.16	4.27	3.36	0.75	2.76	0.85	3.2	0.93	0.98	0.52	0.27	8.2	4.2
0.25	2.85	5.18	0.90	2.43	1.09	15.8	0.90	0.95	2.74	2.00	8.7	6.3
0.25	4.27	5.16	0.92	2.32	1.08	6.6	0.94	0.98	0.95	0.57	7.2	4.3
0.34	4.27	7.13	1.10	1.73	1.10	9.5	0.93	0.97	1.47	1.02	7.8	5.4
0.32	2.85	6.59	1.00	1.95	1.10	18.3	0.90	0.94	3.70	2.72	10.2	7.5
0.44	4.27	9.12	1.32	1.17	0.96	12.6	0.92	0.96	2.16	1.51	8.7	6.1
0.44	5.69	9.12	1.37	1.19	0.99	7.6	0.94	0.97	1.08	0.72	7.1	4.8
0.53	5.69	10.89	1.48	0.81	0.84	8.4	0.92	0.96	1.53	1.09	9.1	6.5
0.57	5.69	11.88	1.51	0.69	0.80	10.3	0.89	0.94	1.96	1.49	9.5	7.2

Table D.4: Surge forced oscillation results of model SH.

A (m)	**T (s)**	**KC**	C_a	C_d	C_b	F_{amp} (N)	$R^2_{C_d}$	$R^2_{C_b}$	**RMSE**$_{C_d}$ (N)	**RMSE**$_{C_b}$ (N)	**NRMSE**$_{C_d}$ (%)	**NRMSE**$_{C_b}$ (%)
0.16	2.85	3.4	0.79	2.67	0.62	1.10	0.98	1	0.12	0.04	5.84	2.2
0.25	2.85	5.2	0.88	2.32	0.81	1.99	0.97	0.99	0.23	0.1	5.86	2.52
0.25	2.85	5.2	0.89	2.33	0.81	2.01	0.97	0.99	0.24	0.11	5.9	2.63
0.25	4.27	5.2	0.91	2.31	0.83	0.87	0.98	1	0.09	0.04	5.45	2.33
0.32	2.85	6.6	0.94	2.19	0.95	3.07	0.96	0.99	0.39	0.19	6.37	3.06
0.32	4.27	6.6	0.95	2.16	0.96	1.19	0.97	1	0.14	0.06	6.03	2.44
0.32	5.69	6.5	0.99	2.14	0.98	0.71	0.98	1	0.07	0.03	5.16	2.23
0.44	4.27	9.1	0.99	1.97	1.23	1.99	0.96	0.99	0.27	0.12	6.86	3.06
0.44	5.69	9.1	1.02	1.98	1.26	1.19	0.97	1	0.14	0.06	5.66	2.3
0.44	5.69	9.1	1.02	1.99	1.26	1.20	0.97	0.99	0.14	0.06	5.84	2.41
0.53	5.69	10.9	1.07	1.95	1.47	1.59	0.97	0.99	0.19	0.09	5.82	2.71
0.53	5.69	10.9	1.07	1.94	1.46	1.58	0.97	0.99	0.18	0.08	5.76	2.69
0.57	5.69	11.9	1.09	1.91	1.55	1.81	0.97	0.99	0.21	0.09	5.81	2.57

Table D.5: Wave test results using model SH.

A (m)	**T (s)**	**KC**	C_a	C_d	C_b	F_{amp} (N)	$R^2_{C_d}$	$R^2_{C_b}$	**RMSE**$_{C_d}$ (N)	**RMSE**$_{C_b}$ (N)	**NRMSE**$_{C_d}$ (%)	**NRMSE**$_{C_b}$ (%)
0.12	2.85	3.24	0.62	2.53	0.68	5.5	0.93	0.95	0.85	0.7	7.7	6.4
0.12	2.85	3.23	0.62	3.12	0.82	5.9	0.94	0.96	0.85	0.71	7.2	6.0
0.09	2.85	2.51	0.61	3.56	0.73	4.5	0.94	0.96	0.62	0.53	6.9	5.9
0.09	4.27	3.22	0.78	3.7	0.92	3.4	0.88	0.88	0.63	0.63	9.1	9.2
0.05	2.85	1.37	0.54	4.68	0.53	1.9	0.96	0.98	0.23	0.17	5.9	4.3

D.2. Overview results model BH.

Table D.6: Heave forced oscillation results of model BH using one panel.

A (m)	**T (s)**	**KC**	C_a	C_d	C_b	$F_{\textbf{amp}}$ (N)	$R^2_{C_d}$	$R^2_{C_b}$	**RMSE**$_{C_d}$ (N)	**RMSE**$_{C_b}$ (N)	**NRMSE**$_{C_d}$ (%)	**NRMSE**$_{C_b}$ (%)
0.07	2.85	1.41	0.59	4.26	0.55	2.1	0.95	0.98	0.3	0.18	7.1	4.2
0.12	2.85	2.38	0.68	3.44	0.75	4.1	0.93	0.98	0.71	0.37	8.6	4.4
0.16	2.85	3.40	0.73	3.33	1	7.8	0.93	0.98	1.3	0.71	8.4	4.6
0.16	4.27	3.38	0.8	3.35	1.02	3.6	0.95	0.99	0.51	0.27	7.2	3.7
0.21	2.85	4.40	0.79	3.1	1.2	12.3	0.9	0.97	2.32	1.35	9.4	5.5
0.21	4.27	4.35	0.84	3.05	1.21	5.8	0.92	0.98	0.94	0.51	8.0	4.4
0.25	2.85	5.18	0.84	2.97	1.35	16.1	0.89	0.96	3.2	1.92	9.9	6.0
0.25	4.27	5.16	0.9	2.92	1.36	7.3	0.92	0.98	1.23	0.66	8.4	4.5
0.25	5.69	5.14	0.94	2.97	1.39	4.5	0.93	0.98	0.68	0.35	7.5	3.9
0.32	5.69	6.53	1.06	2.73	1.63	6.3	0.91	0.97	1.13	0.65	9.0	5.2
0.32	2.85	6.59	0.91	2.81	1.59	22.4	0.85	0.93	5.36	3.62	12.0	8.1
0.32	4.27	6.55	1.02	2.71	1.61	11.0	0.89	0.96	2.08	1.23	9.4	5.6
0.44	4.27	9.12	1.21	2.49	2.03	19.2	0.87	0.95	4	2.52	10.4	6.6
0.44	5.69	9.10	1.29	2.45	2.04	10.7	0.9	0.96	2.05	1.19	9.6	5.6
0.53	5.69	10.91	1.36	2.3	2.27	14.0	0.9	0.96	2.69	1.56	9.6	5.6
0.57	5.69	11.88	1.41	2.21	2.38	15.1	0.9	0.97	3.07	1.77	10.1	5.9

E

Previous done research on perforated structures - overview

Table E.1: Previous done research on the hydrodynamic loads of plates and perforated plates.

Author	Plate geometry	Porosity	Number of plates	Coefficients	Test type	KC	Period [s]	Effects
Z.H. Liang et al. [24]	Square	no	1	C_a and C_d	Forced oscillation	0.3 - 1.6	5.0 and 10	KC, frequency, thickness
J. Li et al. [25]	Square	0%, 1%, 5% and 10%	1 and 3	C_a and C_d	Forced oscillation	0.2 - 1.2	1.0 - 5.0	KC, beta, plate depth, thickness, edge shape, porosity, hole size, spacing multi-plates
K.H. Chua et al. [26]	Square	0%, 1% and 20%	1	C_a and C_d	Forced oscillation	0.2 - 1.3	1.0 and 2.0	KC, frequency, perforation
K. Liu et al. [27]	Square	0%	1	C_a and C_d	Forced oscillation	0.2 - 0.6	2.14 - 9.00	KC, frequency, motion performance
S. An and Odd M. Faltinsen [33]	Square	8% and 16%	1	C_a and C_b	Forced oscillation	0.15 - 1.65	0.5 - 2.5	KC, frequency, perforation, depth
L.F. Cong and B. Teng [22]	Square	0, 4%, 8%, 16% and 26%	1 and 2	C_a and C_b	Forced oscillation and numerical	0.5 - 1.0	n/a	KC, frequency, opening size, opening distribution and spacing multi-plates
T. Kristiansen et al. [54]	Rectangular	28%	1	C_a and C_b	Forced oscillation	0.2 - 2.5	1.0 - 2.0	KC, frequency and simplified subsea modules
F. Mentzoni [21]	Rectangular	19% and 28%	1 and 3	C_a and C_b	Forced oscillation, waves and numerical	0.2 - 2.0	1.0 - 2.0	KC, frequency, perforation ratio, oscillation and orbital flow patterns plates
X. Tian et al. [30]	Rectangular, square, cylinder, triangle, hexagon, octagon	0%, 5%, 10% and 20%	1, 2 and 3	C_a and C_b	Forced oscillation	0.15 - 3.15	0.5 - 1.0	KC, frequency, shape, thickness, porosity, spacing multiple plates, edge corner radius, hole size
A. Bezunartea-Barrio [43]	Circular	0%	1	C_a and C_b	Forced oscillation and decay test	0.3 - 1.0	5.8 - 17.9	KC, frequency and scale effects
K. Thiagarajan and J. Moreno [34]	Circular	0%	1	C_a and C_b	Forced oscillation in still water and in waves	0.5 - 1.2	1	KC, wave motion on oscillating plate
X. Tian and X. Li [31]	Circular	0%	1	C_a and C_b	Numerical	0.2 - 1.0	n/a	KC, frequency
L. Tao and D. Dray [28]	Circular	0%, 5%, 10% and 20%	1	C_a, C_d and C_b	Forced oscillation	0.2 - 1.2	1.0 and 10	KC, frequency, perforation